AN INVESTIGATION OF TWO-PHASE FLOW REGIME TRANSITION IN LARGE DIAMETER PIPES

BY

WENJIE ZHU,
B.Sc. (NORTHWESTERN POLYTECHNICAL UNIV.)
M.Sc. (TIANJIN UNIVERSITY)

AN INVESTIGATION OF TWO-PHASE FLOW

REGIME TRANSITION IN LARGE DIAMETER PIPES

AN INVESTIGATION OF TWO-PHASE

FLOW REGIME TRANSITION IN

LARGE DIAMETER PIPES

By

WENJIE ZHU, B.Sc, M.Sc.

A Thesis

Submitted to the School of Graduate Studies

in Partial Fulfillment of the Requirements

for the Degree

Master of Applied Science

McMaster University

MASTER OF APPLIED SCIENCE (2003)　　　　　　　McMaster University

(Mechanical Engineering)　　　　　　　　　　　　　Hamilton, Ontario

TITLE:　　　　　　　An Investigation of Two-Phase Flow Regime Transition in

　　　　　　　　　　Large Diameter Pipes

AUTHOR:　　　　　　Wenjie Zhu,　　B.Sc. (Northwestern Polytechnical University)

　　　　　　　　　　　　　　　　M.Sc. (Tianjin University)

SUPERVISORS:　　　Professor C.Y. Ching

　　　　　　　　　Professor M. Shoukri

NUMBER OF PAGES:　xv, 127

Abstract

The characteristics and flow regime transitions of two-phase (gas/liquid) flow in a vertical large diameter pipe were experimentally investigated. The experiments were performed in a 20cm diameter and 10m long pipe using air and water. The bubble characteristics were measured with a dual-optical probe. Data reduction techniques were developed to estimate the local void fraction, bubble diameter, frequency and velocity. A total of twenty-one flow conditions with superficial air velocity in the range 0.02 to 0.24m/s and superficial water velocity in the range 0.25 to 0.45m/s were investigated. Flow pattern transitions from bubbly to churn flow, without an intermediate slug flow, were observed in the present facility. The bubbly to churn transition occurs at lower superficial air velocities compared to that in small diameter pipes. An empirical transition boundary for bubbly to churn transition is developed for the present experiment. The wall-peak local void fraction and bubble frequency profiles, which are characteristic of bubbly flow in small diameter pipes, were only observed at very low void fraction ($\langle \alpha \rangle$< 0.04) bubbly flows. The bubbly flow can be classified into undisturbed and agitated bubbly flow according to the bubble motion. The current data is used to evaluate existing drift-flux model correlations for large diameter pipes.

Acknowledgements

I wish to express my sincere gratitude to Professor C.Y. Ching, my research supervisor. Without his patient shepherding, this thesis would never have been finished. Prof. Ching's devotion and hard work is a lesson worth learning for my future work. I would also like to express my sincere appreciation to my thesis co-supervisor Prof. Shoukri and Dr. Ewing for their valuable suggestions during this project.

Many thanks to R. Lodewyks, D. Schick and J. Verhaeghe for their valuable professional advise and technical guidance. My appreciation to M. Duncan and R. Clifford for their generous help. Thanks to all my colleagues and friends for their assistance and encouragement.

Table of Contents

List of Tables

List of Figures

Nomenclature

ROMAN LETTERS	DESCRIPTION	UNITS
A	Cross-sectional area	m^2
b	Distance from bubble centre to chord	m
C_o	Distribution parameter	
D	Pipe diameter	m
d	Gas bubble/liquid drop diameter	m
f	Sampling frequency	$1/s$
j	Superficial phase velocity	m/s
K	Critical Weber number	
k	Gas constant 1.4	
Ku	Kutateladze number	
L	Length	m
n	Scan number	
P	Pressure	Pa
Q	Volumetric flow rate	m^3/s
r	Gas bubble radius	m
t	Time	s

T	Temperature	K
u	Velocity	m/s
V	Voltage, Optical probe output	V
x	Axial bubble chord length	m
X	Measurement value	
Y	Compressibility factor	

GREEK SYMBOL	**DESCRIPTION**	**UNITS**
α	Void fraction	
β	Diameter ratio	
δ	Standard deviation	
μ	Dynamic viscosity	$kg/m{\cdot}s$
ν	Kinematics viscosity	m^2/s
ρ	Density	kg/m^3
σ	Surface tension	N/m

SUBSCRIPT	**DESCRIPTION**
air	Air phase
b	Bubble
c	Churn
db	Bubble back touches downstream probe
df	Bubble face touches downstream probe
f	Friction
g	Gas phase
H	Hydraulic

I	Interfacial
k	Phase
l	Liquid phase
op	Orifice plate
s	Slug
T	Trigger
ub	Bubble back touches upstream probe
uf	Bubble face touches upstream probe
v	Vertical
water	Water phase

Chapter 1

Introduction

Two-phase gas-liquid flows are important in a wide range of industries, such as the power and process industries [1] [2] [3] [4]. For example, in the nuclear power generation industry, two-phase steam-water flows are common in different sections of the plant. In the offshore oil and gas industry, air-lift pumps are commonly used to lift the gas-oil mixture from the deep-sea bed at depths up to 6000m. Two–phase liquid-vapor flows are also common in refrigeration systems and heat transport loops such as heat pipes and capillary pumped loops.

The accurate determination of mass, momentum and energy transfer in the two-phase flow is necessary for these engineering applications. Although gas-liquid two-phase flows have been studied for several decades, a complete understanding of the dynamics of these flows has not been obtained because of the complex interactions between the two phases. Generally, three models are used to study two-phase flows [5]. These are the homogenous, drift-flux and two-fluid models. In the homogenous model, the two-phase mixture is considered as a single, fictitious fluid, in which the conservation equations (mass, momentum and energy) are identical to the single-phase equations, and

the physical properties of the fictitious fluid are obtained by assuming a uniformly distributed mixture. However, the application of the homogenous model is restricted because most two-phase flows cannot be treated as a uniformly distributed mixture. The drift-flux model takes into account the relative motion between the phases through a constitutive relation. The formulation of the drift-flux model is based on the mixture balance equations with the assumption that the dynamics of the two phases can be expressed by the mixture-momentum equation with a kinematic constitutive equation specifying the relative motion between the phases. The constitutive relation for the drift velocity is a function of the flow patterns, and the rates of momentum transfer at the interfaces depend on the two-phase flow structure.

The two-fluid model has gained increasing attention recently because it is formulated in terms of conservation equations for each phase. The two-fluid model considers the phase interactions at the interface, and the transport processes of each phase are expressed by their own conservation equations. The model can predict more detailed changes and phase interactions than a mixture model such as the drift-flux model or homogenous model, and the two-fluid model is considered the most accurate model so far. The interfacial transfer terms for mass, momentum and energy at the interfaces, however, need to be accurately modeled, and depend on the flow structure.

For closure relations, both the drift-flux and two-fluid models require knowledge of the two-phase flow structure. However, most experimental research of two-phase flow has been performed in small diameter pipes, typically less than 10cm [6] [7] [8] [9]. The relatively few investigations on larger diameter pipes have found that the two-phase flow structure is dependent on the pipe diameter [10] [11] [12] [13] [14] [15] [16]. For example, slug flow, which commonly exists in small diameter pipes, has not been observed in larger diameter pipes. A knowledge of the flow structure and interfacial

transfer terms of two-phase flow in large diameter pipes is, however, important since they occur in many process and chemical industries. This research is aimed at obtaining a better understanding of two-phase flow characteristics in large diameter pipes.

1.1 Motivation

In the last few decades, numerous investigations have been performed on two-phase flow structure in small diameter pipes, which are typically less than 10cm. Nevertheless, there are many applications in the nuclear, chemical and petroleum industries where two-phase flow occurs in large diameter pipes either in steady state or transient conditions. For example, in the offshore gas and oil industry, up to 60cm diameter pipes are often used to transport crude oil and gas from the seabed. Several studies have shown that the flow structure in large-diameter pipes is different to that of small-diameter pipes. For example, Stankovic [11], Hikibi & Ishii [13] and Cheng et al. [16] found that the flow pattern transitions from bubbly to churn without an intermediate slug flow in large diameter pipes. The peak in the radial void fraction distribution near the pipe wall in bubbly flow, which is observed in small diameter pipes, was also only observed in larger diameter pipes at very low void fraction [11].

A better understanding of the flow structure in large-scale pipes is desired in many industrial applications [17] [18]. To increase the accuracy of these simulations, knowledge of the flow regime and the associated void fraction and slip ratio relations of two-phase flow in both large and small diameter vertical pipes are necessary for incorporation in the computer codes. The flow-regime maps and knowledge of the flow structure developed from smaller sized test-facilities [8] [16] are not necessarily able to

accurately predict the flow-pattern in larger diameter pipes and meet the needs of the simulations.

1.2 Objectives

The interfacial transfer terms in the two-fluid models specify the rate of phase change, momentum exchange and heat transfer at the interfaces.   Unless the phase-interaction terms are accurately modeled, the two-fluid models do not necessarily give accurate solutions.   The flow structure in large diameter pipes has been observed to be different to those in small diameter pipes.   Therefore, a better understanding of the two-phase flow regimes, regime transition and relative motion between phases in large diameter pipes is important.

Stankovic [11] and Gerges [12] performed studies in the present flow loop and investigated the bubble characteristics at low void fractions. The flow regime transitions, however, were not fully investigated in these studies. The overall objective of the present investigation is to extend the previous studies to cover a higher range of void fractions and study the flow regime transitions. The specific objectives are:

1. To investigate the flow patterns and transition in a 20cm diameter vertical pipe and compare the results to those from smaller diameter pipes.

2. To study the bubble characteristics such as bubble diameter, bubble velocity, bubble frequency and local void fraction under different flow conditions from bubbly flow to churn flow.

3. To determine the validity of current drift-flux models for large diameter pipes.

1.3   Outline of Thesis

This thesis consists of five chapters. In Chapter 2, previous research on two-phase flow maps and flow transitions in small and large diameter pipes are summarized. The flow models and measurement techniques for two-phase flow are also briefly described in this chapter. The experimental facilities are described in Chapter 3, which include the flow loop instrumentation and data reduction techniques. The results are presented and discussed in Chapter 4. Chapter 5 summarizes the conclusions of the present work.

Chapter 2

Literature Review

The general characteristics of two-phase flow are briefly outlined in this chapter. The different flow patterns and flow maps in vertical up flows are described, followed by a discussion of the flow pattern transitions in small and large diameter pipes. The theoretical models and measurement techniques for two-phase flow are also reviewed in this chapter.

2.1 Two-Phase Flow Patterns in Vertical Pipes

The relative velocity and momentum transfer between the gas and liquid phases in gas-liquid flows give rise to various flow patterns (phase distribution). The flow patterns significantly influence the two-phase flow characteristics such as wall friction and heat transfer. Although the present work is primarily concerned with the flow transition from bubbly to churn in large diameter pipes, the entire range of flow patterns in vertical upward co-current two-phase flows is briefly discussed.

For accurate modeling of two-phase flow, it is necessary to understand the interfacial distribution between the phases and the transfers associated with them. The internal structure of two-phase flow is usually classified by its flow pattern or flow regime. Flow patterns are typically characterized by the void distribution in a cross-section and along the flow direction. The flow patterns are often very complicated and difficult to describe. There is also, generally, a lack of agreement in the description and classification of the flow patterns. Although many definitions have been suggested for the flow patterns, the classification proposed by Hewitt and Hall-Taylor [19] will be used in the present work. The dominant patterns are designated as bubbly, slug, churn and annular (Figure 2.1).

Bubbly Flow

The bubbly flow pattern is characterized by the presence of a continuous liquid phase in which gas bubbles, with maximum size far smaller than the pipe diameter, are dispersed more-or-less randomly in the liquid continuum [20]. The gas bubbles are not necessarily evenly dispersed in a given cross-section. The bubbles move upward with a velocity greater than the adjacent liquid, and the relative slip causes a perturbation of the basic flow pattern and gives rise to a wake behind the bubble. The bubbles in the wake can accelerate and collide and coalesce with the upstream bubble.

Slug Flow

Slug flow is characterized as a series of Taylor bubbles separated by slugs of continuous liquid. A typical Taylor bubble is a constant pressure surface whose shape is that of a cylinder bounded on top by a spherical cap or a bullet shaped nose and a distorted flat tail at the bottom. The mean diameter of a Taylor bubble is almost equal to the pipe diameter with length at least one pipe diameter. Between the Taylor bubbles and the pipe wall, liquid flows downward in the form of a thin falling film. The Taylor

bubbles move uniformly upward and are separated by slugs of continuous liquid containing smaller gas bubbles. There is a large axial variation in void fraction between the Taylor bubbles and the liquid slugs. At a section across a Taylor bubble, the flow is similar to annular flow, while across a liquid slug, it is similar to dispersed bubbly flow. As the void fraction is increased, the Taylor bubbles are elongated and line up closely with the tail of the preceding bubble touching the nose of the downstream bubble. In this instance, the liquid slug between the bubbles become unstable and cannot sustain its shape due to the strong wake behind the bubbles.

Churn Flow

Churn flow is somewhat similar to slug flow, but much more chaotic, frothy and disordered. Increasing the air flow rate for a slug flow results in the bullet-shaped Taylor bubble becoming narrower and distorted. The continuity of the liquid in the slug between successive Taylor bubbles is repeatedly destroyed by a high local gas concentration in the slug. As this happens, the liquid slug falls and the liquid accumulates forming a bridge, which is again lifted by the gas. Typical churn flow is characterized by this oscillatory or alternating direction of motion of the liquid slug as well as the liquid film on the pipe wall. The interfaces between the gas and liquid phases have irregular boundaries and it is hard to distinguish the continuous phase, with the flow alternating between gas and liquid continuous flows. At relatively lower gas flow rates, churn flow may be regarded as a breaking up of slug flow with an occasional bridging across the tube by the liquid phase. At relatively higher gas flow rates it may be considered as a degenerate form of annular flow with the film flow direction changing and very large waves formed on the interface [20].

Annular Flow

Annular flow is characterized by the continuity of the gas phase along the pipe core [9]. The liquid phase travels upwards partly as a wavy liquid film and partly in the form of drops entrained in the gas core. It has also been described as a wispy-annular pattern when the entrained phase is in the form of large lumps or "wisps". Annular flow develops from churn flow from two basic mechanisms [9]; flow reversal in the liquid film section along large bubbles and destruction of liquid slugs or large waves by entrainment or deformation. For certain flow rates, the majority of the liquid travels as drops leading to the term mist flow being applied to this flow pattern. The upward flow of the liquid film against gravity results from the forces exerted by the fast moving gas core. This film has a wavy interface and the waves tend to shatter and enter the gas core as entrained droplets. Thus, the liquid moves upwards, due to both interfacial shear and form drag on the waves and drag on the droplets. Annular flow cannot exist unless the gas velocity in the gas core is sufficient to lift the entrained droplets.

2.2 Flow Maps

The normal practice of presenting flow patterns is in the forms of a flow pattern map where the flow patterns are plotted against certain characteristics of the flow. There are a wide variety of flow pattern maps for vertical flow in the literature [21] [22]. It is important to understand that maps prepared from data taken for one pipe size and fluid properties are not necessarily valid for other sizes or properties. Both dimensional and dimensionless coordinates have been used for the flow maps [9]. Dimensionless coordinates have been used with the expectation that a universal flow pattern map can be obtained. However, without a proper theoretical basis, the use of dimensionless

coordinates is no more general than the use of dimensional ones. Griffith and Wallis [23] attempted to invoke theory to develop suitable dimensionless coordinates. They showed that the dimensionless coordinates u^2/gD and j_g/j controlled the transition from the slug to annular flow patterns. The theory was, however, not completely sufficiently to provide an analytical expression for the transition boundary [9]. Among the flow pattern mapping techniques, dimensional coordinates such as superficial velocities j_g and j_l [5] [9] or superficial momentum flux, $\rho_g j_g^2$ and $\rho_l j_l^2$ [22] are widely used. Models frequently used for predicting the flow pattern transition for upward gas-liquid flow include those from Taitel et al. [9] and Mishima and Ishii [24] (Figure 2.2 and Figure 2.3). There is only very limited data for flow maps of two-phase flow in large diameter pipes. Such as a flow map of the similar flow loop (D=20cm) by Nada et al. [15] (Figure 2.4), and a flow map of Ohnuki et al. based on experiment data [14] for a 20cm diameter pipe (Figure 2.5).

2.3 Flow Pattern Transitions

The interactions between bubbles, such as collisions and coalescences and interactions between the bubbles and the pipe wall make the flow pattern complex and difficult to be described by a mathematical model. Knowledge of the flow patterns and the transitions between them, however, are required to establish models for each flow pattern. The gas bubbles in a liquid flow are found to have a wide distribution of size and shape. When they are very small, they remain spherical and move vertically upward in a rectilinear motion. As the bubble size increases, the buoyancy force increases with a consequent increase in the velocity. As the bubble concentration increases, coalescence between bubbles can produce larger bubbles or void gap with higher rise velocities and,

more significantly, with some bubbles rising more rapidly with others being carried downwards. In most cases, the transition boundaries are empirically determined and are not based on physical models. Thus, it is important to understand the mechanisms by which the transition from one flow pattern to another takes place to improve the generality of the prediction and classify the experimentally observed flow patterns.

2.3.1   Transition in Small Diameter Pipes

The physical mechanisms of the flow pattern transitions are introduced in this section. Models developed by Mishima and Ishii [24] and Taitel et al. [9] for two-phase flow in vertical pipes, which are in good agreement with experimental data in small diameter pipes, are also presented.

Bubbly-Slug Transition

When gas is introduced at low flow rates into a vertical column of liquid, the gas phase is distributed as discrete bubbles. Many studies of bubble motion demonstrate that if the bubbles are very small, they behave as rigid spheres rising vertically in rectilinear motion [9]. Transition from dispersed bubbles observed at low gas flow rates to slug flow requires a process of agglomeration or coalescence. As the gas flow rate increases, the bubble frequency increases and the closer bubble spacing results in an increase in the coalescence rate. However, as the liquid flow rate increases, the turbulent fluctuations associated with the flow can cause breakup of larger bubbles formed as a result of agglomeration [26]. If this breakup is sufficiently intense to prevent recoalescence, then the dispersed bubble pattern is maintained. Otherwise, with an increase of gas flow rate at low liquid flow rates, the bubble frequency increases and the dispersed bubbles become so closely packed with many collisions and the rate of agglomeration to larger

bubbles increases sharply. If the size of the larger bubbles reaches a critical size, the spherical bubbles begin to deform, and move upward in a zigzag pattern. The bubbles randomly collide and coalesce, forming a number of larger individual bubbles with a spherical cap similar to the Taylor bubbles of slug flow, but with a diameter smaller than the pipe. Thus, the flow is characterized as an array of smaller bubbles moving in zigzag motion and the occasional appearance of larger cap bubbles. Eventually, the coalescence of the larger cap bubbles will result in a transition to a Taylor bubble. The turbulent breakup process can prevent agglomeration only if the bubble size produced is small enough for the bubbles to remain spherical. Brodkey [25] gives the critical bubble size at which this occurs as:

$$d_{crit} = \left[\frac{0.4\sigma}{(\rho_l - \rho_g)g} \right]^{1/2} \qquad (2\text{-}1)$$

Once the fluid properties (liquid and gas phase density ρ_l, ρ_g, surface tension σ, and kinematics viscosity v_l) and pipe diameter D are set, the relationship between j_g and j_l below which the turbulent induced dispersion takes place and slug flow cannot exist is given by [9]:

$$j_g + j_l = 4.0 \left\{ \frac{D^{0.429}(\sigma/\rho_l)^{0.089}}{v_l^{0.072}} \left[\frac{g(\rho_l - \rho_g)}{\rho_l} \right]^{0.446} \right\} \qquad (2\text{-}2)$$

The existence of an above-critical bubble size in a flow field depends on the diameter of the tube. If the tube is wider, then some of them may co-exist and move together with lower-critical-size bubbles. If it is narrow then these distorted bubbles form Taylor bubbles very quickly and give rise to slug flow [9].

Besides the mechanism introduced above, several other mechanisms for the transition from bubbly flow to slug flow in small diameter pipes have been suggested [27] [28] [29] [30]. Radovicich & Moissis [27] postulated that transition is due to collisions between small bubbles, with a fraction of these collisions resulting in coalescence, ultimately leading to bubbles which are of similar diameter to the pipe. Bubbly flow can be considered as a transient flow regime, and given a sufficiently long residence time, will develop into slug flow. However, Hewitt [29] determined there was no effect of pipe length on the transition, implying that the transition from bubbly to slug occurs simultaneously throughout the channel, and making it unlikely that break-up and coalescence of the bubbles is the mechanism responsible for the transition. Taitel et al. [9] claimed that bubble coalescence is responsible for the transition to slug flow, but suggested a dispersed bubble flow pattern can be maintained if an equilibrium between bubble coalescence and break-up due to liquid turbulence is reached.

A void fraction of around 0.25 to 0.30 has been suggested as the transition criteria from bubbly to slug flow from experiments [31]. Radovicich and Moissis [27] used a semi-theoretical approach by considering the bubbles dispersed in a cubic lattice in which the individual bubble were allowed to fluctuate. The void fraction was found to be about 0.30 when the packing gap between two bubbles became less than a bubble diameter and the bubble collision and coalescence rates became very high.

From the above geometrical consideration [27], Mishima and Ishii [24] developed an empirical model, where the transition criterion is given by

$$j_l = \left(\frac{3.33}{C_0} - 1 \right) j_g - \frac{0.76}{C_0} \left(\frac{\sigma g (\rho_l - \rho_g)}{\rho_l^2} \right)^{\frac{1}{4}} \tag{2-3}$$

The distribution parameter C_0 for round tubes in a moderate Reynolds number range is given by [33]:

$$C_0 = 1.2 - 0.2 \sqrt{\frac{\rho_g}{\rho_l}} \tag{2-4}$$

Taitel et al. [9] speculated that transition from bubbly to slug occurred at a void fraction below that predicted by Radovicich and Moissis [27] because of the bubble deformation and its random path. They used a criterion of $\alpha = 0.25$ and obtained the transition boundary as:

$$j_l = 3.0 j_g - 1.15 \left[\frac{g (\rho_l - \rho_g) \sigma}{\rho_l^2} \right]^{\frac{1}{4}} \tag{2-5}$$

The radial distributions of void fraction and bubble frequency have different profiles in bubbly and slug flow [34]. The local void fraction changes from a saddle shaped profile to a parabolic shape as the flow pattern transition from bubbly to slug (Figure 2.6). The peak in the local void fraction in the vicinity of the pipe wall is commonly observed in the low gas flow rate region. Increasing the gas flow rate at constant liquid velocity decreases the relative peak value of the void fraction near the wall to the value at the pipe center. The location of the peak is about one mean bubble radius from the wall. Similar to the void fraction distribution [34], the bubble frequency distribution is also saddle shaped in bubbly flow (Figure 2.7), whereas it is parabolic-shaped in slug flow.

Slug-Churn Transition

Once Taylor bubbles are formed, they occupy most of the pipe cross-sectional area and are axially separated by a liquid slug in which small bubbles are dispersed. The liquid confined between the Taylor bubbles and the pipe wall flows around the bubble as a falling film. In small diameter pipes, with an increase in gas flow rate, the ratio of Taylor bubble length to liquid slug length decreases and the liquid slugs become more aerated. At a certain critical gas flow rate, the slug flow transitions to churn flow. In churn flow, the continuity of the liquid phase between successive distorted Taylor bubbles is frequently destroyed by the gas phase. As this happens, the liquid slug falls and the falling liquid accumulates forming a bridge which is again lifted by the gas.

There are considerable difficulties in accurately identifying the slug-churn transition because there is confusion as to the description of the churn flow itself. Taitel et al. [9] characterized churn flow when oscillatory motion of the liquid is observed. In churn flow, the liquid slug is too short to support a stable liquid bridge between two consecutive Taylor bubbles. The falling film around the bubble penetrates deeply into the liquid slug creating a highly agitated aerated mixture at which point the liquid slug is seen to disintegrate and to fall in a rather chaotic fashion. The liquid re-accumulates at a lower level at the next slug where liquid continuity is restored and the slug then resumes its upward motion [8]. Thus, the oscillatory motion of the liquid is an important characteristic of churn flow.

Several mechanisms and models have been proposed for the slug to churn transition in small diameter pipes. Bilicki and Kestin [35] proposed the transition may occur by one of two mechanisms. In the first, when a Taylor bubble approaches the one ahead of it by a distance lower than a characteristic length, it is accelerated by the flow field to catch up and coalesce with its predecessor. When this occurs, the slug-flow

pattern gives way to churn flow. The second possible mechanism of flow pattern transition is that of onset of instability in the thin layer of liquid between the Taylor bubble and the pipe wall [36]. Brauner and Barnea [37] concluded that transition takes place when the gas void fraction within the liquid slug reaches the maximum bubble cubic volumetric packing (0.52). McQuillan and Whalley [20] and Wallis [5] thought the flooding of the liquid film surrounding the Taylor bubble in the slug flow is the mechanism of the transition. Jayanti and Hewitt [38] used the flooding mechanism by accounting for the effect of the Taylor bubble length to explain the transition. Chen & Brill [39] used the explanation of Bilicki and Kestin's first mechanism on the basis of the wake effect behind Taylor bubbles. The influence of the pipe scale was not considered in any of the above models.

Taitel and Dukler [40] observed that when the liquid slug separating two consecutive Taylor bubbles becomes very short, the wake behind the Taylor bubble destroys the effective slug bridge. Mishima & Ishii [24] had a similar proposal and postulated the transition occurs from slug flow to churn flow when the void fraction in the liquid-slug section reaches the mean void fraction in the slug-bubble section. The transition criterion is given by

$$\frac{j_g}{C_0 j + 0.35(\Delta \rho g D / \rho_l)} = 1 - 0.813 \left\{ \frac{(C_0 - 1)j + 0.35\sqrt{\dfrac{\Delta \rho g D}{\rho_l}}}{j + 0.75\sqrt{\left(\dfrac{\Delta \rho g D}{\rho_l}\right) \cdot \left(\dfrac{\Delta \rho g D^3}{\rho_l \cdot v_l^2}\right)^{\frac{1}{18}}}} \right\}^{0.75} \qquad (2\text{-}6)$$

where

$$\Delta \rho = \rho_l - \rho_g \qquad (2\text{-}7)$$

16

$$j = j_l + j_g \tag{2-8}$$

From experimental observations, Taitel et al. [9] pointed out that the churn flow pattern could be considered as an entry region phenomenon associated with the existence of slug flow further along the pipe. The entry length for churn flow calculated as a criterion of slug to churn flow transition was given by

$$\frac{L}{D} = 40.6 \left(\frac{j_l + j_g}{\sqrt{gD}} + 0.22 \right) \tag{2-9}$$

Churn–Annular Transition

As the gas flow rate is further increased, the churn flow transitions to annular flow, where the liquid flows upwards as a film adjacent to the wall with the gas flow in the pipe core. The conditions for annular flow to persist was studied by Pushkin and Sorokin [41], and it was shown that the phenomenon is governed by the Kutateladze number,

$$K_u = j_g \rho_g^{1/2} [g\sigma(\rho_l - \rho_g)]^{-1/4} \tag{2-10}$$

Annular flow is possible when $K_u > 3.2$, below which flooding occurs and churn flow exists. This empirical result shows good agreement with the criteria developed by Taitel et al. [9], where it is suggested that annular flow will not exist if the gas velocity in the gas core is not sufficient to lift the entrained droplets. The minimum gas velocity required to suspend a drop is determined from a balance between the gravity and drag forces acting on the drop. The maximum stable drop size from Hinze [43] is

$$d = \frac{K\sigma}{\rho_g u_g^2} \tag{2-11}$$

where the K is the critical Weber number of 30. Thus, the transition boundary can be obtained as:

$$\frac{j_g \rho_g^{1/2}}{\left[\sigma g(\rho_l - \rho_g)\right]^{1/4}} = 3.1 \qquad (2\text{-}12)$$

Mishima and Ishii [24] developed criteria for churn to annular transition according to two different mechanisms: flow reversal in the liquid film section along large bubbles and destruction of liquid slugs or large waves by entrainment or deformation. The first mechanism assumes the annular drift-velocity correlation can be used locally for the film section along large bubbles:

$$j_g = \sqrt{\left(\frac{\Delta \rho g D}{\rho_g}\right)}(\alpha - 0.11) \qquad (2\text{-}13)$$

and the second criterion were obtained from the onset of droplet entrainment:

$$j_g = \left(\frac{\sigma g \Delta \rho}{\rho_g^2}\right)^{1/4} \left(\frac{\sqrt{\rho_l \sigma}}{\mu_l}\left(\frac{\sigma}{g \Delta \rho}\right)^{1/4}\right)^{1/5} \qquad (2\text{-}14)$$

2.3.2   Transition in Large Diameter Pipes

Most previous studies in large diameter pipes are related to flow pattern and pressure drop [13] [45] [46] [47]. The flow pattern transition was investigated by Stankovic [11] and Nada et al. [15] in the current facility (*D*=20cm) (Figure 2.4) and Ohnuki et al. [14] in a similar 20cm diameter pipe (Figure 2.5).

Stankovic [11] reported that the saddle shaped void fraction profile in bubbly flow was only observed at very low void fraction ($<\alpha>$ < 0.04). When the gas flow rate was increased, the profiles became parabolic. In the same facility, Gerges [12] did not observe the saddle shaped void fraction profiles. Instead, the profiles for local void fraction, bubble frequency and velocity in bubbly flow were parabolic. The bubble diameter profile observed by Gerges [12] was uniform within the core region and a small incease near the wall.

The flow patterns described by Ohnuki et al. [14] are not generally those used by other researchers. The flow patterns were described as undisturbed bubbly, agitated bubbly, churn bubbly, churn slug and churn froth. In undisturbed bubbly flow, the distinct bubbles have an uniform upward movement with few collisions. The agitated bubbly flow was described as bubble clusters with random movement with some clusters moving downward in the wake of the larger bubble clusters. The large coalescent bubbles flow in a similar manner to the cap bubbles in churn bubbly, churn slug and churn froth flow. A churn bubbly flow was observed as the air flow rate increased from undisturbed bubbly flow. The radial distributions of the flow characteristics observed by Ohnuki et al. are somewhat different to those in small diameter pipes (Figure 2.8). For example, the void fraction distribution is classified into a wall-peak phase distribution or a core-peak depending on the flow rate. The bubble diameter distribution is almost flat with a wall-peak for undisturbed bubbly and churn bubbly flow, while the bubble velocity has a peak at the pipe center in churn bubbly flow.

Cheng et al. [16] observed that the bubble size and velocity had a gradual transition as the flow transitioned from bubbly to churn in a 15cm diameter pipe. Although the pressure fluctuations generated by the alternate passage of liquid slugs and big gas voidage were observed, the high gas voidage did not have a closed smooth

surface like the traditional Taylor bubbles in small pipes.   The bubble frequency, velocity, chord length and local void fraction were found to have parabolic profiles for the churn flow pattern.

The void fraction at the bubbly to churn flow pattern transition was measured by Hikibi et al. [13] to occur at $\alpha = 0.17$ in a 10.2cm diameter vertical pipe.

2.4   Theoretical Models

Due to the complex nature of two-phase flow, a complete analytical solution has not been developed yet.   Three approaches have been widely used to model two-phase flows based on assumptions regarding the relative motion between the phases and the interfacial conditions.   The homogeneous equilibrium model is the earliest and simplest two-phase flow model.   It assumes the two phases have the same velocity and are in thermodynamic equilibrium.   The closure laws for homogeneous models can be derived directly from the methodology for single-phase flows.

The drift-flux model for void-fraction prediction in two-phase flow was first postulated by Zuber and Findley [6].   The most important assumption associated with the drift-flux model is that the motion of the whole mixture is expressed by the mixture-momentum equation and the relative motion between phases is taken into account by a kinematic constitutive equation.   Therefore, the basic concept of the drift-flux model is to consider the mixture as a whole, rather than as two separated phases [33].   The use of the drift-flux model is appropriate only when the motions of the two phases are strongly coupled.

The drift-flux model implies a linear relationship [6] between the gas velocity v_g and superficial mixture velocity j.

$$v_g = \frac{J_g}{\alpha} = C_0 \cdot j + v_{gj} \tag{2-15}$$

C_0 is a distribution parameter that represents the effect of non-uniform flow and concentration profiles and v_{gj} is the local drift velocity that represents the local relative velocity between the phases. There have been several investigations to estimate the values and forms of the drift-flux velocity and distribution coefficient [8] [34] [50]. The drift-flux model is only an approximate formulation in comparison with the more rigorous two-fluid formulation. However, because the formulation is based on the mixture balance instead of separate balance equations for each phase, the drift-flux model is simpler and can be applicable to a wide range of two-phase flow problems of practical interest.

The drift-flux model has been studied for relatively large diameter pipes, where the drift velocity is found to differ from that of small diameter pipes [48] [50]. A number of correlations have been developed for C_0 and the mean drift velocity v_{gj}. Kataoka and Ishii [50] proposed Equation (2-4) for C_0 of the fully developed flow in round tubes. The following correlations for the drift velocity for large diameter pipes were developed as [50]:

$$v_{gj}^{+} = 0.0019 D_H^{*\,0.809} \left(\frac{\rho_g}{\rho_l} \right)^{-0.157} N_{\mu l}^{-0.562} \tag{2-16}$$

for $D_H^{*} \leq 30$ and $N_{\mu l} \leq 2.2 \times 10^{-3}$

$$v_{gj}^{+} = 0.03 \left(\frac{\rho_g}{\rho_l} \right)^{-0.157} N_{\mu l}^{-0.562} \tag{2-17}$$

for $D_H^{*} \geq 30$ and $N_{\mu l} \leq 2.2 \times 10^{-3}$

$$v_{gj}^{+} = 0.92 \left(\frac{\rho_g}{\rho_l} \right)^{-0.157} \tag{2-18}$$

for $D_H^* \geq 30$ and $N_{\mu l} > 2.2 \times 10^{-3}$

where the dimensionless drift velocity v_{gj}^{+}, dimensionless viscous number $N_{\mu l}$ and dimensionless hydraulic diameter D_H^* are defined by:

$$v_{gj}^{+} = \frac{v_{gj}}{\left(\dfrac{\sigma g \Delta \rho}{\rho_l^2} \right)^{1/4}} \tag{2-19}$$

$$N_{\mu l} = \frac{\mu_l}{\left(\rho_l \sigma \sqrt{\dfrac{\sigma}{g \Delta \rho}} \right)^{1/2}} \tag{2-20}$$

$$D_H^* = \frac{D_H}{\sqrt{\dfrac{\sigma}{g \Delta \rho}}} \tag{2-21}$$

Ishii used the above relations to develop drift velocities for specific flow regimes (bubbly, slug and churn turbulent bubbly flows) in a relatively small diameter pipe ($D \leq 40/\sqrt{\sigma/g\Delta\rho}$) and are given by [33].

$$v_{gj} = (1-\alpha)^{1.75} \sqrt{2} \left(\frac{\sigma g \Delta \rho}{\rho_l^2} \right)^{1/4} \tag{2-22}$$

$$v_{gj} = 0.35 \left(\frac{g \Delta \rho D}{\rho_l} \right)^{1/2} \tag{2-23}$$

$$v_{gj} = \sqrt{2}\left(\frac{\sigma g \Delta\rho}{\rho_l^2}\right)^{1/4} \tag{2-24}$$

Based on experimental data (D=5.08cm and 10.2cm), Hirao et al. [52] proposed the following drift-flux type correlation for a relatively large diameter pipe:

$$v_{gj} = 0.52\sqrt{\frac{g\Delta\rho D}{\rho_l}} \tag{2-25}$$

for $j \geq 0.24\,\text{m/s}$ $P \leq 1.5\,\text{MPa}$ and $D \geq 5\,\text{cm}$.

Shoukri et al. [10] developed a correlation for the drift-flux model for a 20cm diameter pipe as,

$$\frac{j_g}{\alpha} = 0.8j + 0.45 \tag{2-26}$$

The distribution parameter was observed to decrease with an increased pipe diameter. However, the drift velocity was found to not change much with the pipe scale [10].

The two-fluid model, which uses the conservation equations for the gas and liquid phases, is the most recent [53]. In the two-fluid model formulation, the transport processes of each phase are expressed by their own conservation equations. Therefore, it can be expected that the model can predict more detailed changes and phase interactions than a mixture model such as the drift-flux model. A three-dimensional two-fluid model has been obtained by using temporal or statistical averaging. The model is expressed in terms of two sets of conservation equations governing the balance of mass, momentum and energy in each phase. However, since the averaged fields of one phase are not independent of the other phase, the interaction terms appear in the field equations as

source terms. For most practical applications, the model developed by Ishii [54] using temporal and statistical averaging can be simplified to the following forms.

Conservation of Mass:

$$\frac{\partial}{\partial t}(\varepsilon_k \rho_k) + \nabla \cdot (\varepsilon_k \rho_k u_k) = \Gamma_k \tag{2-27}$$

Conservation of Momentum:

$$\frac{\partial}{\partial t}(\varepsilon_k \rho_k u_k) + \nabla \cdot (\varepsilon_k \rho_k u_k{}^2)$$
$$= -\varepsilon_k \nabla P_k - \nabla \cdot \varepsilon_k (\overline{\tau_k} + \tau_k') + \varepsilon_k \rho_k g + u_{ki} \Gamma_k + M_{ik} - \nabla \varepsilon_k \cdot \tau_i \tag{2-28}$$

Conservation of Energy:

$$\frac{\partial \alpha_k \rho_k H_k}{\partial t} + \nabla \cdot (\alpha_k \rho_k H_k \vec{v}_k) = -\nabla \cdot \alpha_k (\overline{\overline{q}}_k + q_k{}^t) + \alpha_k \frac{D_k}{Dt} P_k + H_{ki} \Gamma_k + \frac{q''_{ik}}{L_s} + \Phi_k \tag{2-29}$$

The subscript k denotes liquid (l) or gas (g) phase, and i stands for the value at the interface

Γ_k	Mass generation
M_{ik}	Generalized interfacial drag
τ_i	Interfacial shear stress
q''_{ki}	Interfacial heat flux
Φ_k	Dissipation
L_s	Length scale at the interface
$1/L_s = a_i$	Interfacial area concentration

Several interfacial transfer terms appear on the right-hand sides of the Equations (2-27, 28, 29). As pointed out by Ishii [54], the weakest but important link in the multi-fluid model formulation is the constitutive equations for the interfacial interaction terms. Two-fluid models recognize the presence of flow patterns and treat the exchanges at the gas-liquid interface specifically. Consequently, in addition to the constitutive equations for ∇P_k, $\overline{\tau}_k$, $\tau_k{}'$ and τ_i, the two-fluid models require the closure laws to explicitly deal with the phase interface and flow patterns. In general, the interfacial transfer terms, Γ_k and M_{ik}, can be modeled in terms of interfacial area concentration and the corresponding driving forces as:

$$\Gamma_k = -\rho_{ki}(u_{ki} - u_i) \cdot n_{ki}a_i \qquad (2\text{-}30)$$

$$M_{ik} = -\rho_{ki}u_{ki}(u_{ki} - u_i) \cdot n_{ki}a_i \qquad (2\text{-}31)$$

$$\Gamma_k H_{ki} + q''_{ki}/L_s = a_i(\overline{m}_k H_{ki} + q''_{ki}) \qquad (2\text{-}32)$$

Since these interfacial transfer terms should also obey the balance laws at the interface, interfacial transfer conditions could be obtained from an average of the local jump conditions. They are given by:

$$\sum_k \Gamma_k = 0 \qquad (2\text{-}33)$$

$$\sum_k M_{ik} = 0 \qquad (2\text{-}34)$$

$$\sum_k H_{ki}\Gamma_k + \frac{q''_{ik}}{L_s} = 0 \qquad (2\text{-}35)$$

The interfacial area concentration or interfacial surface area per unit volume, a_i, is defined as the ratio of the gas phase surface area to the total flow volume [56]:

$$a_i = \frac{A_{sg}}{V}$$

(2-36)

where A_{sg} is the surface area of the gas phase, and V is the total flow volume. In practical two-phase flows, the interfacial distribution is so complicated that it is almost impossible to determine the local instant interfacial area concentration by experiment or analysis. Therefore, the averaged interfacial area concentration becomes quite important and several studies have been performed to determine this parameter [54] [59]. According to Ishii et al. [53] [54] [55], the interfacial area per unit volume can be expressed as

$$a_i = a_{ib} = \frac{6\alpha_g}{d_{sm}} \text{ in bubbly flow regime}$$

(2-37)

$$a_i = a_{is} = \frac{4.5}{D}\frac{\alpha_g - \alpha_{gs}}{1-\alpha_{gs}} + \frac{6\alpha_{gs}}{d_{sm}}\frac{1-\alpha_g}{1-\alpha_{gs}} \text{ in slug flow regime}$$

(2-38)

For churn-turbulent flow, the interfaces around the large bubbles become very irregular due to turbulent motions. To take into account this effect, a roughness parameter C_{ct} is introduced to obtain

$$a_i = a_{ic} = \frac{4.5C_{ct}}{D}\frac{\alpha_g - \alpha_{gs}}{1-\alpha_{gs}} + \frac{6\alpha_{gs}}{d_{sm}}\frac{1-\alpha_g}{1-\alpha_{gs}}$$

(2-39)

where $C_{ct} > 1$ in churn flow and α_g, α_{gs}, D. d_{sm} refer to gas phase volumetric fraction, average void fraction in liquid slug, pipe diameter, and sauter mean diameter of small bubbles, respectively. In general, however, the interfacial area concentration decreases in

churn-turbulent flow due to increased coalescence in the liquid-film and slug sections [54]. The first term on the right hand side in Equations (2-38) and (2-39) represents the contribution of the gas slug and the second term that of the small bubbles in the liquid slug. For the present estimation of a_i, it was assumed

$$a_{is} = a_{ic}(C_{ct} = 1)$$

(2-40)

for simplicity. The average void fraction α_{gs} in the liquid slug is given by Kurul and Podowski [32] as

$$\alpha_{gs} = \begin{cases} \alpha_g & (0 \leq \alpha_g < 0.25) \\ 0.3929 - 0.5714\alpha_g & (0.25 \leq \alpha_g < 0.6) \\ 0.05 & (0.6 \leq \alpha_g \leq 1) \end{cases}$$

(2-41)

The expression for d_{sm} is given by Kocamustafaogullari et al. [60] as

$$d_{sm} = 1.06 \left(\frac{\sigma}{\rho_l^{1/3}} \right)^{1/3} \left\{ \frac{\alpha_g(1-\alpha_g)D^2}{j(-dP/dx)} \right\}^{2/9}$$

(2-42)

Among the several averaging techniques for the interfacial area concentration, the time-averaged value is most often used [59].

$$\bar{a}_i = \frac{1}{T} \sum_{j=1}^{N} \frac{1}{|n_{kij} \cdot v_{ij}|}$$

(2-43)

where n_{kij} is the normal outward vector of phase k at the interface and the suffix j denotes the jth interface passing a point during time interval T. Measuring the time averaged interfacial area concentration based on Equation (2-43) is physically possible

but is quite difficult with current measuring techniques. Kataoka and Serizawa [59] developed a practical method to calculate the interfacial area concentration based on several statistical assumptions for the interfacial configuration and movement. The method was applied only to bubbly flow and the radial distributions of interfacial area concentration were measured. Assuming spherical bubbles and random bubble motion, the time averaged interfacial area concentration is given by [59]

$$\overline{a_i} = 4N \overline{\left(\frac{1}{u_b}\right)} \frac{1}{1 - \cot\frac{\alpha_0}{2} \ln\left(\cos\frac{\alpha_0}{2}\right) - \tan\frac{\alpha_0}{2} \ln\left(\sin\frac{\alpha_0}{2}\right)} \qquad (2\text{-}44)$$

where α_0 is determined by

$$\frac{\sin 2\alpha_0}{2\alpha_0} = \frac{1 - \left(\overline{\left|u_b'\right|^2} \middle/ \overline{\left|u_b\right|^2}\right)}{1 + 3\left(\overline{\left|u_b'\right|^2} \middle/ \overline{\left|u_b\right|^2}\right)} \qquad (2\text{-}45)$$

where N, u_b and u_b' are the number of bubbles passing a probe per unit time, the velocity of the bubble and its fluctuation. These quantities can be measured by a single optical probe with double sensors. Based on their data, Serizawa and Kataoka [61] obtained the following correlation.

$$a_i = 1030 j_l^{0.2} \alpha_g^{0.87} \quad (j_l \geq 1\text{m/s}) \qquad (2\text{-}46)$$

A similar correlation was obtained by Mishima et al. [24]. However, for a small liquid flux ($j_l \leq 1\text{m/s}$), the dependence of the interfacial area concentration on the liquid flux was reversed and the data were not successfully correlated.

2.5 Measurement Techniques

In order to develop and verify two-phase flow models, many measurement techniques have been developed to measure the local flow variables. Several such techniques are reviewed in this section. The common intrusive techniques include conductivity devices, hot-film anemometry and optical probes while non-intrusive techniques include gamma densitometry, capacitance and ultrasonic methods [62] [63].

2.5.1   Intrusive Techniques

The most common intrusive methods are those that use conductivity probes, hot-film anemometry and optical probes. All are based on the operating principle of phase detection using variations in the local fluid properties of the two phases. Generally, the local information such as void fraction, bubble size and bubble velocity can be obtained by the output signals from one or two sensors.

Conductivity Devices

The principle of two-phase flow measurements by conductivity devices is based upon the difference in conductivity between the gas and liquid phases. Investigations related to resistivity probes include those by Liu and Bankoff [8], Serizawa et al. [64], Delhaye [65], Herringe and Davis [66], Barrau et al. [67] and Hamad et al. [68]. A typical probe tip is made of Tungsten wire housed in a stainless steel tube. When the probe tip is in contact with the liquid phase, the circuit is closed because the liquid is conducting and when it is in the gas phase, the circuit is open. The output voltage signal of the probe provides a time trace of the times the probe is in the gas and liquid phase. A significant difference in the electrical conductivities of the two phases is required to accurately discriminate the output signal into the two distinct phases. The probe,

however, cannot be used in dispersed droplet flow because of the difficulty of having a continuous electrical path in the liquid phase between the two electrodes.

Hot-Film Anemometry

Hot-film anemometry has been successfully used in two-phase flow. In hot-film anemometry, the output signal is proportional to the heat transfer from the probe to the fluid. An electronic feed back circuit is used to maintain the sensing element at a constant temperature higher than the surrounding fluid. The large difference in heat transfer from the sensor to the liquid and gas can therefore be used for phase identification as well as for measurements in the continuous phase [34] [69]. The hot-film anemometry probe consists of a sensing element across two needles. When fluid passes the probe, the sensor is cooled, resulting in a decrease in its resistance. A fast response bridge circuit senses the decrease in resistance and the bridge voltage is changed to maintain a constant sensor temperature. The most significant limitation of hot-film anemometry measurements is the need to produce an output voltage signal which has a high signal-to-noise ratio. This proves to be most difficult at high mass flux and high-pressure conditions where the convective heat transfer from the hot-film senor to the gas phase become significant and the delineation between liquid and vapor parts of the voltage signal is not clear, thereby making the selection of an appropriate threshold voltage difficult [64].

Optical Probes

While conductivity probes can be used only in aqueous systems and hot-film anemometry has restrictions on the flow conditions, an optical probe can be used in non-aqueous systems over a wide range of flow conditions. The probe utilizes light emitted through an optical fiber, and the intensity of the light reflected back from the probe tip is used to distinguish the phase. The reflected light from the optical probe is sensitive to the

change in refractive index of the surrounding medium and is thus responsive to interfacial passages. Depending on the optical properties of the two phases, the light beam is almost totally reflected or partially reflected when the probe tip is in contact with the gas and liquid phase. The intensity of the reflected optical signals, which is returned via an optical fiber, will depend on the phase the tip is in contact with. The optical signal is typically converted into voltage signals via a photo-multiplier and amplified.

Dual-sensor probes consist of two active sensing elements that are separated in the flow direction by a known distance and can be used for bubble velocity measurements. The bubble velocity is estimated from the distance between the two sensors and the resultant time-difference-of-arrival. Analysis of the output signals can yield parameters such as the void fraction, bubble chord length and velocity.

The early investigators transformed the original analog signal into a binary data series using an amplitude trigger circuit. An amplitude trigger threshold was used since the fall and rise times in the output signal were so short that a nearly square wave response was observed for the passing bubbles. A threshold voltage (V_T) was established such that for $V \geq V_T$, the active element of the optical probe was considered to be in contact with the vapor phase. Conversely, for $V < V_T$, the probe was in contact with the liquid phase. The setting of the trigger voltage level affects the accuracy of the void fraction, bubble velocity and bubble diameter. A detailed description of the analysis methods is presented in Chapter 3 of this thesis.

2.5.2   Gamma Densitometer System

A gamma densitometer can be used to measure volumetric void fractions in two-phase flows. It consists of a shielded radioactive source located on one side of the test

section and a gamma detector on the opposite side. The gamma beam is aligned normal to the test section axis. The wide beam from the radioactive source is collimated and directed through the test section. It usually covers the entire cross-section for an area-average measurement. Void fraction profiles can be obtained by using a narrow beam directed through the test section [71]. The densitometer signal resolution depends on the energy spectra of the source and the sensitivity of the signal processing system.

The gamma densitometer provides a direct measurement of the density of the two-phase mixture in the path of the gamma beam through the relationship [71]:

$$\rho = \frac{\ln(I_0 / I)}{\mu_t} \qquad (2\text{-}47)$$

where I_o and μ_t are calibration constants obtained from gamma count measurements at each desired measurement position, with an empty and liquid-filled test section and I is the count rate measured for the two-phase test condition. The two-phase density is related to the void fraction and vapor and liquid densities through the relationship:

$$\rho = (1-\alpha)\rho_l + \alpha\rho_g \qquad (2\text{-}48)$$

The primary limitations of the gamma densitometer system are the long counting time, limited spatial resolution and the near-wall measurement difficulty.
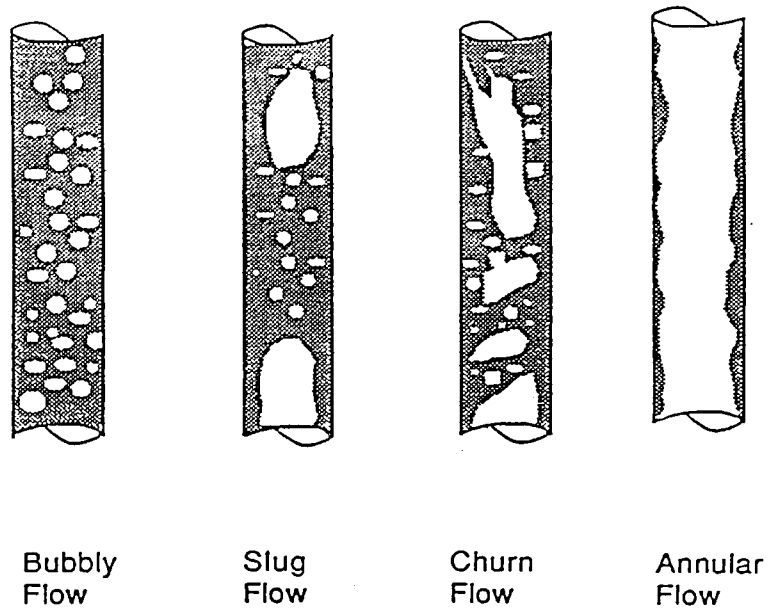
Bubbly
Flow

Slug
Flow

Churn
Flow

Annular
Flow

Figure 2.1   Schematics of flow patterns in vertical pipes
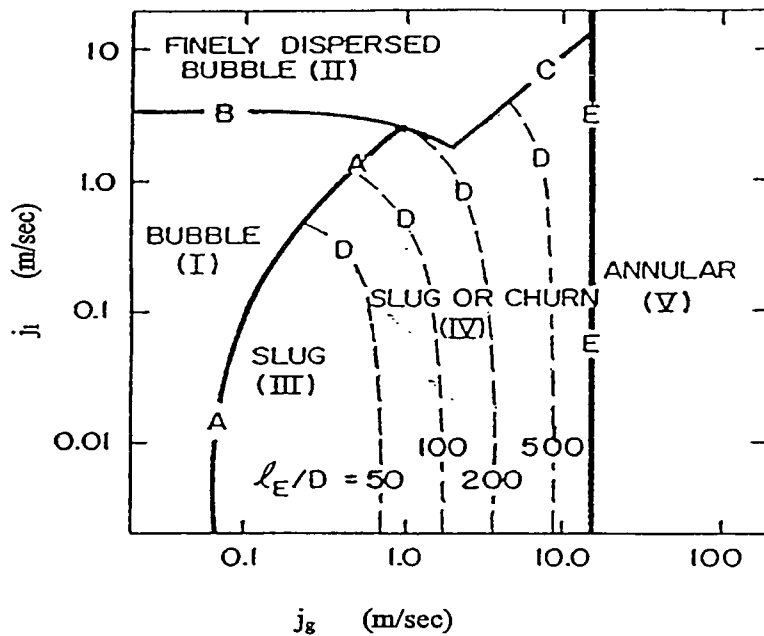

Figure 2.2   Flow regime map of Taitel et al. for air-water at 25°C and 0.1MPa in 5cm diameter vertical pipes
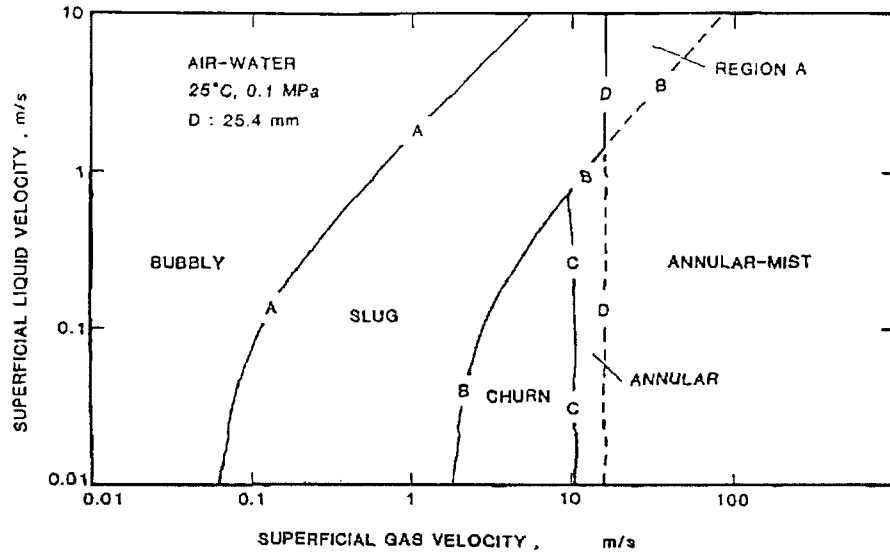
Figure 2.3   Flow regime map of Mishima and Ishii for air-water in 2.54cm diameter vertical pipes
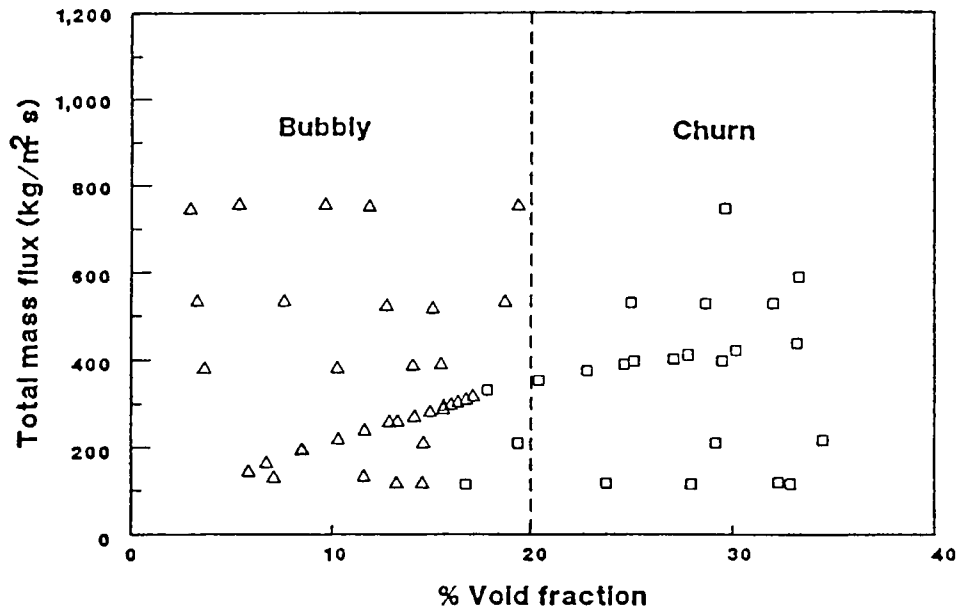

Figure 2.4   Flow regime map of Nada et al. for air-water in 20cm large diameter vertical pipes
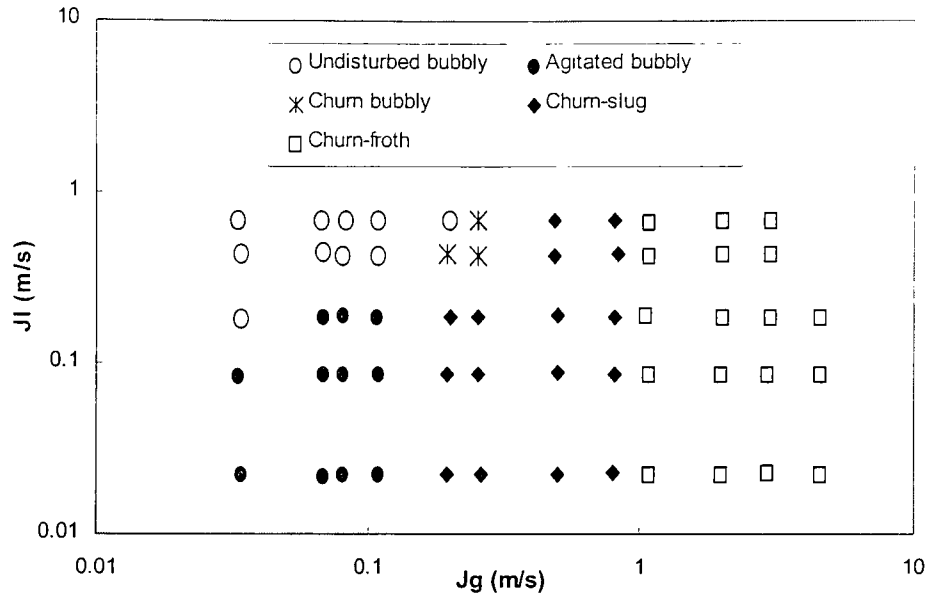
Figure 2.5   Flow regime map of Ohnuki et al. for air-water in 20cm large diameter vertical pipes
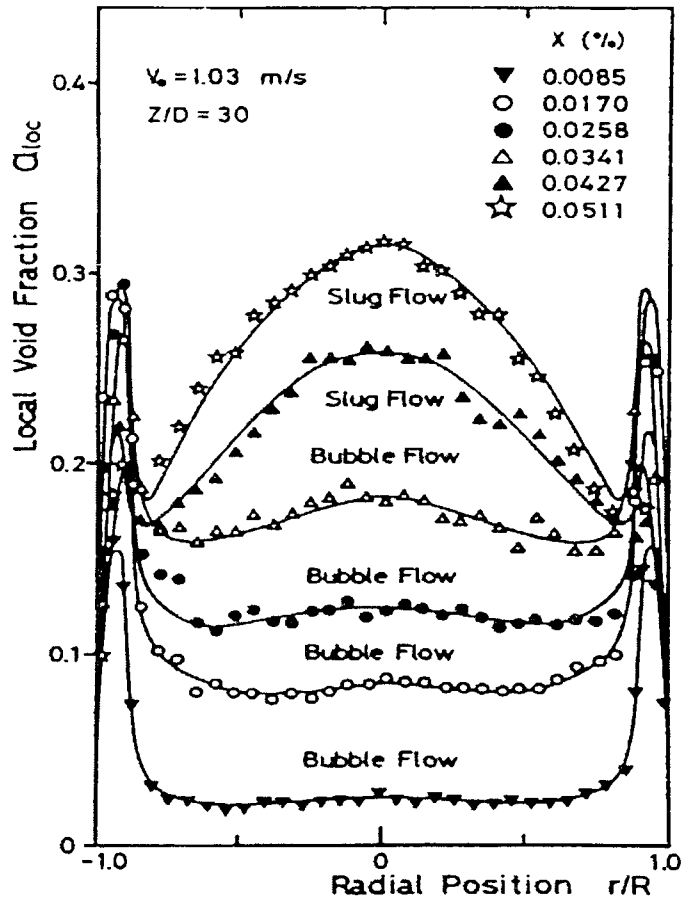
Figure 2.6   Void fraction profiles in 6cm small diameter pipes [34]
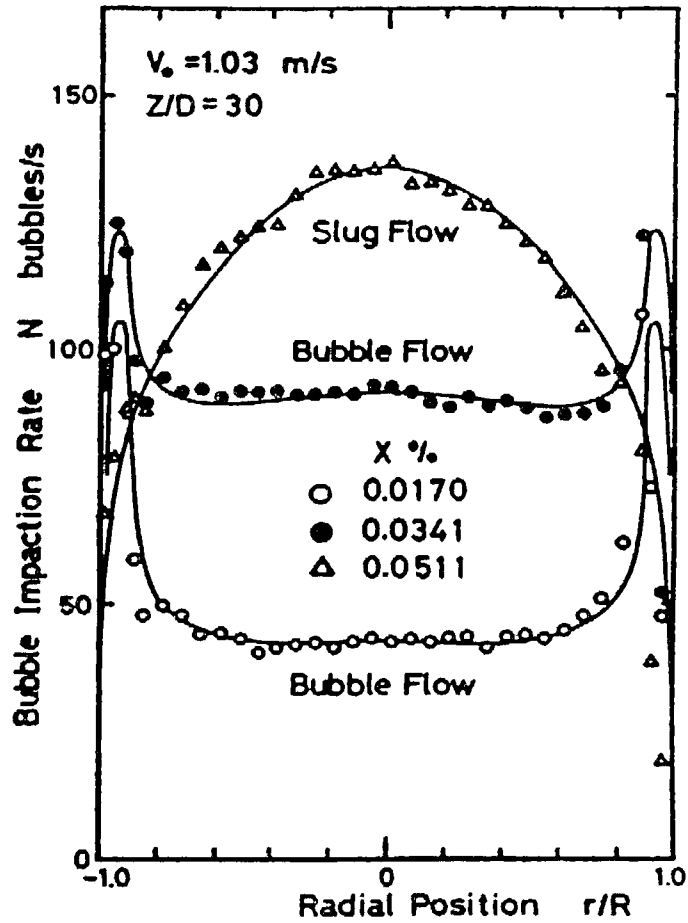
Figure 2.7   Bubble frequency profiles in 6cm small diameter pipes [34]
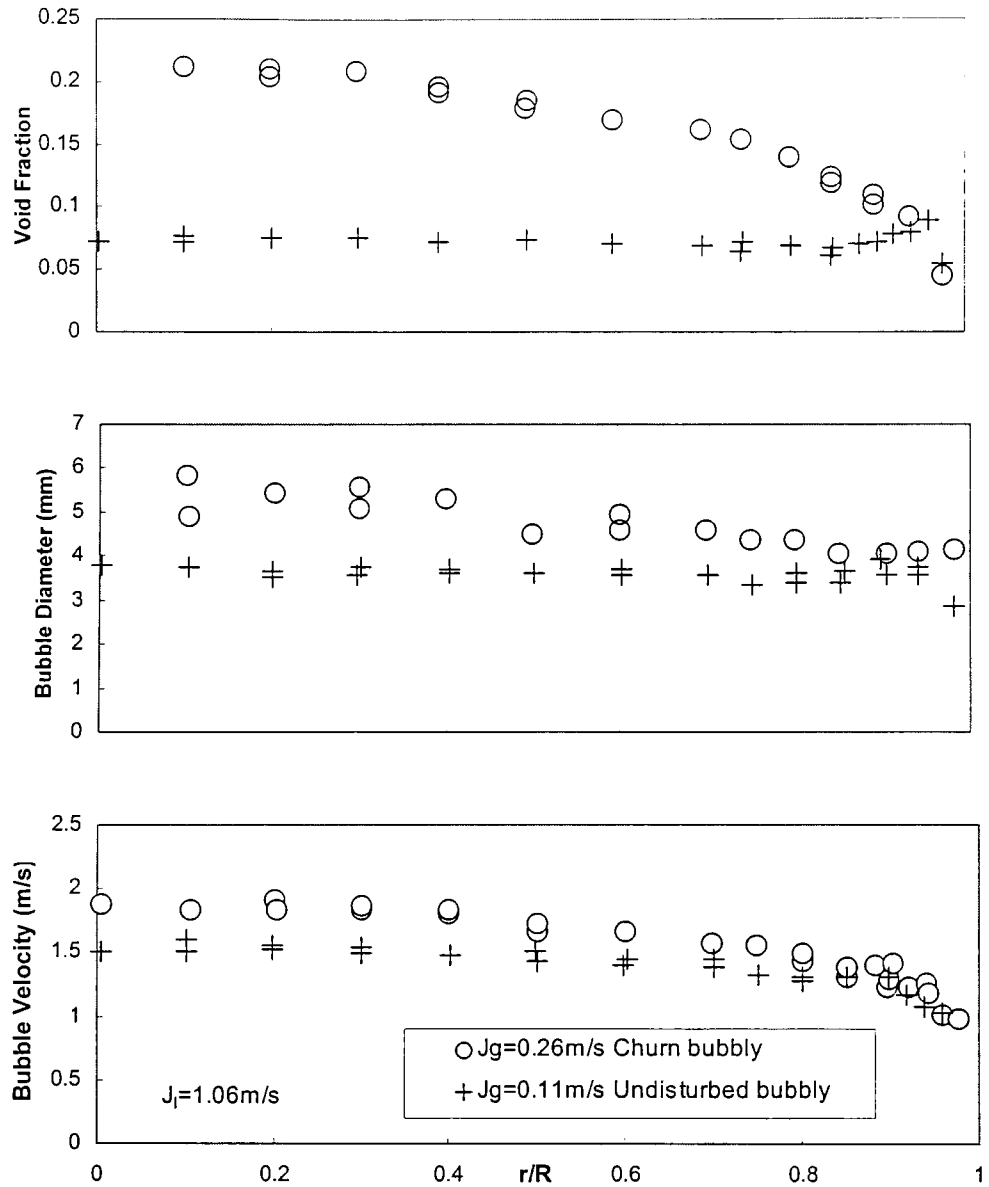
Figure 2.8   Radial distribution of bubble characteristics in air-water flow in 20cm diameter vertical pipes [14]

Chapter 3

Experimental Facilities and Data Reduction

The experiments were performed in a vertical 20cm diameter air-water two-phase flow loop, where the flow was circulated in a natural or a forced mode. The flow patterns were identified visually with the assistance of a 1000 frames per second flow imaging system. The gas bubbles or gas voidage were characterized using a dual optical probe. The flow loop, instrumentation and data reduction procedures are described in detail in this chapter.

3.1 Two-Phase Flow Loop

The flow loop is designed to study two-phase air-water flows in a 20cm diameter vertical pipe. The vertical section of the loop has a total height of 9.56m and spans three floors. A schematic of the flow loop is shown in Figure 3.1. The loop is essentially that was used by Stankovic [11] and Gerges [12]. The detailed design of the loop is presented here for completeness. The test section is located 42 diameters downstream from the

point where the air is introduced into the liquid flow. Pictures of the flow loop showing the test section with the data acquisition system located on the third floor and the flow control section in the first floor are presented in Figure 3.2 and Figure 3.3. The main components of the test facility include the riser pipe, downcomer pipe, phase separation tank, pump, bubble generator, air injection system and data acquisition system.

The two-phase flow circulates in the loop in either natural of forced mode. The natural circulation is induced by the hydrostatic head difference between the riser section and the downcomer section, while a stainless steel centrifugal pump is used for the forced circulation mode. Water from the municipal mains and compressed air are used as the liquid and gas phases. The air is injected into the water using a bubble generator and the co-current two-phase fluid flows vertically upward through the riser pipe. The air in the two-phase flow is completely separated in the phase separation tank located at the top of the riser pipe, and the water returned through the downcomer pipe. The riser is made of 20cm inner diameter transparent acrylic pipes and runs parallel to the 10cm downcomer pipe with a 1.8m separation distance between the two pipes. The end of the riser extends 0.5m into the separation tank to completely discharge the two-phase mixture to a level higher than the water level in the tank to improve phase separation. Most measurements and observations were executed at the test section located on the riser pipe.

The test section is located about 1.17m below the bottom of the phase separation tank on the riser pipe. The static pressure difference across the test section was measured 1m apart for estimating the volume-averaged void fraction. At the low flow rates of interest to this experiment, the differential pressure gives accurate enough void fraction measurements because the frictional losses are negligibly small. The phase separation tank is made of stainless steel and has dimensions 2.25m long, 0.93m wide and 0.79m height. The air is discharged into the environment from four openings at the top of the

tank. A deflector plate and a baffle were set at the higher elevation in the tank to improve air separation and reduce flow disturbances. The water level in the tank is observed through a sight glass on the riser side of the tank. The ideal static water levels in the tank for natural and forced circulation to ensure complete separation of the phases were about 20cm and 40cm respectively [12]. A 5cm diameter hose attached 14.2cm lower than the air discharge openings was used to discharge the overflow water. The downcomer pipe is a 10cm inner diameter PVC pipe with a 1.3m transparent section 1m below the outlet of the separation tank. The transparent section is used to ensure only single-phase water is returned back. An orifice plate, with diameter ratio $\beta = 0.6$, is used to measure the water flow rate downstream of the transparent section in the downcomer. The stainless-steel centrifugal pump, which is used for the forced circulation mode, is installed in the bypass line at the bottom between the riser and downcomer pipe with three gate valves for controlling the water flow rate. The pump has a volumetric rate of 450USGPM at 10m head.

The bubble generator at the bottom of the riser consist of a circular showerhead-like sieve with a large number of 0.1cm diameter holes spread evenly and covers the whole area of the riser inlet. A honeycomb flow straighter and a coarse grid mesh were installed downstream of the circular disk to reduce bubble swirl and improve radial bubble distribution [12]. The compressed air passes through an orifice plate ($\beta = 0.2$) and is filtered and regulated before entering the bubble generator. The temperature and pressure of the air is measured just downstream of the orifice plate.

To facilitate control of the flow conditions from the third floor, an automatic control valve with a positioner was installed on the air inlet line. It consists of a 2" gate valve, a pneumatic forced positioner and a pneumatic actuator. The positioner is an opposite-force balance device manufactured by Valve Related Controls Inc. The same

source of compressed air used for the gas phase is ported to the positioner through a filter, a regulator and a lubricator in succession. The positioner controls the pneumatic actuator by modulating the flow of supply air to the actuator in response to an analog input signal from the data acquisition board. The positioner has a resolution of 0.1% of span for typical operation.

3.2 *Instrumentation*

A high-speed camera, manufactured by Redlake MASD Inc. was used to visualize the flow. The Redlake MASD MotionScope PCI –1000, designed as a PC peripheral for capturing high-speed digital images directly in the PC, has a record rate up to 1000 frames per second. The system consists of a high-speed camera, full size PCI camera control and frame storage board (on-board memory), with software for calculating bubble velocities. Although the bubble velocity and size can be measured using the camera software, the pipe wall curvature distorts the 2-D image required for accurate measurements. The high-speed camera in this instance was used only for observing the flow regimes and calibrating the dual optical probe.

The air and water flow rates were measured using standard orifice plates. The differential pressure ΔP across the orifices were measured using Validyne pressure transducers. The water or air flow rate Q_k is calculated as:

$$Q_k = \frac{\rho_{op}}{\rho_k} \cdot K_k \cdot Y_k \cdot \beta_k^{\,2} \cdot A_k \cdot \left(\frac{2 \cdot \Delta P}{\rho_k} \right)^{1/2} \quad (k = l, g) \qquad (3\text{-}1)$$

where A_k is the pipe flow area, ρ_k, ρ_{op} are mass density at the test section and the orifice plate and the other parameters are as listed in Table 3.1:

Table 3.1   Parameters for flow rate calculation from orifice plate measurements

Parameters	$k = l$ (Liquid phase)	$k = g$ (Gas phase)
β_k (Diameter Ratio)	0.6	0.2
K_k (Flow Coefficient)	0.65~0.66	0.6
Y_k (Compressibility Factor)	1	Y_g
D_k (Pipe Diameter)	0.10 m	0.05 m

The compressibility factor of the gas phase Y_g is calculated as:

$$Y_g = \left[r^{\frac{2}{k}} \cdot \left(\frac{k}{k-1} \right) \cdot \left(\frac{1 - r^{\frac{k-1}{k}}}{1 - r} \right) \cdot \left(\frac{1 - \beta^4}{1 - \beta^4 \cdot r^{\frac{2}{k}}} \right) \right]^{\frac{1}{2}} \qquad (3\text{-}2)$$

where air is assumed as an ideal gas, the ratio of specific heats $k = \dfrac{c_p}{c_v} \approx 1.4$ and the pressure ratio around orifice plate is defined as $r = \dfrac{P_2}{P_1} = 1 - \dfrac{\Delta P}{P_1}$.

The flow temperatures are measured using type K thermocouple and a dual optical probe is used to measure the gas bubble characteristics such as bubble velocity, size and void fraction at the test section. The data from the pressure transducers, thermocouples and optical probes were acquired using a 16-bit A/D National Instruments SCB-68 board. The SCB-68 is a shielded I/O connector block for interfacing analog and digital I/O signals to a plug-in real-time on-board signal processing and control DAQ device AT-MIO-16X board. There are eight analog input interfaces and one analog output interfaces. The analog output signals are transmitted from the DAQ board to control the

pneumatic actuator on the air inlet line. The instruments connected to the board together with the ranges and associated accuracy are list in Table 3.2. The data was logged into a Pentium III personal computer with LabVIEW software. The data processing algorithms were developed using MATLAB.

Table 3.2   Location and range of instruments

Label	Range	Location	Accuracy
T.C. 1	0-200°C	Thermocouple at test section	±2.2°C
T.C. 2	0-200°C	Thermocouple at air inlet line	±2.2°C
P.T. 1	±3PSI	Pressure transducer at air orifice	±0.0075PSI
P.T. 2	±5PSI	Pressure transducer at water orifice	±0.0125PSI
P.T. 3	±1.5PSI	Pressure transducer at test section	±0.00375PSI
P.T. 4	±30PSI	Pressure transducer at air line	±0.075PSI
O.P. 1	0-10V	Upstream optical probe	0.01526V
O.P. 2	0-10V	Downstream optical probe	0.01526V
V.A.	0-100%	Analog output for valve V9	±0.01%

3.2.1   Dual Optical Probe

For a better understanding of two-phase flow phenomena, it is necessary to investigate the local flow quantities such as the void fraction, bubble size and upward bubble velocity. These local parameters are measured using a dual optical probe in this instance. Optical probes are basically used as a phase identifier of the two-phase flow. The main components of the dual optical fiber probes are shown in Figure 3.4. The incident beam is generated from a Helium Neon laser source 05-LHR-131 (Melles Griot)

and transmitted through two identical fiber optic fibers with 0.01cm outer diameter. The horizontal separation distance of the two tips is 0.1cm, and the separatism in the stream wise direction is 0.12cm.

The operation of the optical probe is based on the difference in the optical properties of the gas and liquid phases. The light beam passing into the flow through the optical fiber is either reflected back along the return fiber at the probe tips or refracted into the liquid (Figure 3.5). The beam is completely reflected when the probe tip is in contact with the gas and only partially reflected when in contact with the liquid phase. The different intensity representing the different phases are translated into voltage signals via a photo-multiplier and then amplified and recorded by the DAQ board. A sample voltage output from the dual optical probe as a function of time is shown in Figure 3.6. The sample was collected by upstream and downstream sensors simultaneously in a bubbly flow pattern. Although some noise is present in the ideal square-wave output signals, the output voltage corresponding to the liquid and gas phases are significantly different. A typical bubble detected by the upstream probe is highlighted in Figure 3.6. As the bubble interface contacts the upstream probe, the voltage signal increases sharply from the lower voltage to the higher voltage, and then back to lower voltage when the probe comes in contact with water. The increase and decrease identifies the individual phases and the time that they are in contact with the probe. Each pair of increase and decrease can be considered as a complete bubble passing through the probe.

3.2.2   Sampling Time and Frequency

The vertical separation distance of the two probes is determined by several factors, such as the bubble size, velocity and sampling frequency. If the distance is too

small, the accuracy of the time difference of the bubble traveling through the two probes will be lower, which will require a higher sampling frequency, while if the vertical distance is too large it will decrease the probability of the same bubble hitting both probes [12]. The measurement precision increases with the sampling frequency f and sampling time T. However, due to limitations in the A/D board and computer storage and processor capability, an optimum sampling frequency and time for the present conditions were determined.

The bubble velocity u_b was calculated from the time interval Δt of the contact of the bubble interface on the two probe tips and the vertical probe separation distance L_v =0.12cm.

$$u_b = \frac{L_v}{\Delta t} = \frac{L_v}{\Delta N / f} \tag{3-3}$$

The time interval Δt for the bubble interface to travel the distance between the two probes is equal to the number of samples ΔN divided by the sampling frequency f. At a higher bubble velocity u_b, Δt will be smaller and a higher sampling frequency f is required to have the necessary temporal resolution.

Because of the discrete nature of the sample number ΔN, Δt is also a discrete variable, which results in discrete bubble velocities. For this experiment, the average bubble velocities are less than 3m/s, the measurements for the bubble velocity less than 4m/s will have precision no more than 1m/s at the sampling frequency 10kHz and the precision at this velocity is 0.6m/s for a sampling frequency of 20kHz. Different sampling times were tested to determine the appropriate time for statistically steady results. The standard deviations δ of void fraction for the population of measurements from which the observation was taken are listed in Table 3.3 for different sample times.

A sampling time of 180s with frequency of 20kHz for bubbly flow and 300s with 10kHz for transition and churn flow was used for the present experiment.

Table 3.3   Sampling time and standard deviation at sampling frequency of 10kHz

Sampling time T (s)	Standard deviation of the population δ_α (%)
60	5.688
180	2.795
240	2.218
300	1.872

3.3   Test Procedure

The experiments were performed over a range of flow conditions at room temperature. The bubble characteristics in the test section were obtained by traversing the optical probe along a pipe radius. Twenty-one different flow conditions were investigated in this study. To study the flow transition from bubbly to churn flow, the experiments were performed at three different superficial water velocities j_{water} (0.25, 0.35 and 0.45m/s). At each constant j_{water}, the flow patterns were obtained by varying superficial air velocities j_{air} from 0.02 to 0.24m/s. The test conditions are given in Table 3.4, extended from previous investigation in the same flow loop ranged as $0.022 \leq j_{air} \leq 0.055$m/s and $0.02 \leq j_{water} \leq 0.4$m/s at low void fraction by Gerges [12]. Each flow condition is designated by a letter followed by a number, e.g. B3. The cross-sectional averaged void fraction $<\alpha>$

$$\langle \alpha \rangle = \frac{\int_0^R \alpha(r) \cdot r dr}{\int_0^R r dr} \qquad (3\text{-}4)$$

is also presented in Table 3.4. For each flow condition, the fiber optical probe was traversed along the radial direction, and measurements were obtained at twenty-one locations along the pipe radius. From r/R=0 to 0.4, measurements were obtained at intervals of 1cm, while from r/R=0.5 to 0.65 the interval was 0.5cm and from r/R=0.70 to 0.975 the interval was 0.25cm.

Table 3.4   Experimental flow conditions

j_{air} (m/s) j_{water} (m/s)		0.02	0.10	0.12	0.14	0.16	0.20	0.24
0.25	Case	A1	A2	A3	A4	A5	A6	A7
	$\langle\alpha\rangle$	0.049	0.149	0.161	0.168	0.179	0.202	0.222
0.35	Case	B1	B2	B3	B4	B5	B6	B7
	$\langle\alpha\rangle$	0.017	0.146	0.155	0.165	0.177	0.197	0.216
0.45	Case	C1	C2	C3	C4	C5	C6	C7
	$\langle\alpha\rangle$	0.019	0.140	0.151	0.160	0.165	0.184	0.224

Flow Patterns: | Bubbly | | Transition | | Churn |

3.4 Data Reduction

The significant parameters that characterize two-phase flow are the local void fraction, bubble velocity and bubble or gas void size distributions. These parameters describe the local flow conditions of steady-state two-phase flow, both qualitatively and quantitatively. Hence, accurate information on these flow variables and the generalized relationships among them are necessary to understand the transport phenomena of two-phase flows.

3.4.1   Phase Discrimination

The output signal from an optical probe is a square wave with superimposed noise where the high and low voltage represents the gas and liquid phases. The ideal voltage signal obtained from a dual optical probe is shown schematically in Figure 3.7. A voltage threshold trigger, normally 10% of the voltage differences over the minimum voltage, is usually used to distinguish between the gas and liquid phases [12]. The voltage signal is translated into a binary dispersed-phase density signal X, where

$$X(t) = \begin{cases} 1 \ (V \geq V_T) \ \text{when the tip is in the vapor phase at time } t \\ 0 \ (V < V_T) \ \text{when the tip is the the liquid phase at time } t \end{cases} \tag{3-5}$$

For a low sampling frequency f, a fixed voltage trigger is relatively reliable because the signals from the probe are essentially rectangular, and hence the void fraction measurements are rather insensitive to the trigger level position. However, at a higher sampling frequency, the voltage signals display a slope due to the finite response time of the probe to the different phases. Although an amplitude voltage trigger is good enough to distinguish each bubble passing the probe, it may introduce errors for the bubble

velocity measurement since an accurate time-difference of arrival at the two probes is necessary. The actual signal corresponding to the passage of a bubble is shown in Figure 3.8. Using the amplitude voltage trigger, the phase change corresponding to the bubble face and back striking the sensor are located at points A and B. However, the actual phase change occurs at points A' and B'. An improved phase discrimination method suggested by Liu and Bankoff [8] is used in the present work, where in addition to the amplitude threshold, the first-order time derivative of the signal is used to distinguish the time at which the interface strikes the probe. Once the phase-change point A and B are determined by the amplitude threshold, a backward and forward searching scheme is used to more accurately locate the phase-change points.

The bubble chords calculated from the two methods were compared to measurements from the high-speed camera. The improved phase discrimination method gives results closer to the measurement from the high-speed camera than the results obtained from the amplitude threshold method.

Table 3.5   Bubble chord measured by different methods

Method	Amplitude Trigger	Improved Slope Trigger	High-Speed Camera
Bubble chord length	4.0 mm	4.1 mm	4.2 mm

The data used to calculate bubble diameter and velocity are processed only on successful signals, where the bubble hits the front probe and then the rear probe within a narrow region close to its center axis. The signals are filtered according to the above criteria before the bubble characteristics are estimated to ensure only the qualified

bubbles are analyzed [12]. There are three criteria suggested by Kocamustafaogullari &
Wang [73] that must be satisfied in the data processing:

1. Upward moving bubbles hit the upstream probe before the downstream one

$$t_{uf,i} < t_{df,i} \text{ and } t_{ub,i} < t_{db,i} \qquad (3\text{-}6)$$

2. To ensure the same bubble is being detected, the two signal widths should be
    comparable

$$\left| (t_{ub,i} - t_{uf,i}) - (t_{db,i} - t_{df,i}) \right| \leq 0.3 * (t_{ub,i} - t_{uf,i}) \qquad (3\text{-}7)$$

3. The time differences Δt_{min} and Δt_{max} between the front and rear probe signals
    are the time limits corresponding to the possible maximum and minimum
    bubble velocities.

$$\Delta t_{min} \leq t_{df,i} - t_{uf,i} \leq \Delta t_{max} \text{ and } \Delta t_{min} \leq t_{db,i} - t_{ub,i} \leq \Delta t_{max} \qquad (3\text{-}8)$$

Therefore, the Δt_{min} and Δt_{max} should be determined by the combination of the vertical
distance between the two probe tips L_v and the flow conditions such as superficial
velocities j_{air} and j_{water}.

3.4.2   Bubble Frequency and Void Fraction

Although data from both probes can be used to estimate the bubble frequency and
void fraction, the data from the upstream probe is more reliable since the bubbles tend to
distort after they impact the upstream probe. The bubble deflection due to the upstream
probe will also reduce the sensitivity of the downstream probe to some bubbles and result

in an underestimation of the measured void fraction. Hence, the number of bubbles was measured using the signal from the upstream probe. Each square wave indicates a bubble passing through the optical probes (Figure 3.7). The local void fraction at each radial position was calculated as the ratio of probe residence time in the void to the total sampling time.

$$\alpha(r) = \lim_{T \to \infty} \left(\int_0^T X(t)dt / T \right) \tag{3-9}$$

or

$$\alpha(r) = \frac{\sum_{i=1}^{i=N} (T_{gi})}{T} \tag{3-10}$$

where T is the total sampling time, N is number of bubbles flowing through the probe tip during the sampling time T and T_{gi} is the residence time of the probe in the gas phase.

The cross-sectional void fraction is estimated by integrating the measured local void fraction $\alpha(r_i)$ over the cross section as:

$$<\alpha> = \frac{\sum_{i=1}^{21} 2 \cdot \pi \cdot r_i \cdot (r_i - r_{i-1}) \cdot \alpha(r_i)}{A} \tag{3-11}$$

The average volumetric void fraction was also obtained by measuring the pressure difference (ΔP) 1m apart in the stream-wise direction at the test section location:

$$\rho = \rho_g \cdot \langle \alpha \rangle + \rho_l \cdot (1 - \langle \alpha \rangle) \tag{3-12}$$

$$\Delta P = \rho_l \cdot g \cdot \Delta H_l = g \cdot \Delta H \cdot \rho - \Delta P_f \tag{3-13}$$

where ΔH_l is the liquid height corresponding to pressure drop between test sections;

ΔH refer to the distance between two station tanks, 1m;

ΔP_f is the frictional pressure drop.

The void fraction $<\alpha>$ measured by the pressure difference is compared with the cross-sectional void fraction measured by upstream and downstream optical probes processed with the amplitude and improved slope trigger methods in Figure 3.9. The measurement from the upstream probe and processed with the improved slope trigger method is closer to the volumetric void fraction estimated from the pressure difference with a maximum difference of ±12.1%. The comparison indicates the upstream probe has better accuracy than downstream probe, and the improved slope trigger method is better than the amplitude one.

3.4.3   Bubble Velocity and Diameter

Bubble velocity is determined using the signals from the two probes by measuring the time-difference-of-arrival of the interface at the two sensors. As shown in Figure 3.7, there are two interfaces (face and back) that hit the probe tips successively. The bubble velocity in this instance is calculated from the measurements from bubble face by Equation (3-3).

The probability of the bubble circumferential location where it strikes the probe is equal, so the measurements yield the distribution of bubble chord lengths rather than bubble diameter. Bubble chord length was calculated from the bubble velocity and the time interval (Δt) for the bubble face and back to pass through the probe.

$$x = u_b . \Delta t \qquad\qquad (3\text{-}14)$$

To convert the bubble chord length measurement into a diameter, two methods can be used. One is through statistical methods, whereas the other uses a filter method that considers only the bubble signals where its center flows through the probes [12]. In the first method, the bubble diameter can be obtained from the probability density function of the bubble chord length. Assuming spherical shaped bubbles, the bubble diameter at a given radial location can be estimated as [74]:

$$\overline{d}(r) = 1.5 \int_0^\infty x \cdot PDF(x)dx \qquad (3\text{-}15)$$

where $\overline{d}(r)$ is the local average bubble diameter

x is the axial bubble chord length

$PDF(x)$ is the probability density function of bubble chord length

The second method compares the bubble chord measured by the two probes simultaneously and estimates the diameter only if they are within criterion C of each other.

$$\frac{\left| x_{upstream} - x_{downstream} \right|}{x_{upstream}} \leq C \qquad (3\text{-}16)$$

The criterion C (Equation 3-16) of 5% used in the present investigation is based on the assumption of a spherical bubble model (Figure 3.10) and is more stringent than the 30% used by Gerges [12]. Two bubble chords, $x_{upstream}$ and $x_{downstream}$, are measured simultaneously by the two optical probes. If one of probe is offset from the bubble center by a distance b, then the other is at a distance $(b+L_h)$ from the center, where L_h is the horizontal distance between the two probes.

With $E = \dfrac{L_h}{r}$ and $B = \dfrac{b}{r}$, then

$$\frac{\left| x_{upstream} - x_{downstream} \right|}{x_{upstream}} = 1 - \left(\frac{r^2 - (b + L_h)^2}{r^2 - b^2} \right)^{\frac{1}{2}}$$

$$= 1 - \left(1 - \frac{2EB + E^2}{1 - B^2} \right)^{\frac{1}{2}} \qquad (3\text{-}17)$$

Using the above criterion results in an error less than 7.15% for bubble diameters or length of gas void up to 20mm.

Table 3.6   Bubble diameter estimated from different methods

Method	Statistical	Filter (C=5%)
Bubble Diameter	3.35 mm	3.40 mm

The results from the two methods show good agreement (Table 3.6). However, the sampling time should be sufficiently long enough to obtain a sufficient number of realizations to obtain a statistically steady value. The filter method is used in the current experiment to estimate the bubble diameter.

3.5 *Uncertainty Analysis*

An uncertainty analysis was performed based on the method of Moffat [72]. The uncertainty attributed to a measurement is an estimate of the possible residual error in

that measurement after all proposed corrections have been made. For each measurement, an error source is usually categorized as a fixed error and a random error, which are described by its bias limit, *B*, and its precision limit, *P*, respectively. Any error that will not change during the conduct of the experiment is a fixed error, which is usually due to inaccurate calibration of the measurement instruments. The random error (precision error) is due to the limited precision of the measurement instruments as well as the scatter in the repeated measurements.

Table 3.7   Experimental uncertainty

Results	Uncertainty $(U_R)_{0.95}$	
R	Max. %	Min. %
j_{air}	1.96	1.12
j_{water}	2.55	1.12
$<\alpha>$	1.33	1.01
$\alpha(r)$	0.42*	0.30*
x	8.49*	4.18*
u_b	4.17*	4.17*
IAC	8.50*	4.19*

*: Bias limit $(B_R)_{0.95}$

The result *R* of the experiment is assumed to be calculated from a set of measurements X_i,

$$R = R(X_1, X_2, X_3, ..., X_n) \tag{3-18}$$

For each result presented, the overall uncertainty $(U_R)_{0.95}$ is expressed as:

$$(U_R)_{0.95} = \sqrt{B_R{}^2 + P_R{}^2}$$ (3-19)

where the bias limit of the result R is estimated by

$$B_R = \sqrt{\sum_{i=1}^{n}\left(\frac{\partial R}{\partial X_i}B_{X_i}\right)^2}$$ (3-20)

The uncertainties associated with the flow rates, volumetric void fraction, local void fraction and bubble frequency, diameter, velocity and interfacial area concentration are presented in Table 3.7.

1: Riser Pipe
2: Test Section
3: Phase Seperation Tank
4: Downcomer Pipe
5: Pump
6: Bubble Generator
7: Dual Optical Probe
8: Air Filter
V: Valve
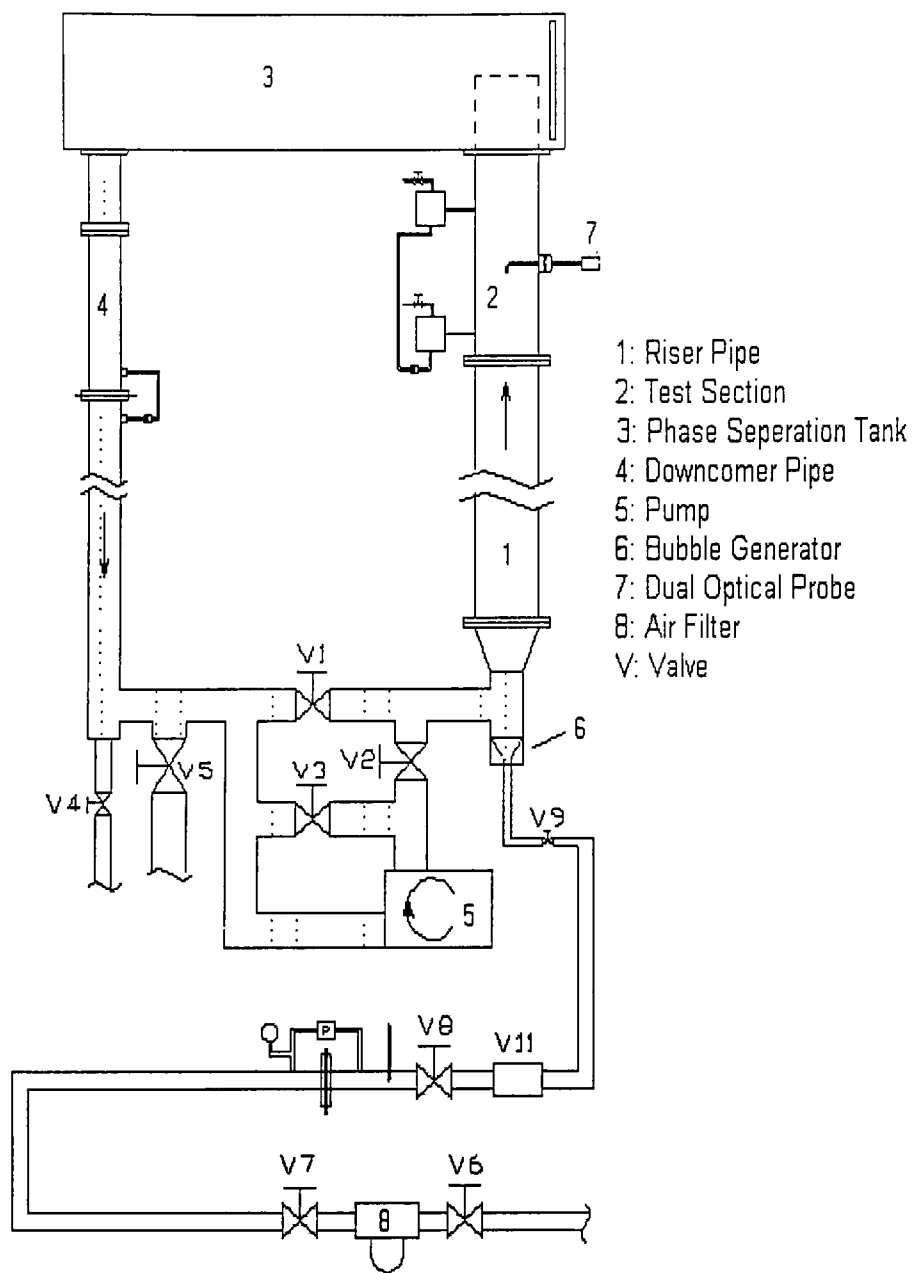
Figure 3.1   Schematic of two-phase flow loop

Figure 3.2   Measurement components in flow loop
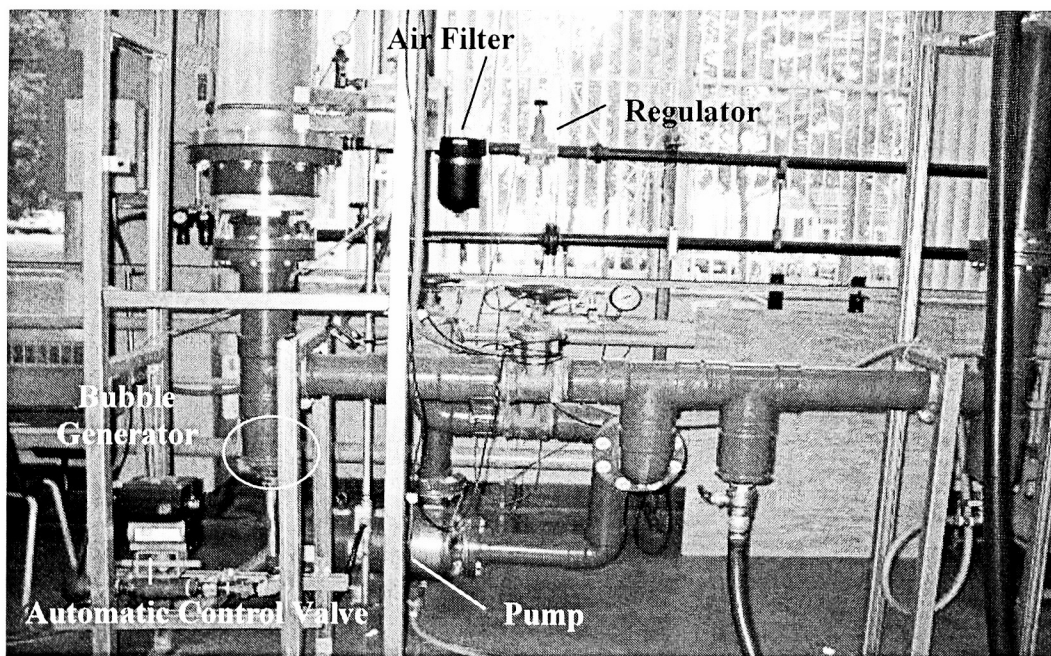
Figure 3.3   Control components in flow loop
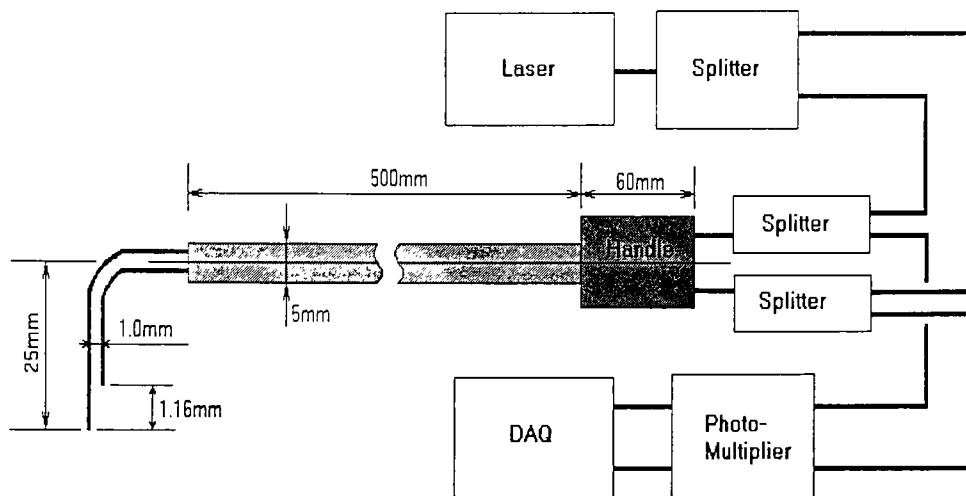
Figure 3.4   Schematics of dual optical probe

Air phase   Water phase
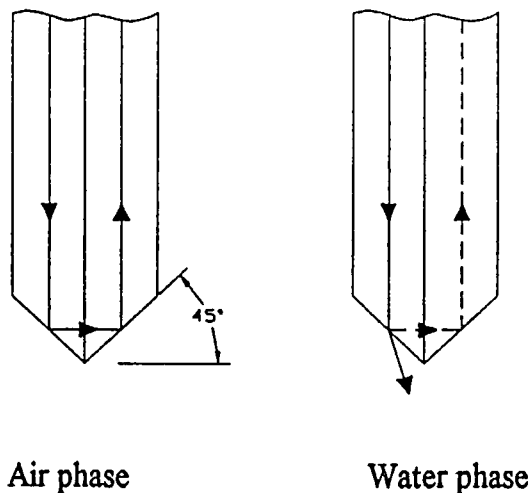
Figure 3.5   Principle of light refraction at probe tip
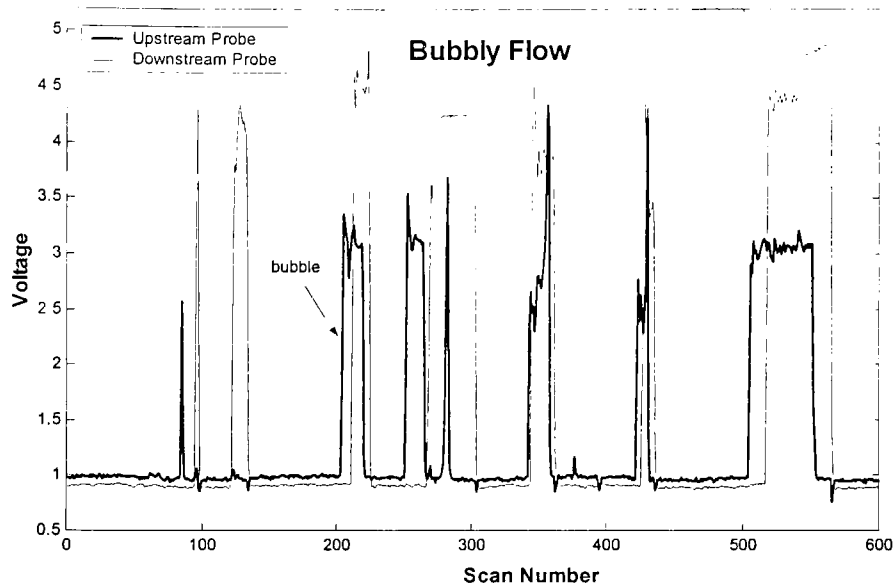
Figure 3.6   Sample of optical probe output
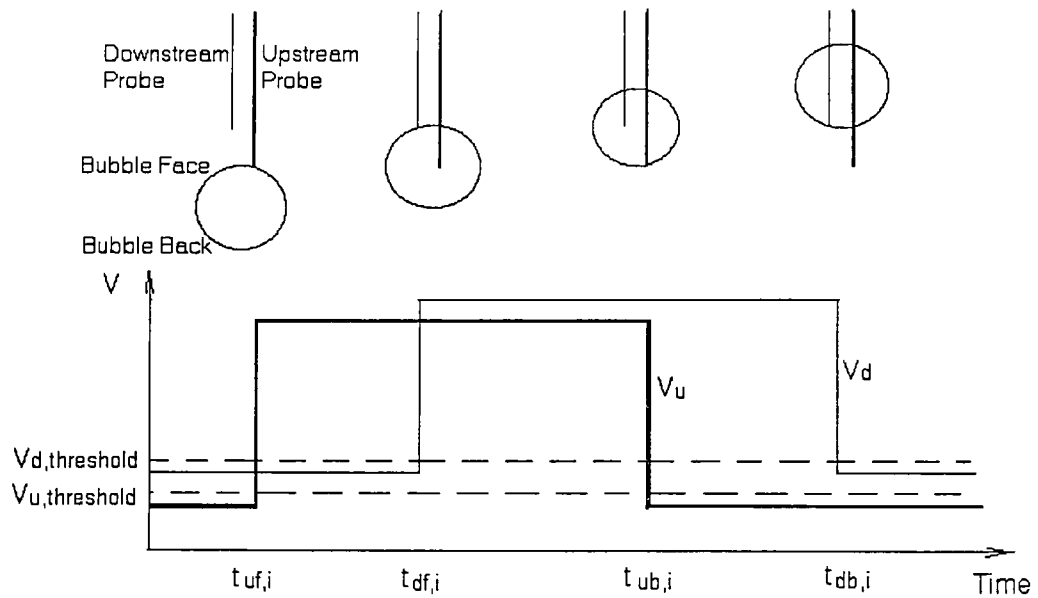
Figure 3.7   Schematics of phase identification signal from dual optical probe
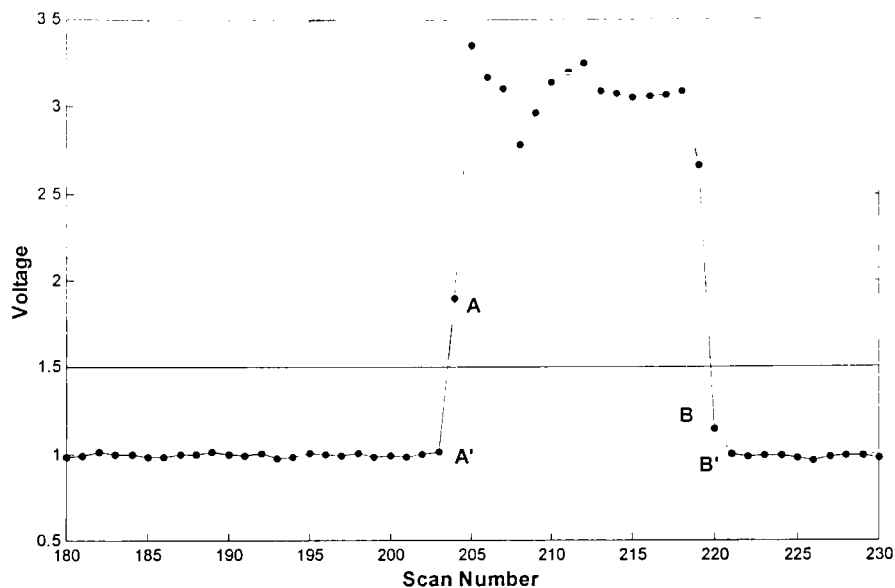
Figure 3.8   Schematics of trigger setting differences
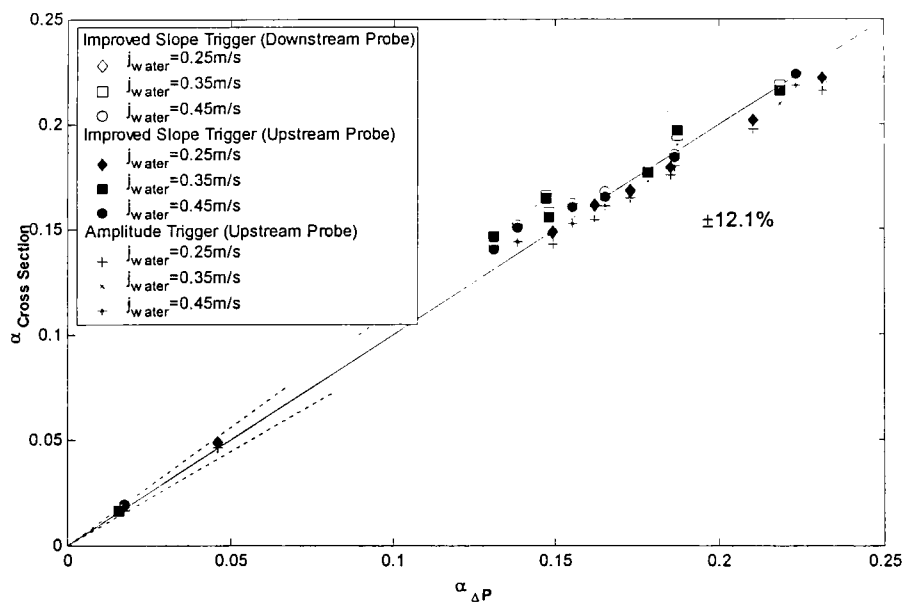
Figure 3.9   Void fraction measured by dual optical probe and pressure drop
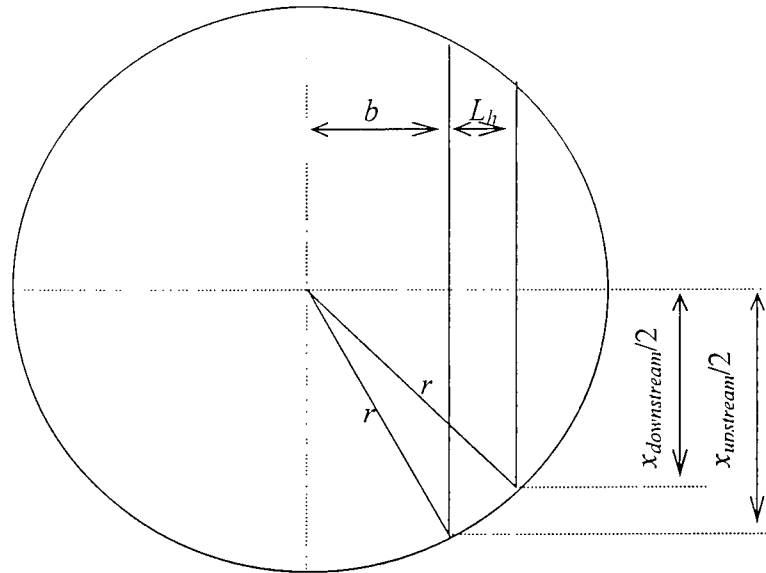
Figure 3.10   Schematic of bubble diameter filter criterion

Chapter 4

Results and Discussion

The experimental results for the flow conditions described in Chapter 3 (j_{air} in the range of 0.02 to 0.24m/s, j_{water} in the range of 0.25 to 0.45m/s) are presented and discussed in this chapter. The flow patterns and transitions observed with the aid of the high-speed camera are described in section 4.1. Profiles of bubble characteristics measured in the present facility are compared with those in small and large diameter pipes in section 4.2. The *PDF* and *CDF* of measured flow characteristics are analysed and compared in section 4.3. The radial distributions of the bubble characteristics are studied in section 4.4 as the flow pattern develops from bubbly to churn flow with increasing gas flow rate. The bubble frequency, bubble diameter, local void fraction and bubble velocity are used to characterize the flow in this instance. An attempt to calculate the Interfacial Area Concentration is presented and discussed in section 4.5. The void fractions predicted by the drift-flux models are compared with the present experimental results in section 4.6.

4.1 Flow Patterns

The flow patterns were observed with the help of a high-speed camera as a function of superficial air velocity j_{air} and superficial water velocity j_{water}. The flow patterns observed at each flow condition and their case labels are presented in Table 4.1. No slug flow was observed during the transition from bubbly to churn flow in the present facility. Slug flow is defined when gas bubbles having approximately the same diameter as the pipe, and greater in length than the tube diameter exist along with liquid slug regions where the liquid completely covers the flow area of the tube.   Similar observations have been reported in the present facility by Stankovic [11] and Gerges [12] and in other large diameter pipe facilities by Ohnuki et al. [14] [75] (*D*=20cm, 48cm), Larson [76] (*D*=30.5cm) and Cheng et al. [16] (*D*=15cm).

Table 4.1   Experimental conditions and flow patterns

j_{air} (m/s) j_{water} (m/s)		0.02	0.10	0.12	0.14	0.16	0.20	0.24
0.25	Case	A1	A2	A3	A4	A5	A6	A7
	$<\alpha>$	0.049	0.149	0.161	0.168	0.179	0.202	0.222
0.35	Case	B1	B2	B3	B4	B5	B6	B7
	$<\alpha>$	0.017	0.146	0.155	0.165	0.177	0.197	0.216
0.45	Case	C1	C2	C3	C4	C5	C6	C7
	$<\alpha>$	0.019	0.140	0.151	0.160	0.165	0.184	0.224

Flow Patterns: | Bubbly | | Transition | | Churn |

A qualitative description of the flow patterns observed using the high-speed camera for j_{water} =0.45m/s and j_{air} in the range 0.02 to 0.24m/s, corresponding to flow conditions C1 to C7 is presented in this section. The distinct discrete bubbles in case C1 (Figure 4.1(a)) move upward in a zigzag path with few collisions and coalescences between them. Thus, this flow pattern will be designated as undisturbed bubbly flow as used by Ohnuki et al. in the following discussions. Although most of the bubbles in the bubbly flows C2 and C3 have nearly spherical shapes, their motions are more random than those of C1. Bubble interactions are observed with downward motion of smaller bubbles due to the re-circulatory flow downstream of the larger bubbles. This flow pattern will be called agitated bubbly flow to distinguish it from the undisturbed bubbly flow pattern. When the agitated bubbly flow transitions into churn flow, individual large bubbles with distorted edges appear in the transition flow (C4 and C5). These unstable bubbles typically develop into Taylor bubbles to form slug flow in small diameter pipes [77]. In this case, however, as the air flow rate is further increased, more deformed and distorted larger bubbles with discrete liquid drops appear along with smaller spherical bubbles in the liquid phase, with higher levels of unsteadiness (Figure 4.1(b)). Although some larger bubbles have lengths greater than the tube diameter, they are distorted with an indistinct boundary, entirely different to Taylor bubbles in small diameter pipes.

In vertical upward flow in large diameter pipes, the transition from undisturbed bubbly to churn flow is assumed to take place because of the dominance of the turbulent break-up forces. The gas holdup in a dispersed bubble is determined from a balance between break-up forces due to turbulence, and coalescence forces due to gravity and/or surface tension [37]. Whenever coalescence forces dominate, agglomeration of small bubbles occurs, leading to the formation of a larger bubble. However, with increasing

turbulence, break-up forces will impede the further agglomeration of these larger bubbles, which ultimately lead to Taylor bubbles.

The flow patterns observed in the current facility are presented as flow maps in logarithmic and linear coordinates as a function of the superficial velocities j_{air} and j_{water} (Figure 4.2(a) and (b)). The bubbly to slug and slug to churn flow transition boundaries predicted by Taitel et al. [9] and Mishima and Ishii [24] for small diameter pipes are also shown in the figures for comparison. The bubbly-churn transition in the present facility occurs at lower j_{air} than the bubbly-slug transition in small diameter pipes according to the criterion of either Taitel et al. or Mishima and Ishii. The transition region is shown enlarged in Figure 4.2(b), along with an approximate transition boundary developed from the present experimental data. In the current facility, at a constant j_{water}, the transition from bubbly to churn occurs at a lower j_{air} than that predicted by Taitel et al. [9] or Mishima and Ishii [24] for transition from bubbly to slug flow. The bubbly-to-slug transition boundary of Taitel et al.[9] shows a better agreement with the present transition from bubbly to churn flow. The bubbly to churn transition was observed to occur around $<\alpha>$ =0.155~0.165, which agrees well with the results of Hibiki et al. [13] who found $<\alpha>$ = 0.17 for a D=10.2cm pipe at transition. This is lower than the value $<\alpha> \approx 0.20$ suggested by Nada et al. [15]. This is also lower than the criteria (0.25 and 0.30) used by Taitel et al. and Mishima and Ishii for transition from bubbly to slug flow. The bubbly to churn transition boundary in the present facility can be expressed empirically as:

$$j_{water} = 2.08 j_{air} + 0.058 \tag{4-1}$$

for the range 0.02m/s $\leq j_{air} \leq$ 0.24m/s and 0.25m/s $\leq j_{water} \leq$ 0.45m/s.

The present flow patterns are also compared with those observed by Stankovic in the same facility (Figure 4.3) and Ohnuki et al. [14] in a similar diameter pipe (D=20cm)

at *L/D*=60 with air and water as the two fluids (Figure 4.5). Although the experiments were performed in the same facility, the transition boundary observed by Stankovic occurs at a higher j_{air} for a constant j_{water}. If the density of the compressed air used by Stankovic for calculating the superficial velocities is replaced by the density at the test section, the modified flow map (Figure 4.4) shows a better agreement with the present flow map. It should be noted that Ohnuki et al. defines several flow patterns: undisturbed bubbly, agitated bubbly, churn bubbly, churn slug and churn froth. If the undisturbed bubbly and agitated bubbly can be treated as bubbly flow and churn bubbly as transition flow with churn slug and churn froth as churn flow, then the flow patterns observed in the present facility are in good agreement with the observations of Ohnuki et al. Due to the subjective discrimination of the flow patterns, especially around the transition flow patterns, the boundaries developed by different researchers can be thought similar if they are all located within a transition region.

4.2   Comparison with Data in Small Diameter Pipes

To understand the effect of the pipe diameter on the two-phase flow parameters, such as bubble frequency, bubble diameter, local void fraction and bubble velocity, the present experimental data are compared with other studies in both small and large-diameter pipes. It should be noted that the radial void fraction profiles in the present facility are in good agreement with the results of Gerges and Ohnuki et al. at similar flow conditions in a similar diameter pipe (Figure 4.6).

4.2.1   Bubble Frequency

The radial distributions of bubble frequency are compared with bubbly flow in a smaller diameter pipe (*D*=0.038m, Liu and Bankoff [8]) and bubbly flow in the same facility by Gerges [12] in Figure 4.7. The bubble frequency of the bubbly flow in the small diameter pipe has a saddle shaped profile with a distinct peak near the wall and a relatively flat profile in the core. It has been suggested that the peak in the bubble frequency profile near the wall in small diameter pipes is due to the longer stagnation period caused by adherence or reflection of the bubbles at the surface of the wall [34]. In the present experiments, an almost flat profile with a slight increase close to the wall is observed in undisturbed bubbly flow (j_{air}=0.02m/s, j_{water}=0.35m/s) at very low void fractions. In agitated bubbly flow (j_{air}=0.10m/s, j_{water}=0.35m/s) the profile is parabolic. Although the maximum bubble frequencies occur at different radial positions, *r/R*=0.9 and 0.975, for the 0.038m and 0.20m diameter pipes, the distance from the maximum to the pipe wall is almost equal and close to their average bubble radius, ≈2mm (Figure 4.9). The maximum bubble frequency is moved from pipe wall to the pipe center as the flow transitions from undisturbed bubbly to agitated bubbly and churn flow. The bubble frequency for agitated bubbly flow and bubbly flow in the 0.20m and 0.038m diameter pipes are close in the pipe central region (*|r/R|<0.4*). The bubble frequency in agitated bubbly flow in the present facility, however, continues to decrease as the wall is approached, while for the case of bubbly flow in the smaller diameter pipe, it remains relatively flat with a sharp peak very close to the wall (*|r/R|* ≈ 0.9). In the churn flow in the present facility, the radial distribution has a core-peak shape similar to that in agitated bubbly flow, except that the bubble frequency is higher at any given radial position because of the higher j_{air}.

4.2.2   Bubble Diameter

The bubble diameter profiles of undisturbed bubbly flow C1 and agitated bubbly flow A1 are compared with the measurements of Gerges [12] and Ohnuki et al. [14] in Figure 4.8. The bubble diameter is almost constant at about 3.9mm through the entire cross section for undisturbed bubbly flow. For the bubbly flow in the present experiment, the average bubble size decreases from about 5.7mm to 3.9mm at the pipe centreline as j_{water} increases from 0.25m/s to 0.45m/s at a fixed j_{air} of 0.02m/s. Unlike the profiles of Gerges or Ohnuki et al., a wall-peak profile is not observed in either undisturbed bubbly or agitated bubbly flow in the current experiments. The bubble diameter profile is relatively flat in undisturbed bubbly flow and has a parabolic shape in agitated bubbly flow in the present facility.

The bubble diameter profiles are also compared to those measured in smaller diameter pipes by Liu and Bankoff [8] for bubbly flow (Figure 4.9). The average bubble diameter at the pipe centreline increases from about 4.0mm to 12.1mm as the flow transitions from undisturbed bubbly to churn flow as j_{air} increases from 0.02m/s to 0.24m/s with constant j_{water} of 0.35m/s. The bubble diameter profile of undisturbed bubbly flow in the current facility is similar to that of Liu and Bankoff, with the profile almost uniform over the cross section of the pipe with a bubble diameter of about 3.9mm. As the air flow rate is further increased, the average bubble diameter increases with a core-peak profile for churn flow.

4.2.3   Local Void Fraction

The local void fraction profiles of bubbly flow are compared with data of Stankovic [11], Gerges [12] and Ohnuki et al. [14] (*D*=0.20m) in Figure 4.10. At very

low void fractions, there is a small increase close to the wall in undisturbed bubbly flow and is similar to that observed by Stankovic and Ohnuki et al. The maximum near-wall void fraction, however, is significantly smaller than the peak of Stankovic and Ohnuki et al. Stankovic observed that the wall peak profiles are presented at void fraction below 0.04, while Ohnuki et al. (D=20cm and L/D =60) found the wall-peak at void fractions up to about 0.08. At higher void fractions (agitated bubbly and churn), the local void fraction profile in the present facility has a good agreement with the measurements of Gerges at the same flow condition with a parabolic shape. The criterion $<a><$ 0.04 is used to distinguish undisturbed bubbly from agitated bubbly flow in the present research.

In Figure 4.11, the radial local void fraction distributions are compared with results from smaller diameter pipes. In the present facility, the local void fraction profiles have the same characteristics as the bubble frequency profile (Figure 4.7). Both the undisturbed bubbly flow in the larger diameter pipe and the bubbly flow in the smaller diameter pipe have an increase close to the wall while the agitated bubbly flow and churn flow have parabolic profiles. This is consistent with the bubble frequency and diameter distributions since the local void fraction is a function of the two distributions.

4.2.4   Bubble Velocity

There is no significant effect of either the flow pattern or pipe diameter on the shape of the radial bubble velocity profiles (Figures 4.12 and 4.13). In all cases, the bubble velocity reduces from a maximum at the pipe centreline towards the wall. In vertical-upward flow, the bubbles typically move faster than the surrounding liquid due to buoyancy. The bubble velocity is increased with either an increase in gas flow rate (Figure 4.13) or liquid flow rate (Figure 4.12). In the present facility, the bubble velocity

increases by about 0.5m/s as j_{water} increases from 0.25 to 0.45m/s at constant j_{air}=0.02m/s

(Figure 4.12) and 2.2m/s as j_{air} increases from 0.02 to 0.24m/s at constant j_{water}=0.35m/s

(Figure 4.13). Compared with the present measurements, the lower bubble velocity was

observed in Gerges' experiment, which is due to the different phase discrimination

methods, as introduced in section 3.4.1, applied during the data processing.

4.3   *Distributions of Bubble Characteristics*

To obtain an overall distribution of the bubble characteristics over the cross

section of the pipe, the probability density function (*PDF*) and cumulative distribution

function (*CDF*) of the bubble chord, local void fraction and bubble velocity are presented

in Figures 4.14 - 4.22.

4.3.1   Bubble Chord

The term bubble chord used here is the path length of the gas bubble or gas

voidage as it passes through the probe. The *PDF* of the bubble chord measured under the

different flow conditions are plotted in Figures 4.14–4.16 (a) with the corresponding

CDF plotted in Figures 4.14-4.16 (b). The gas voidage with measured chord length

larger than 40mm are not shown in the figures for clarity because they represent less than

2% of the total population. No less than 98% of the bubbles in undisturbed bubbly flow

have chord length less than 15mm. No obvious differences in the *PDF* is observed for

measured bubble chord in the range 2mm to 15mm as the air flow rate is increased and

the flow pattern develops from undisturbed bubbly to agitated bubbly and churn flow in

all three series of experiments. However, as the air flow rate increases, the *PDF* of the

smaller bubble chords (≤ 3mm) decrease while it increases for longer bubble chords (≥ 5mm) as more larger bubbles are generated from coalescence of smaller bubbles. In the transition and churn flow, although there is an increase in the number of larger bubbles due to coalescence, there is a corresponding increase in the number of smaller bubbles as well with increasing air flow rate. While coalescence force is dominant for bubbly flow, the break-up forces become as important as the coalescence forces in transition and churn flow.

4.3.2   Local Void Fraction

The *PDF* and *CDF* of local void fractions are shown in Figures 4.17 − 4.19 for different j_{air} at a constant j_{water} of 0.25, 0.35 and 0.45m/s. The local void fraction for the undisturbed bubbly flow does not exceed 0.1, while for agitated bubbly flow, it is less than 0.5. The *PDF(α)* for churn flow has a wider range than bubbly flow and extends close to 1.0 where the distorted large gas voids can have length larger than 20cm. As j_{air} increases, the peak of the *PDF* profiles decreases and the range increase. A double-peak in the *PDF* profile, which is typical in slug flows, indicating the local void fraction in the liquid slug and the Taylor bubbles is not seen in the present distributions as the flow pattern develops from bubbly to churn flow.

For any local void fraction, the *CDF* decreases as j_{air} increases. For example, the *CDF* decreases from 0.97 for bubbly flow (j_{air}=0.02m/s, j_{water}=0.25m/s), to 0.57 for churn flow (j_{air}=0.24m/s, j_{water}=0.25m/s) at void fraction of 0.20. The transition flow regimes of these three series have a *CDF(α=0.20)* close to 0.75, while bubbly flow has a *CDF* (α=0.20)>0.80 and churn flow *CDF(α=0.20)*<0.70.

4.3.3   Bubble Velocity

The *PDF* and *CDF* of upward moving bubble velocity are shown in Figures 4.20 –4.22. The number of higher velocity (u_b>1.5m/s) bubbles increase and the lower velocity (0.4m/s<u_b<1m/s) bubbles decrease as the air flow rate increases. There is an increase in the number of very low velocity (u_b<0.4m/s) bubbles as the air flow rate increases. This is likely due to an increase in the number of bubble collisions with a resultant decrease in the velocity of some bubbles.

From the *CDF*, it can be seen that 50 percent of the bubbles in undisturbed bubbly flow have velocity less than 1m/s, while 90 percent of the bubbles have velocity less than 2.5m/s. In the case of churn flow, 50 percent of the bubbles have velocity less than 1.5m/s and 90 percent of the bubbles have velocity less than 4.0m/s.

4.4   Radial Distribution of Bubble Characteristics

The radial distribution of the bubble frequency, bubble diameter, void fraction and upward bubble velocity are presented in this section. The parameters, in general, increase at any radial position as the air flow rate is increased at a constant water flow rate.

4.4.1   Bubble Frequency

The bubble frequency, or bubble density is defined here as the number of bubbles that pass through the measurement location per unit time. The radial distribution of bubble frequency for the three constant water flow rates with increasing air flow rates are shown in Figures 4.23 - 4.25. At a constant j_{water}, the bubble frequency at any radial

position increases as the j_{air} is increased. For undisturbed bubbly flow B1 (j_{air}=0.02m/s, j_{water}=0.35m/s) and C1 (j_{air}=0.02m/s, j_{water}=0.45m/s), the profiles are almost uniform with a frequency around 5 (1/s). A very small increase in the bubble frequency is discernible close to the wall. In this flow regime, there are few bubble collisions or coalescences and they retain their shape and frequency at which they are generated by the bubble generator. As the air flow rate increases and the flow transitions into agitated bubbly and churn flow, the profiles become parabolic with the value in the core region increasing with air flow rate. The increase in the bubble frequency is greater in the pipe core than closer to the wall, indicating a drift of the bubbles from the wall region to the central region. For example, at the pipe centreline of experiment series B (Figure 4.24), the frequency increases from 39 (1/s) to 65 (1/s) as the flow transitions from agitated bubbly to churn flow, while it remains nearly constant at 10 (1/s) close to the pipe wall (r/R = 0.975).

The bubble frequencies at selected radial positions (r/R= 0, 0.5, 0.75 and 0.975) are plotted as a function of j_{air}/j_{water} in Figure 4.26. Close to the wall (r/R= 0.975), the bubble frequency is almost constant for all three j_{water} . As the distance from the wall increases, the frequency increases with j_{air}/j_{water}. There is also a corresponding increase in the bubble frequency with j_{water} at a fixed j_{air}/j_{water}.

4.4.2   Bubble Diameter

The radial distribution of the bubble diameter for both undisturbed and agitated bubbly flow is relatively flat, though there is a small increase in the diameter in the central region in the agitated bubbly flow (Figures 4.27 – 4.29). In the transition and churn flow regimes, the profiles become distinctly parabolic. In the central region, the

bubble diameter increases as the air flow rate increases.   For example, for the experimental series B (Figure 4.28), the average bubble diameter or length of gas voidage at the centreline ($r/R = 0$) increases from 8.0mm to 12.3mm as the flow transitions from agitated bubbly to churn flow. The bubble diameter near the pipe wall remains constant at around 6mm for agitated bubbly and churn flow patterns. The profile for undisturbed bubbly flow, however, is almost uniform with a bubble diameter about 4mm. There is a slightly higher scatter in the bubble diameter profiles because only the successful bubble hits that yield the diameter are considered, which results in a smaller bubble diameter population.

The bubble diameters at selected radial positions are plotted as a function of j_{air}/j_{water} in Figure 4.30 at different radial positions ($r/R= 0$, 0.5, 0.75 and 0.975). In the near-wall region ($r/R= 0.975$), the bubble diameter is almost constant beyond $j_{air}/j_{water} \geq$ 0.2 and does not change with j_{air} or j_{water}. At the other radial locations, there is an increase in the bubble diameter with j_{air}/j_{water}, with the increase being more pronounced towards the centreline. For a given j_{air}/j_{water}, there is an increase in the bubble diameter as j_{water} increases from 0.25m/s to 0.35m/s, but with a further increase in j_{water} there is no increase in the bubble diameter for the agitated bubbly and churn flow. It can be speculated that the increase in turbulence levels with an increase in j_{air} increases the break-up forces and limits the bubble size in this case.

4.4.3   Local Void Fraction

The local void fraction distributions are presented in Figures 4.31 – 4.33. For very low void fractions ($<\alpha> < 0.04$), the profile is almost flat with a small increase as the wall is approached. This is consistent with the observation of Stankovic [11]. As the

air flow rate is increased, the local void fraction increases in the central region and the profiles become more parabolic. The local void fractions of undisturbed bubbly flow is significantly less than the other flow patterns. Close to the wall (r/R=0.975), the local void fraction increases from about 0.02 for undisturbed bubbly flow to about 0.05 for agitated bubbly flow (Figure 4.34). It does not increase further with either an increase in j_{air} or j_{water}. Away from the wall, the void fraction increases with j_{air}/j_{water} and is consistent with the bubble frequency. The local void fraction at the pipe centreline is above 0.2 when the flow transitions from bubbly to churn flow.

4.4.4   Bubble Velocity

The bubble velocity distributions are shown in Figures 4.35 – 4.37. Except for the undisturbed bubbly flow, the bubble velocities are highest in the core-region and decrease as the wall is approached. In the undisturbed bubbly flow, the bubbles have a uniform velocity across the cross section. The bubble velocities under the different flow conditions are compared at four radial positions, r/R= 0, 0.5, 0.75 and 0.975, in Figure 4.38. For all radial positions, the bubble velocities increase as j_{air}/j_{water} or j_{water} increases.

4.5 Interfacial Area Concentration

The interfacial area concentration is defined as the available interfacial area per unit volume of a mixture, and represents the average order geometrical effect of the interfacial structure. As a first approximation, the *IAC* of bubbly and churn flows in the current experiments are calculated using Equations (2-37) - (2-42). The results for the *IAC* across the flow area for the flow conditions listed in Table 4.1 are given in Table 4.2.

Table 4.2   *IAC* (m^{-1}) of different flow conditions

j_{air} (m/s) \\ j_{water} (m/s)	0.02	0.10	0.12	0.14	0.16	0.20	0.24
0.25	49	107	113	115	115	123	135
0.35	18	114	98	103	110	109	121
0.45	23	122	119	102	104	112	131

The *IAC* at a fixed j_{water} increases as j_{air} is increased for each flow pattern. For example, at j_{water}=0.35m/s, the *IAC* of undisturbed bubbly flow (j_{air}=0.02m/s) is 18(m^{-1}) and increases up to 121(m^{-1}) for churn flow (j_{air}=0.24m/s). The *IAC* of undisturbed bubbly flow is lower than that of agitated bubbly flow. Nevertheless, no distinct differences of *IAC* were found between agitated bubbly and churn flows.

The radial distribution of the local *IAC* is shown in Figures 4.39 - 4.41. The *IAC* radial distribution profiles are similar to that of the local void fraction profiles (Figures 4.31   4.33) with a parabolic shape for agitated bubbly and churn flow pattern, a relatively flat profile in undisturbed bubbly flow. The *IAC* of transition and churn flow do not change significantly as the air flow rate increases. For example, the *IAC* increases from 120(m^{-1}) to 142(m^{-1}) at pipe centerline when the flow goes from transition to churn at j_{water}=0.35m/s (Figure 4.40). The *IAC* of agitated bubbly flow decreases slightly with an increase in air flow rate. This is likely due to a higher coalescence with an increase in air flow rate in this flow regime. The *IAC* of undisturbed bubbly flow is significantly less than that of other flow patterns. At a given radial position, there is no discernible change in the *IAC* with j_{air}/j_{water} (Figure 4.42).

The present radial *IAC* distribution of the agitated bubbly flow is compared with those of other experiments performed in small (*D*=0.05m) and larger diameter (*D*=0.20m) pipes by Revankar and Ishii [83] and Gerges [12] in Figure 4.43. The *IAC* profiles in the larger diameter pipe have a parabolic shape, with the *IAC* decreasing as the wall is approached. Due to the higher concentration of bubbles near the wall in smaller diameter pipes, the radial *IAC* profile measured by Revankar and Ishii has a wall-peak shape, similar to the bubble frequency and void fraction profiles.

4.6 Drift Flux Model Correlations

In the design and analysis of two-phase flow systems, the drift-flux model is often used to estimate the void fraction. It has been noted that the drift velocity for a relatively large diameter pipe differs from that for a smaller diameter pipe [50] [52]. The present results are compared with the prediction from drift-flux models of Shoukri et al. [10], Kataoka and Ishii [50] and Hirao [52] for large diameter pipes in Figure 4.44. A drift-flux correlation for bubbly flow based on the measurement from the present facility was proposed by Shoukri et al. as:

$$\frac{j_g}{\alpha} = 0.8j + 0.45 \text{ (Bubbly)} \tag{4-2}$$

For Kataoka and Ishii's model, the dimensionless hydraulic diameter and dimensionless viscous number are calculated as $D_H^* = 73.41$ and $N_{\mu l} = 1.99*10^{-3}$, and the drift–flux correlation is obtained as:

$$\frac{j_g}{\alpha} = 1.194j + 0.478 \tag{4-3}$$

With the same distribution parameter C_0, Hirao's drift-flux correlation is obtained as:

$$\frac{j_g}{\alpha} = 1.194j + 0.728 \tag{4-4}$$

The RMS errors of predicted void fraction by these correlations for different flow patterns are shown in Table 4.3.   Except for the undisturbed flow regime, Hirao's correlation underpredicts the void fraction in the other flow regimes.   The present results are in good agreement with Shoukri et al.'s model from the agitated bubbly to the churn flow regimes.   The Kataoka and Ishii's theoretical model shows a better prediction for churn flow although underprediction at bubbly flow pattern.

**Table 4.3 The RMS percentage error of void fraction
predicted by different drift-flux correlations**

Flow pattern / Correlation	Undisturbed bubbly	Agitated bubbly	Transition	Churn
Shoukri et al.	45	27	7	16
Kataoka and Ishii	18	40	24	11
Hirao	13	52	39	27

The measurements of Gerges and present experiments are compared with the prediction by Shoukri et al.'s drift-flux model in Figure 4.45.   The correlation shows a good agreement with both measurements with underprediction for bubbly flow and overprediction for churn flow.

The j_{air}/α of the current data is plotted against j in Figure 4.46 for the different flow regimes. The data clearly falls into different bands for the different flow regimes, making it unlikely that a single model will be valid in all flow regimes. The local drift velocity v_{gj} of churn flow is almost twice that of agitated bubbly flow, indicating a higher local relative velocity between the two phases in the churn flow.
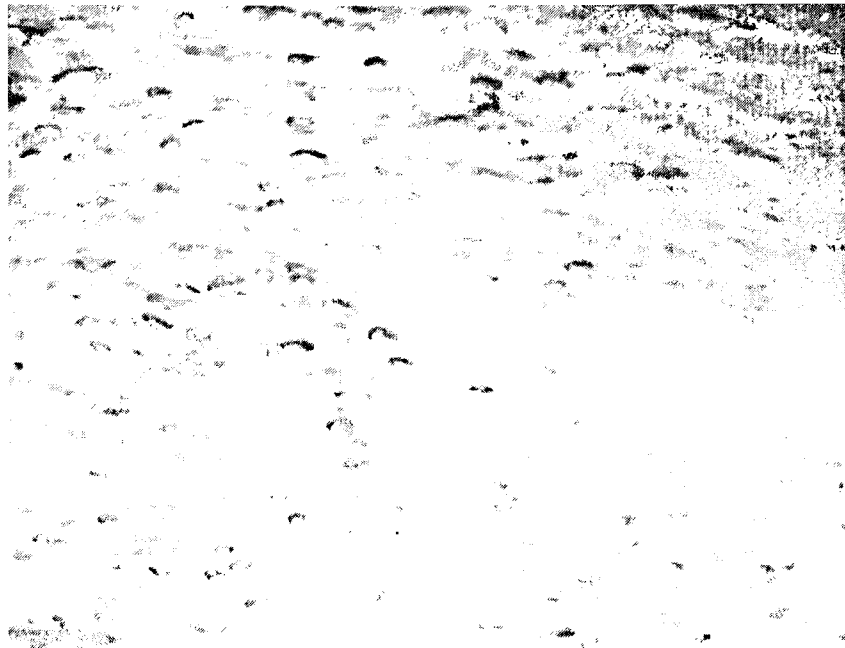
(a) Bubbly Flow
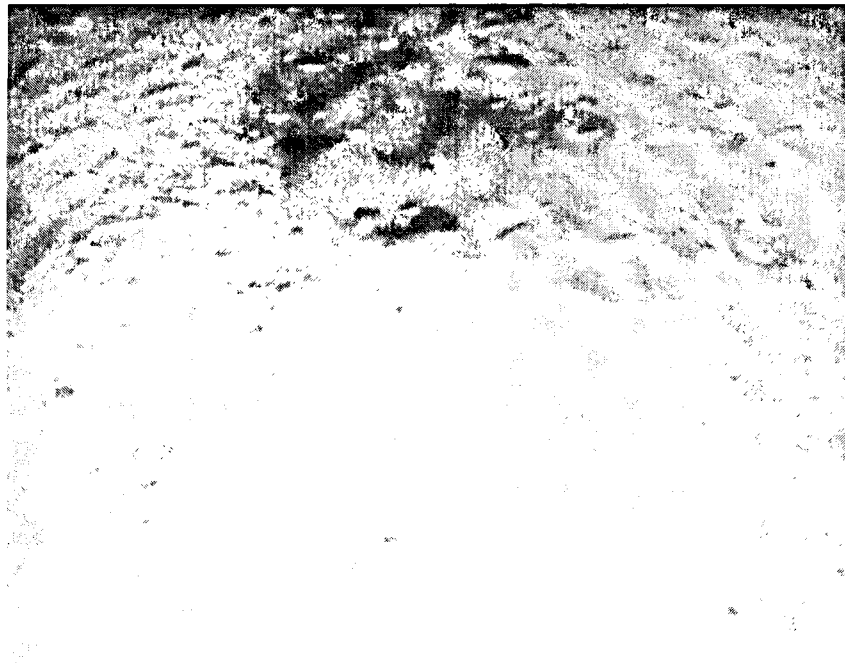
(b) Churn Flow

Figure 4.1 Typical bubbly and churn flow in the present 20cm diameter vertical pipe
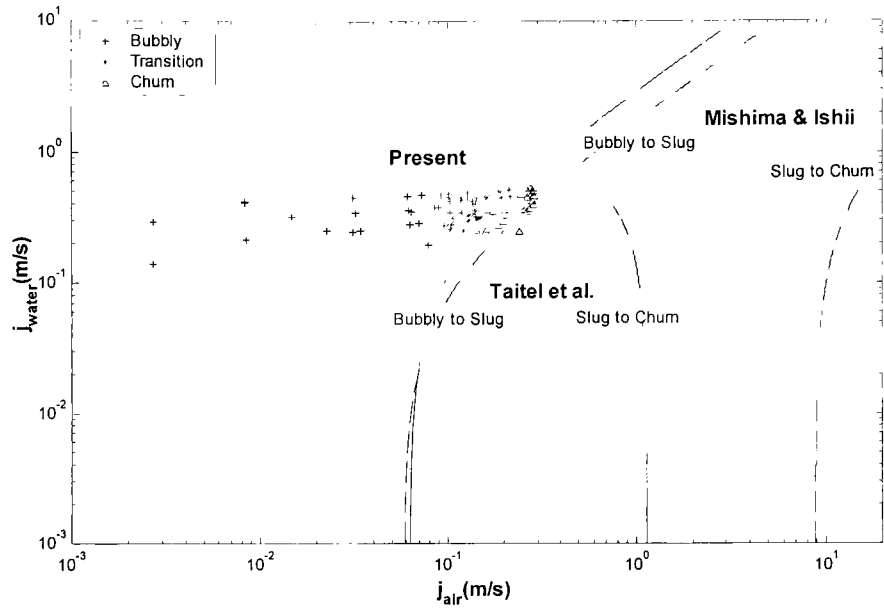
(a)
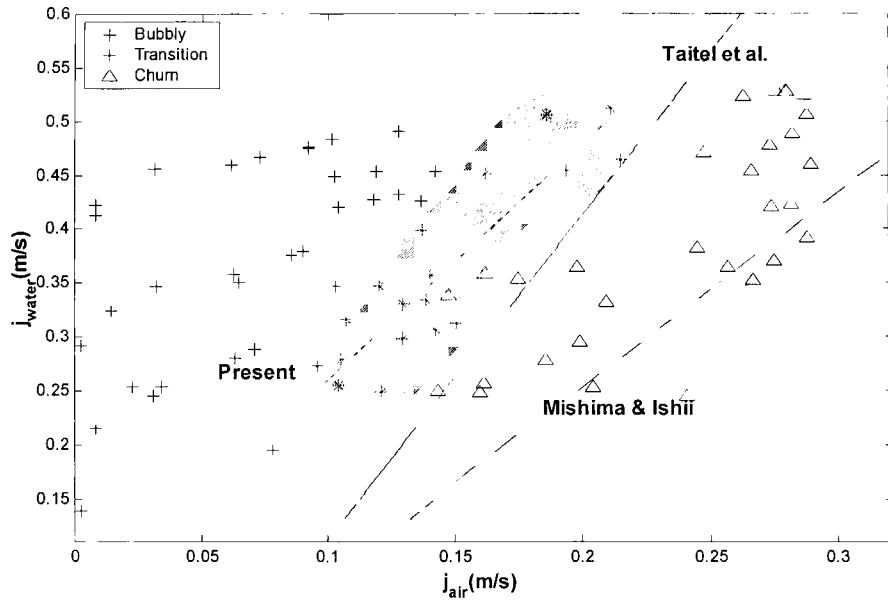
(b)

Figure 4.2   Comparison of current flow map with flow maps of Taitel et al. [9] and Mishima and Ishii [24]
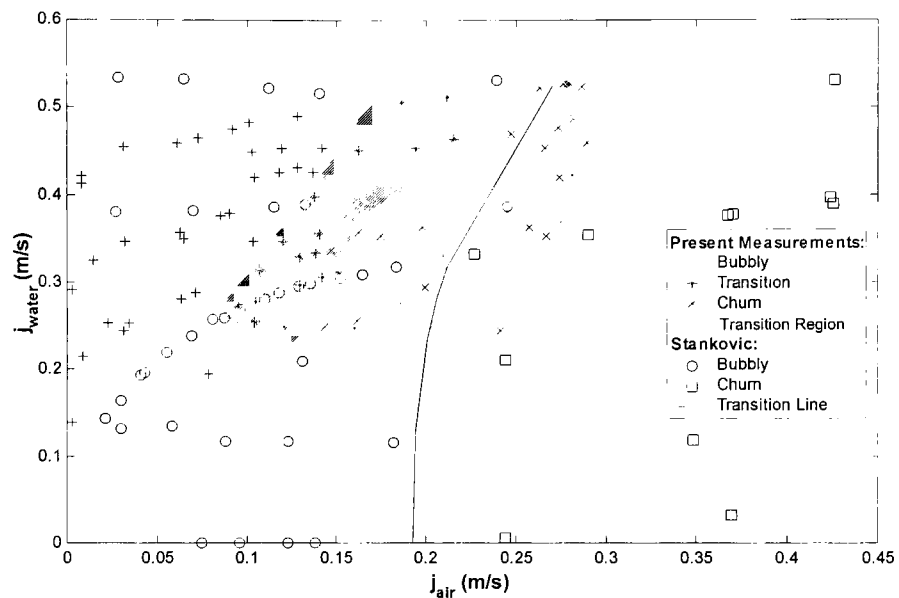
Figure 4.3   Comparison of current flow map with flow map of Stankovic [11]
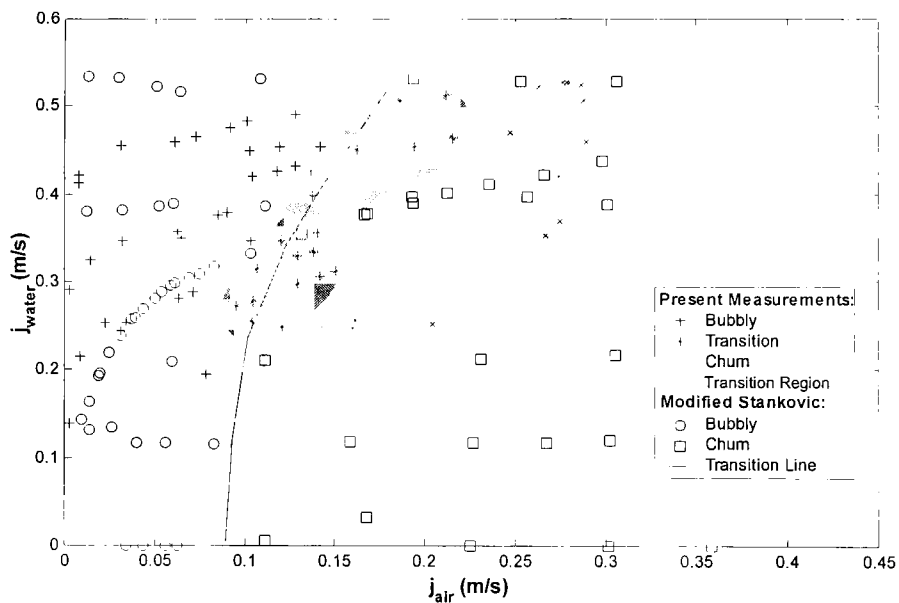
Figure 4.4   Comparison of current flow map with modified flow map of Stankovic [11]
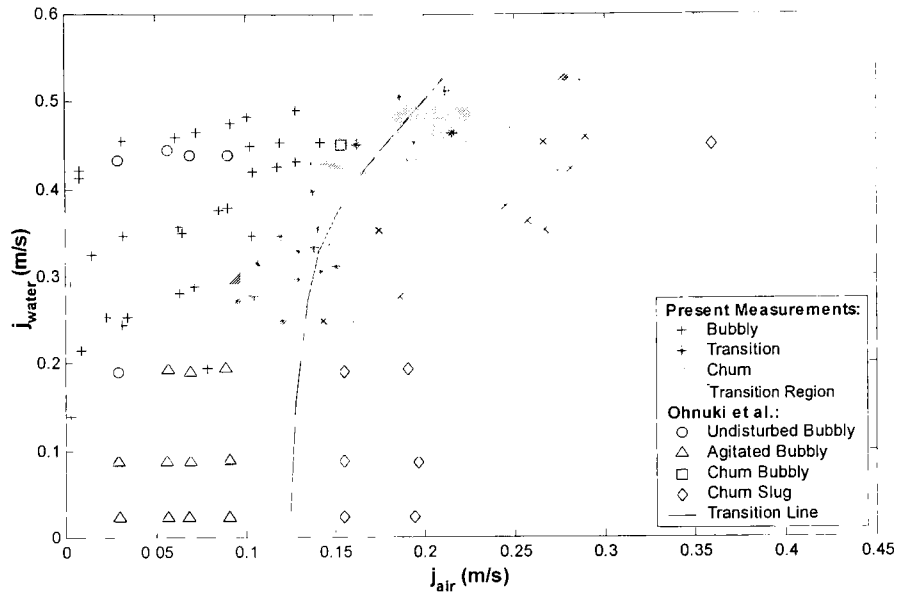
Figure 4.5   Comparison of current flow map with flow map of Ohnuki et al. [14]
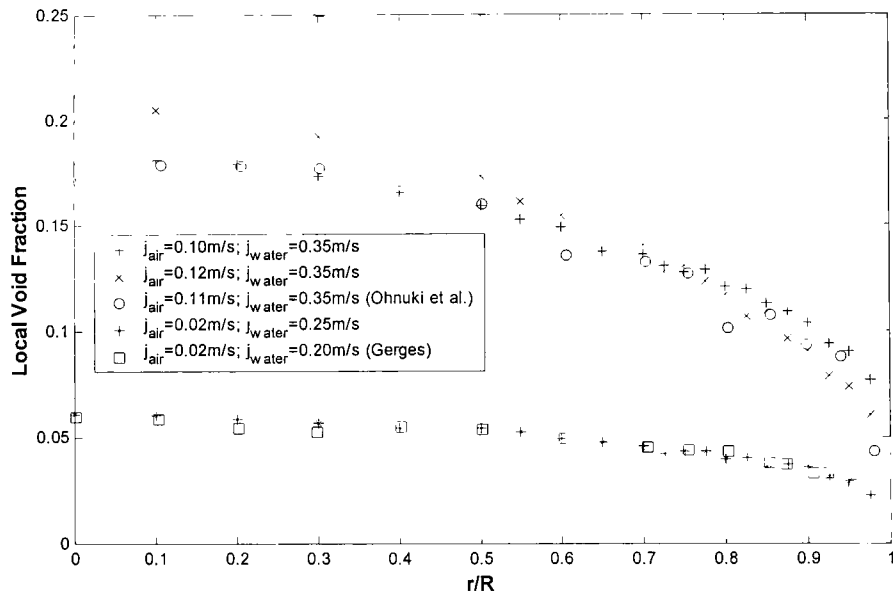
Figure 4.6   Comparison of radial void fraction profiles with results of Stankovic and Ohnuki et al. at approximately same flow conditions
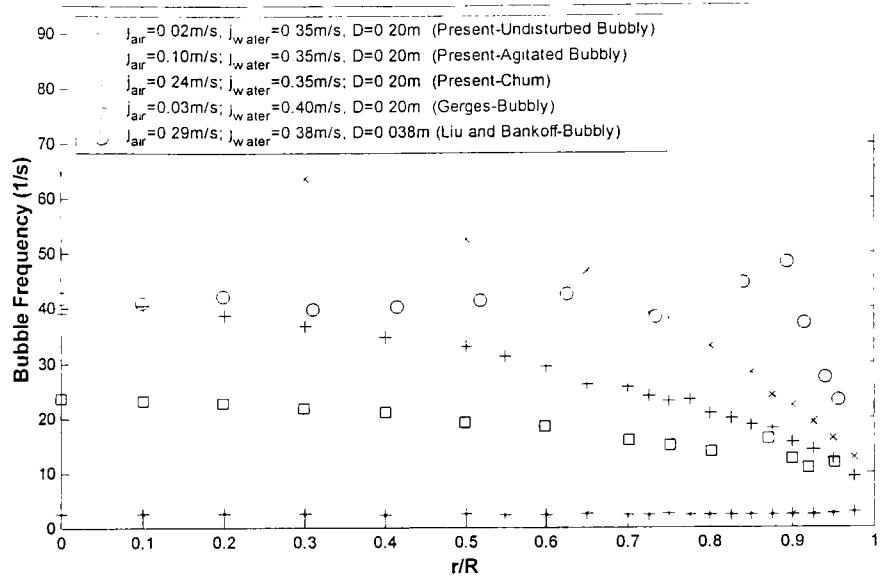
Figure 4.7 **Comparison of radial bubble frequency profiles in large and small diameter pipes**
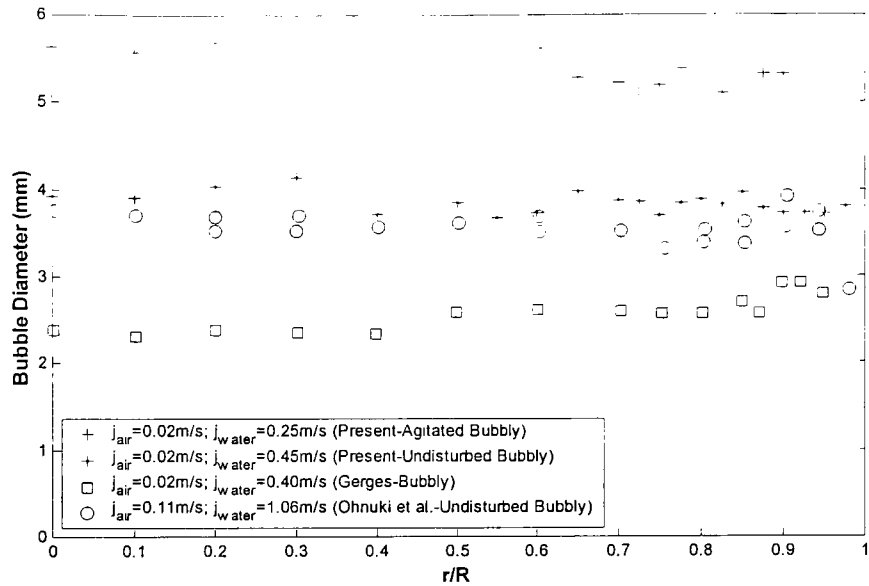
Figure 4.8   ˙ Radial bubble diameter profiles measured in large diameter pipes (*D*=20cm)
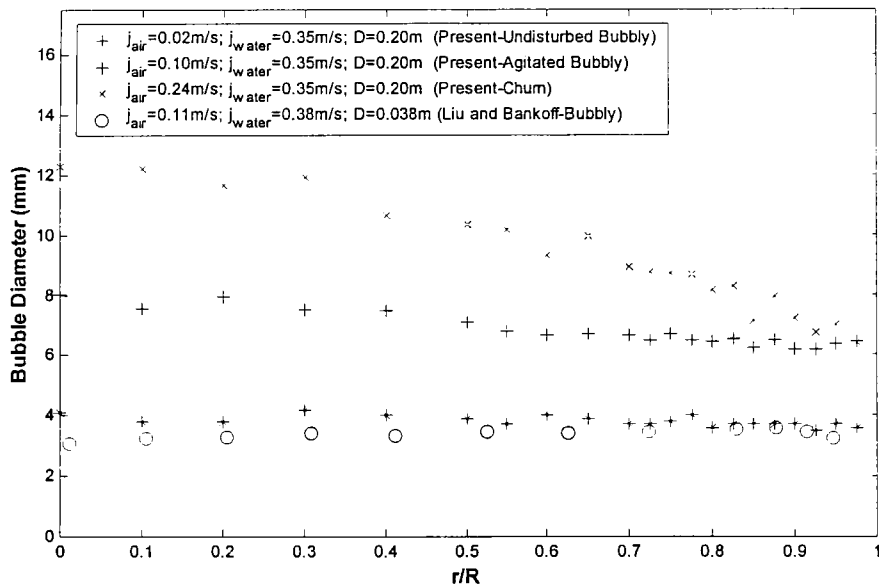
Figure 4.9   Comparison of radial bubble diameter profiles in large and small diameter pipes
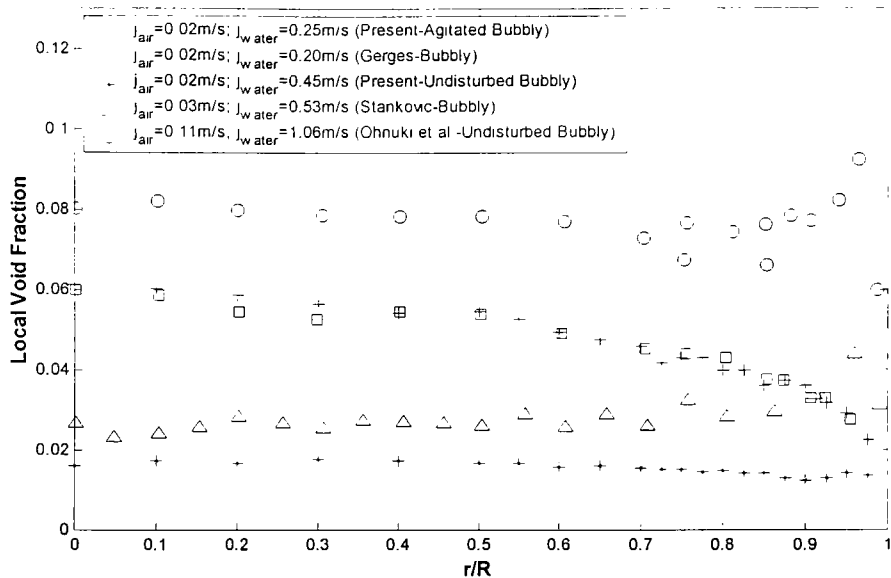
Figure 4.10   Radial local void fraction profiles measured in large diameter pipes (*D*=20cm)
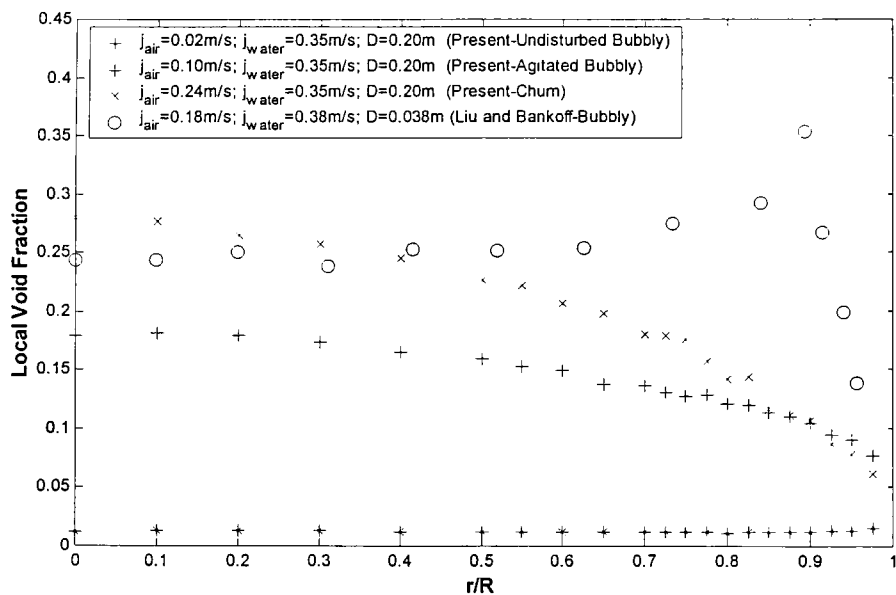
Figure 4.11   Comparison of radial local void fraction profiles in large and small diameter pipes
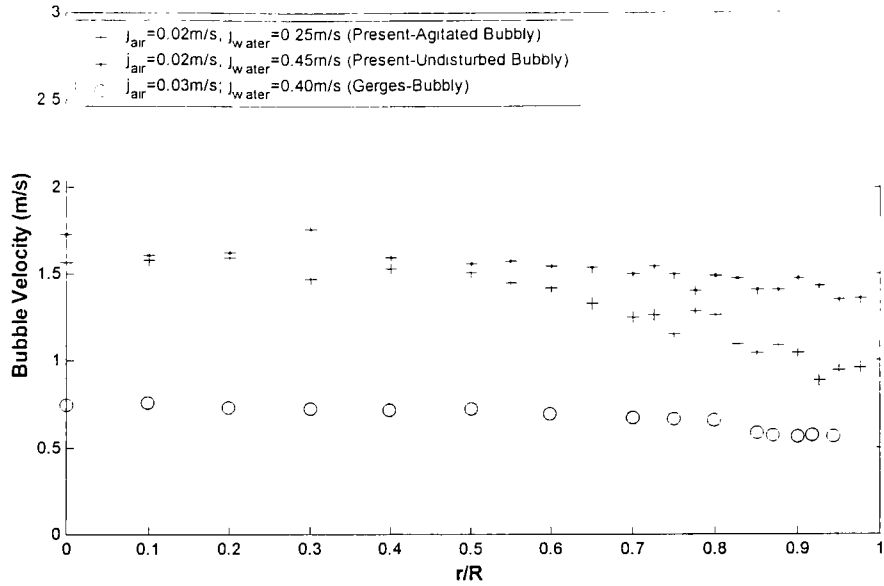
Figure 4.12   Radial bubble velocity profiles in large diameter pipe (*D*=20cm) for bubbly flow
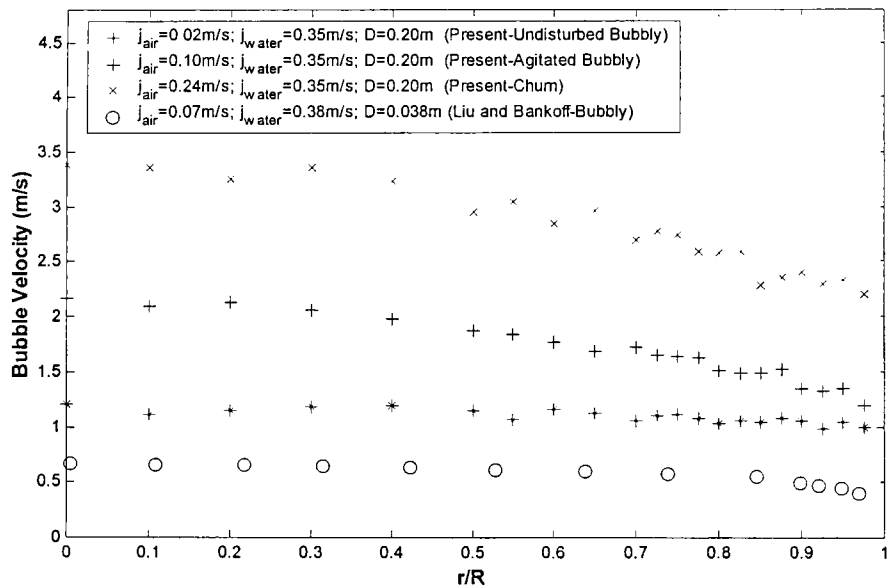
Figure 4.13   Comparison of radial bubble velocity profiles in large and small diameter pipes
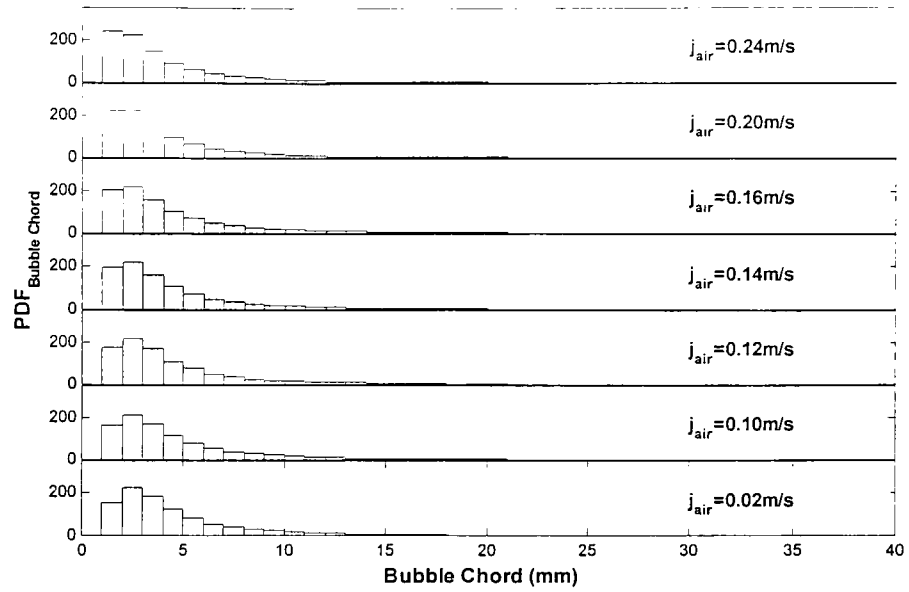
(a)
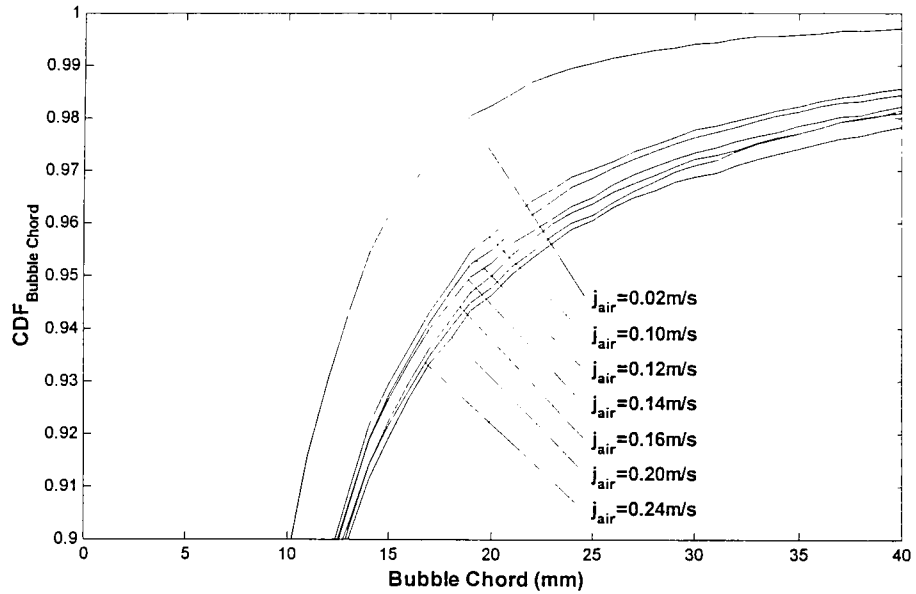
(b)

Figure 4.14   (a) *PDF* (b) *CDF* of bubble chord for j_{water}=0.25m/s
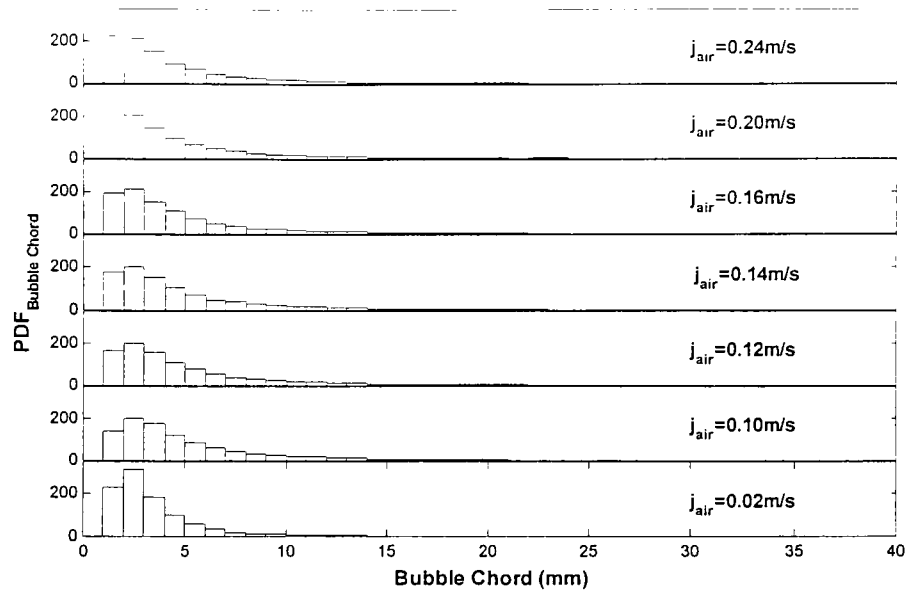
(a)
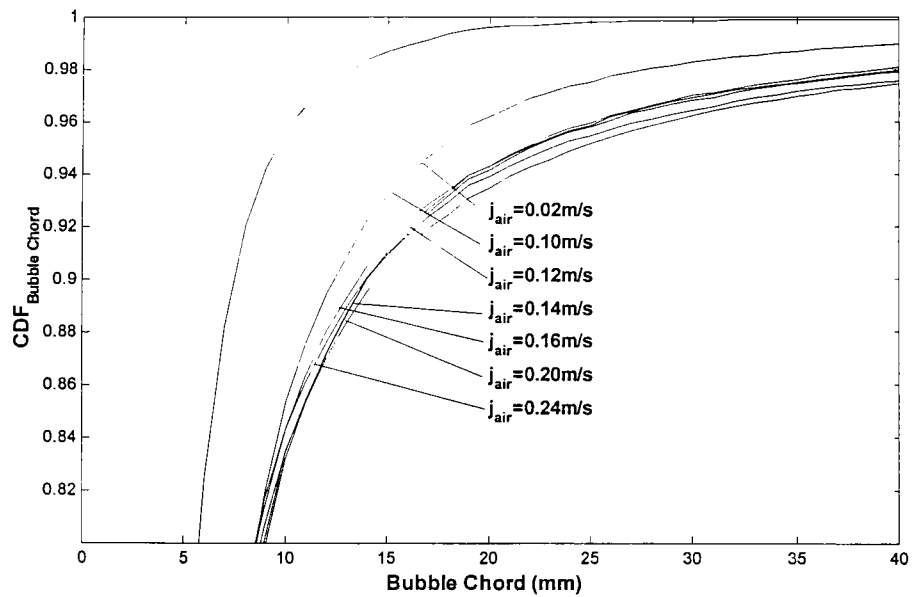
(b)

Figure 4.15 (a) *PDF* (b) *CDF* of bubble chord for j_{water}=0.35m/s
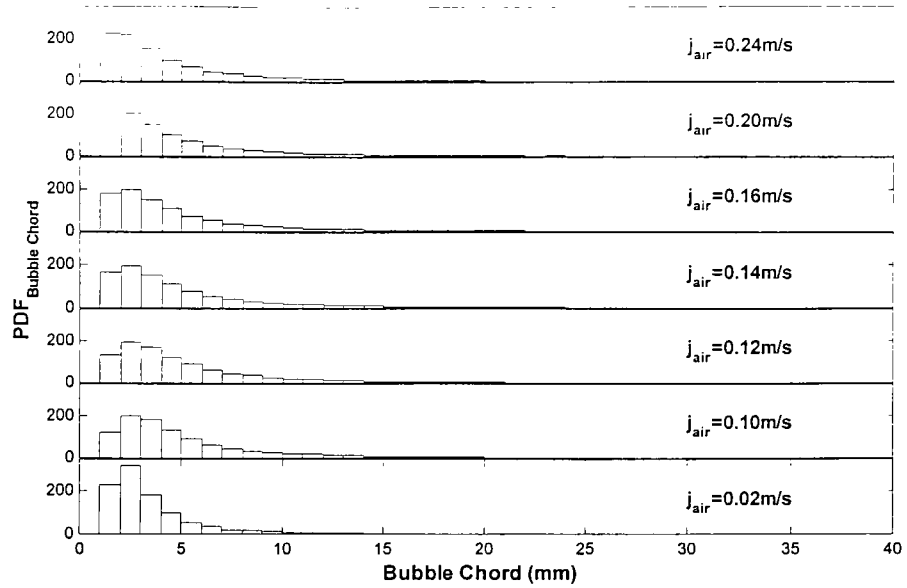
(a)
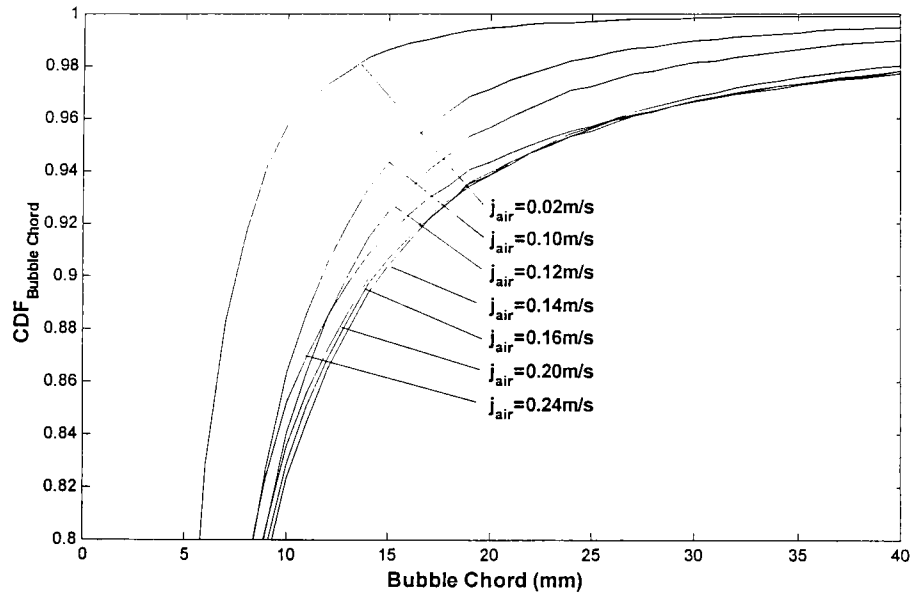
(b)

Figure 4.16   (a) *PDF* (b) *CDF* of bubble chord for j_{water}=0.45m/s
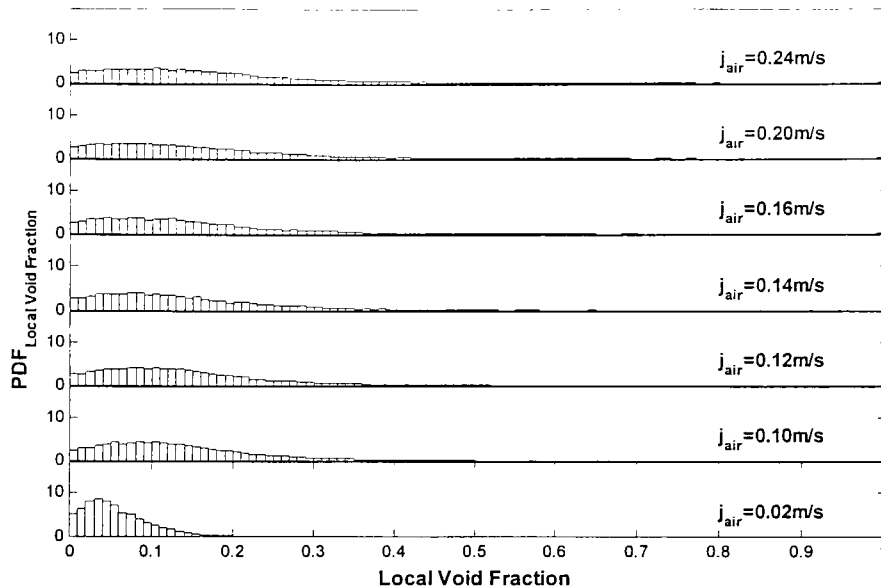
(a)
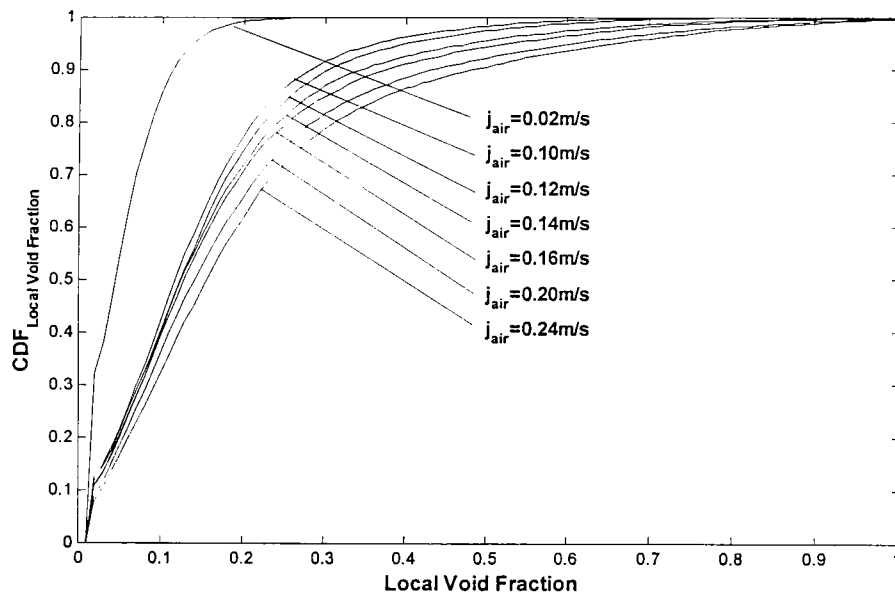
(b)

Figure 4.17   (a) *PDF* (b) *CDF* of local void fraction for j_{water}=0.25m/s
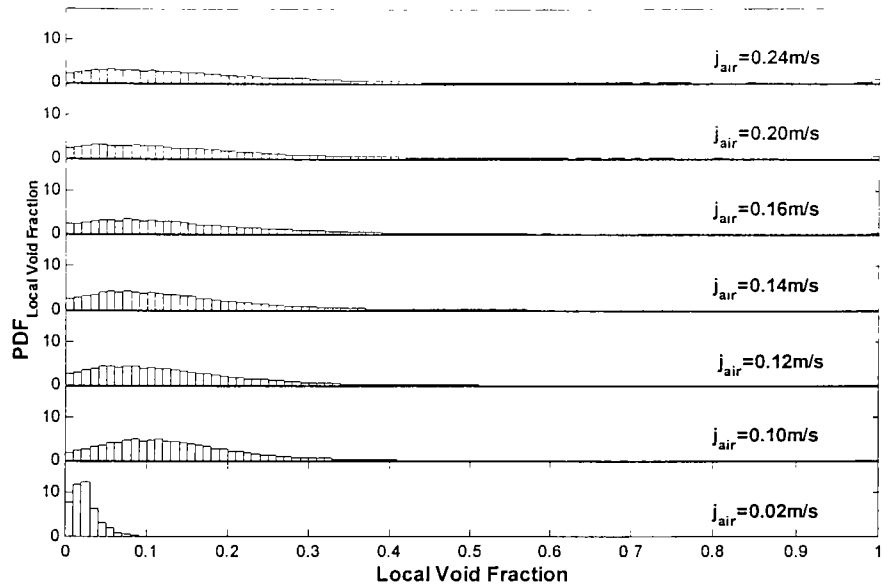
(a)
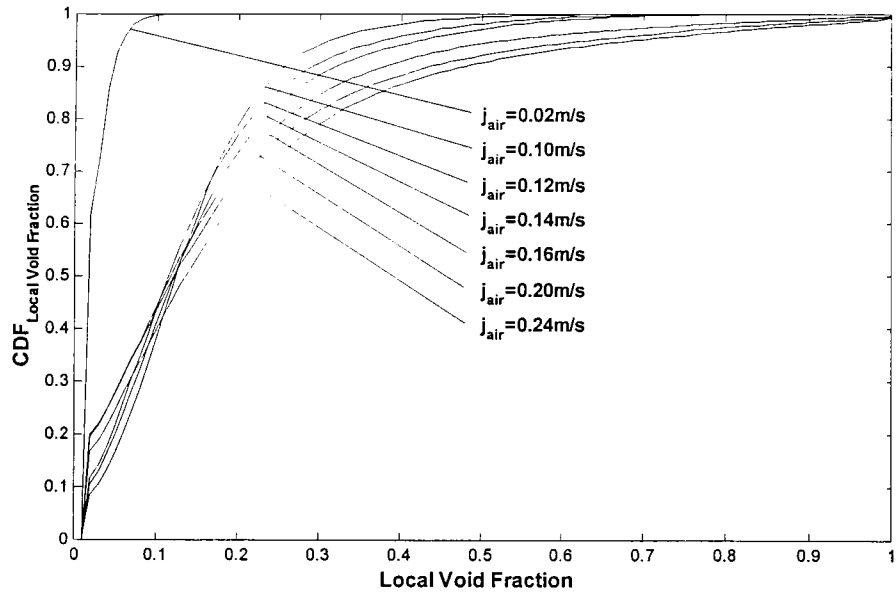
(b)

Figure 4.18   (a) *PDF* (b) *CDF* of local void fraction for *j$_{water}$*=0.35m/s
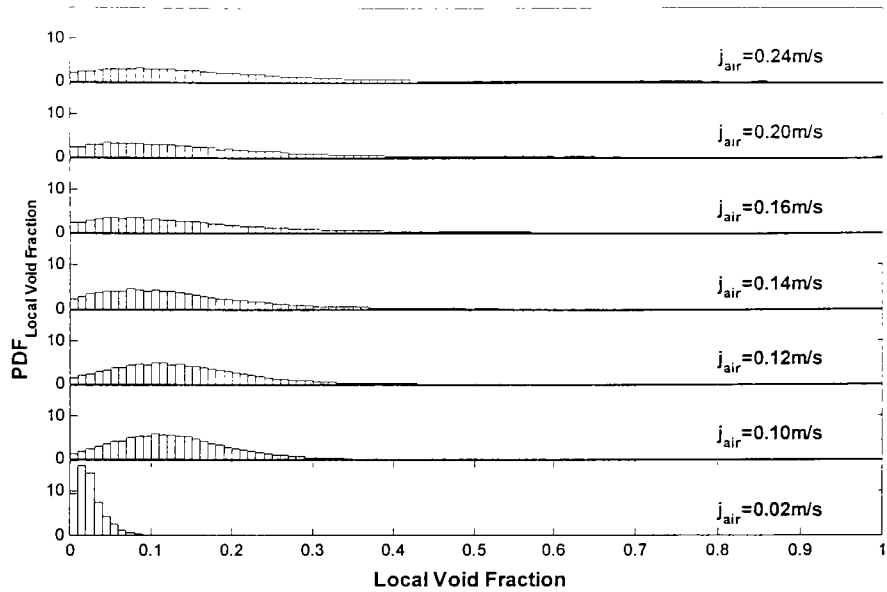
(a)
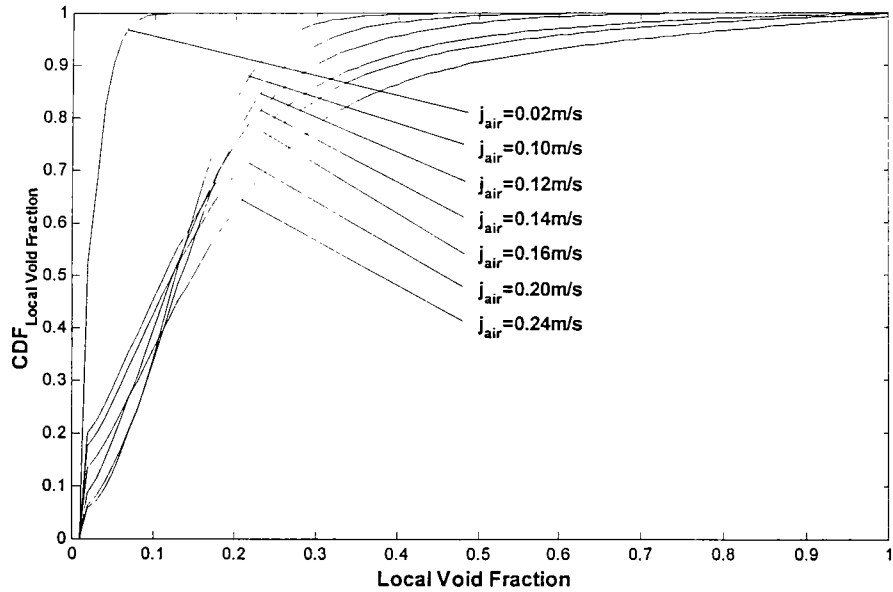
(b)

Figure 4.19   (a) *PDF* (b) *CDF* of local void fraction for j_{water}=0.45m/s
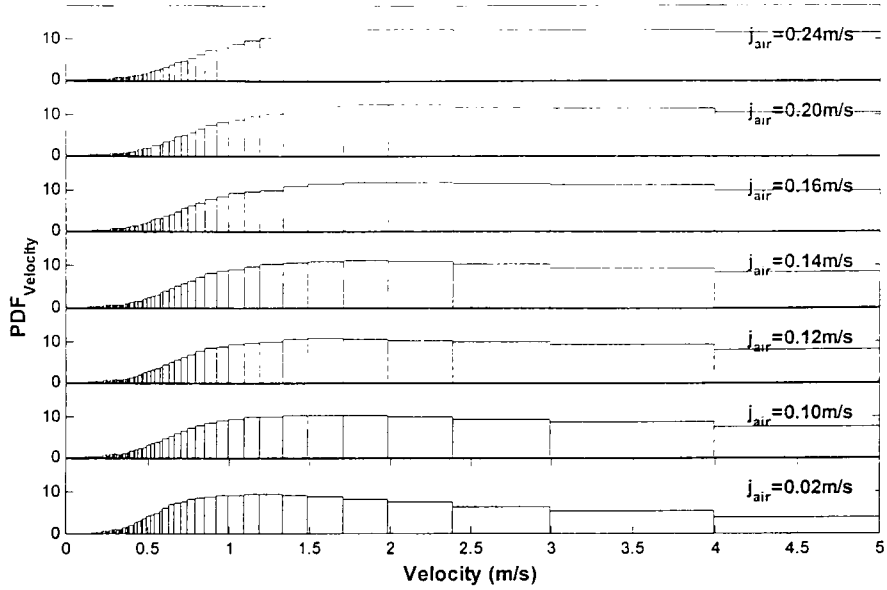
(a)
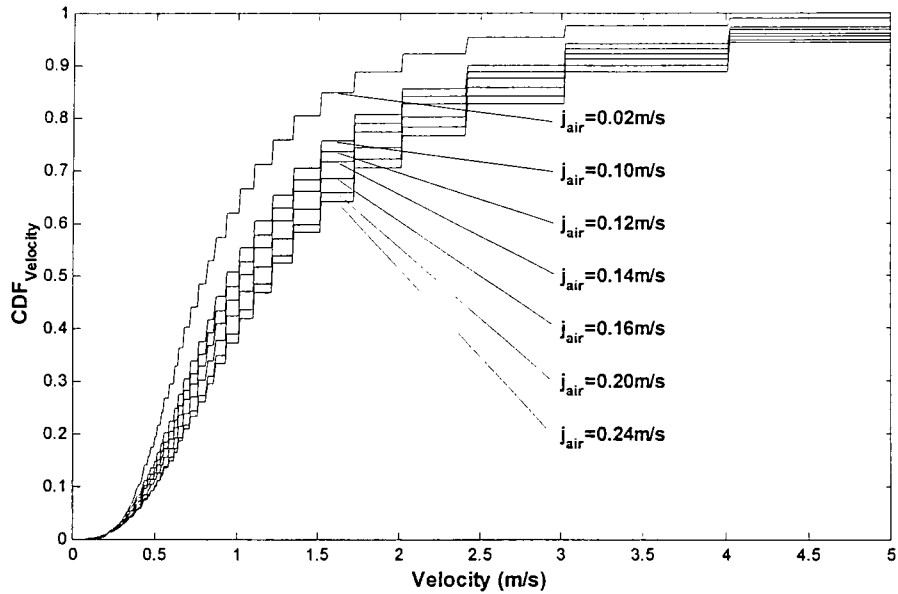
(b)

Figure 4.20   (a) *PDF* (b) *CDF* of bubble velocity for j_{water}=0.25m/s
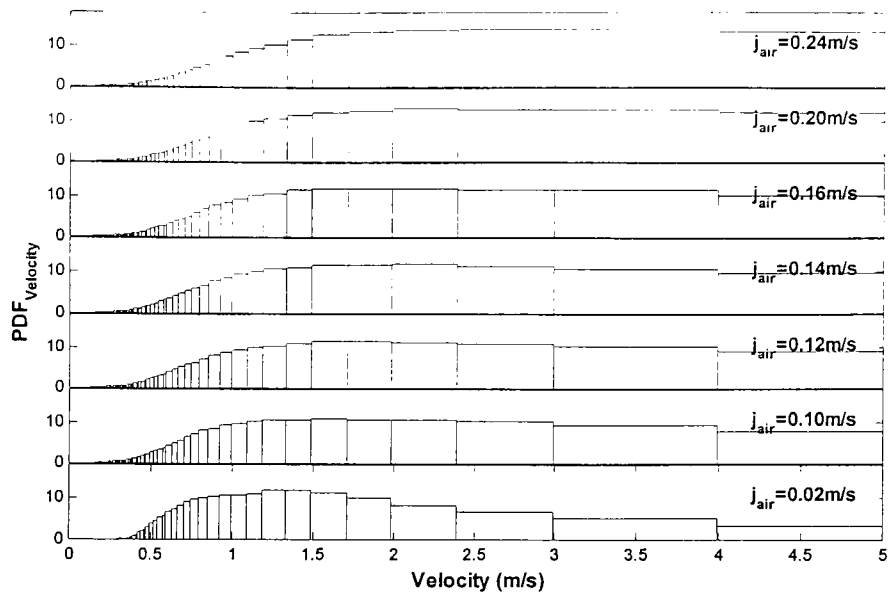
(a)
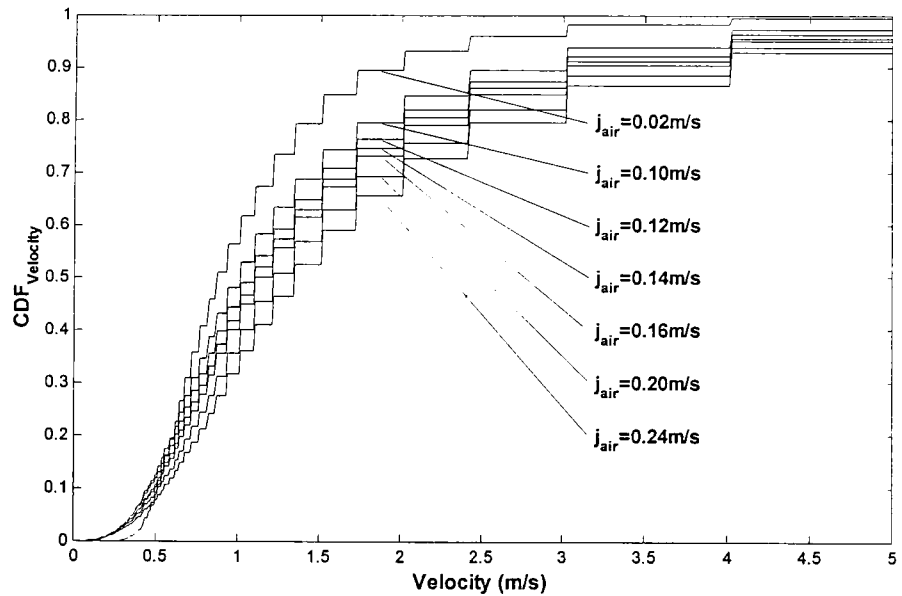
(b)

Figure 4.21   (a) *PDF* **(b)** *CDF* **of bubble velocity for** j_{water}**=0.35m/s**
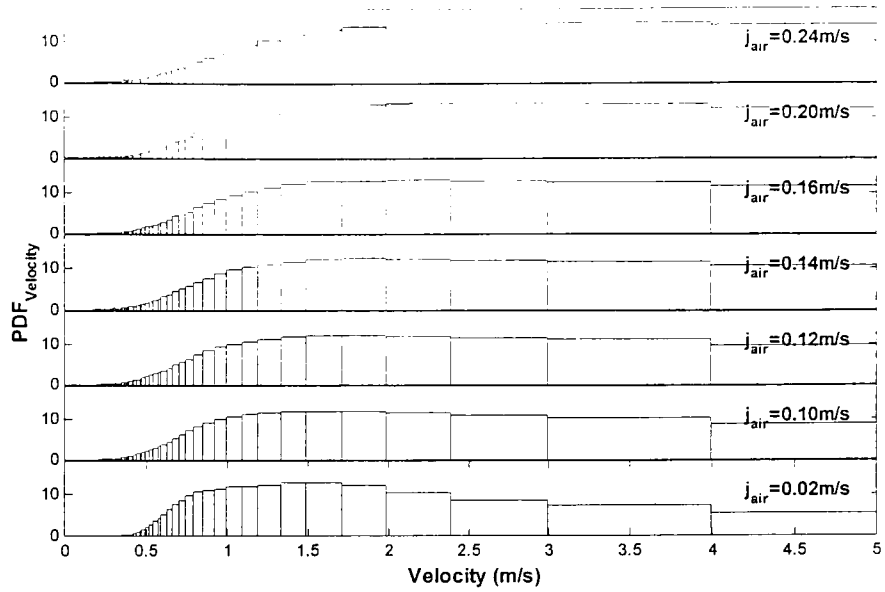
(a)
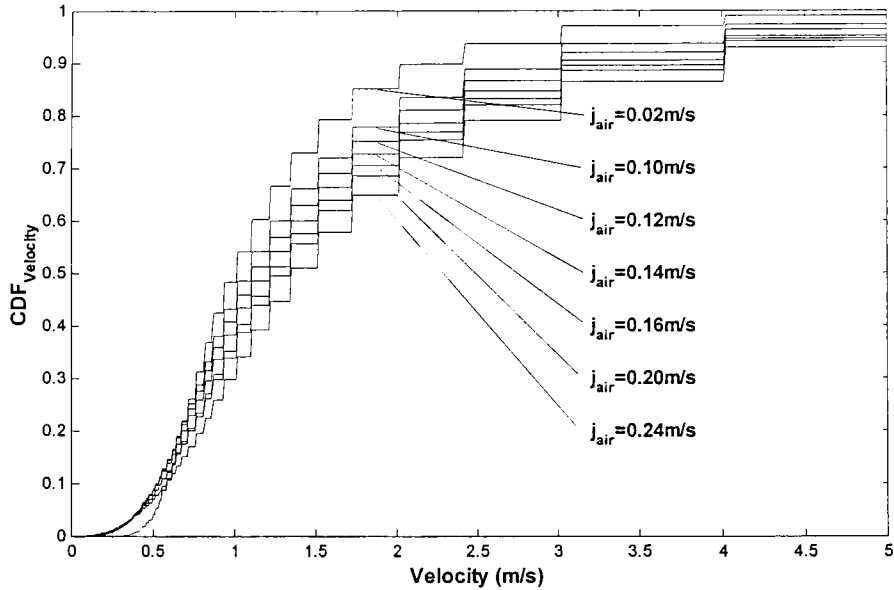
(b)

Figure 4.22   (a) *PDF* (b) *CDF* of bubble velocity for j_{water}=0.45m/s
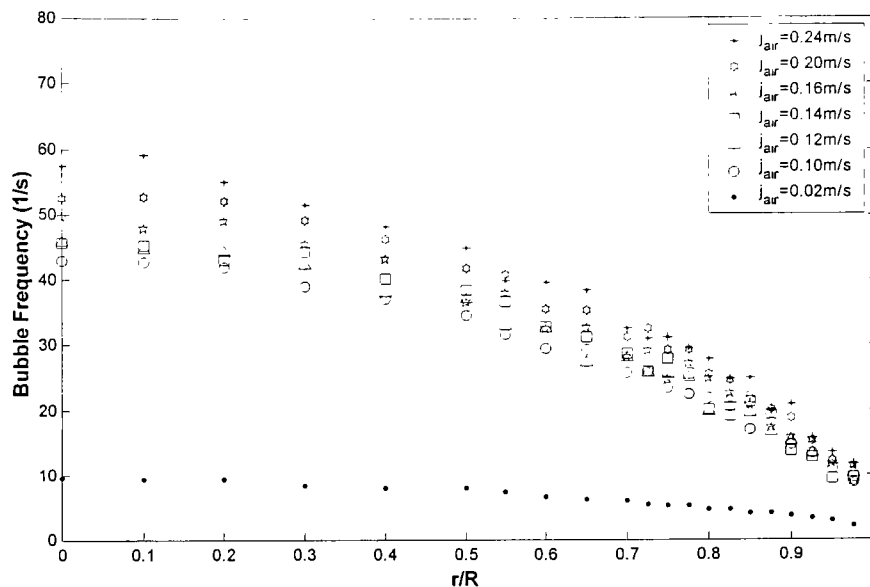
Figure 4.23   Radial bubble frequency distribution for j_{water}=0.25m/s
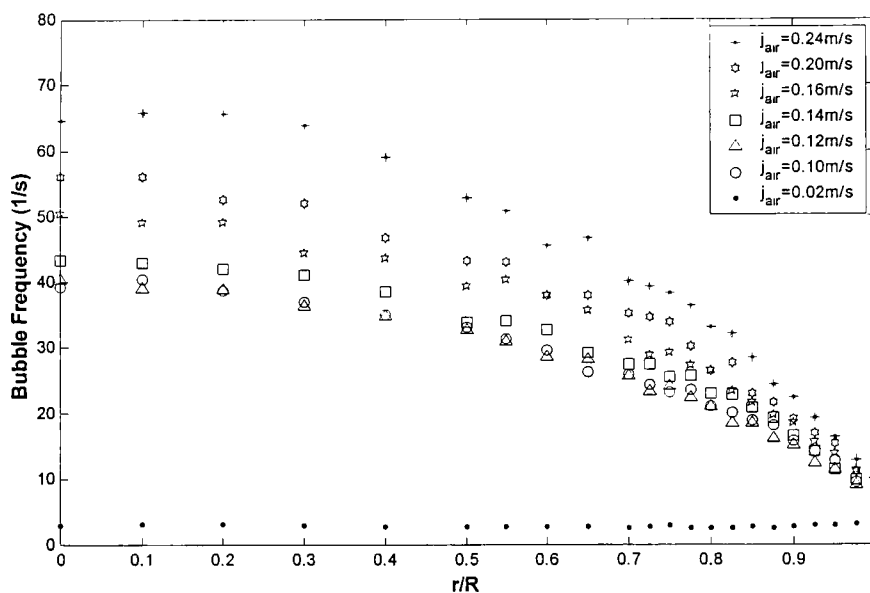
Figure 4.24   Radial bubble frequency distribution for j_{water}=0.35m/s
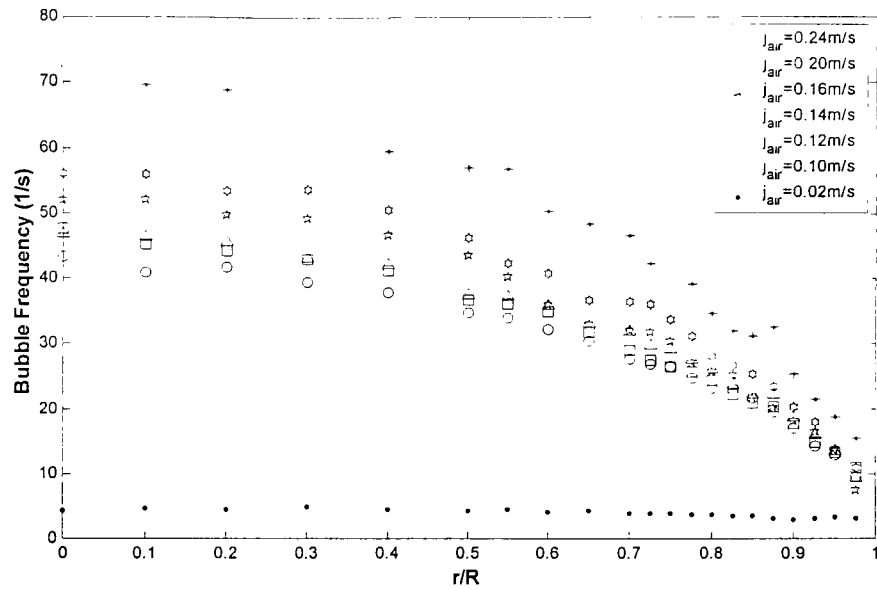
Figure 4.25   Radial bubble frequency distribution for *j*$_{water}$=0.45m/s
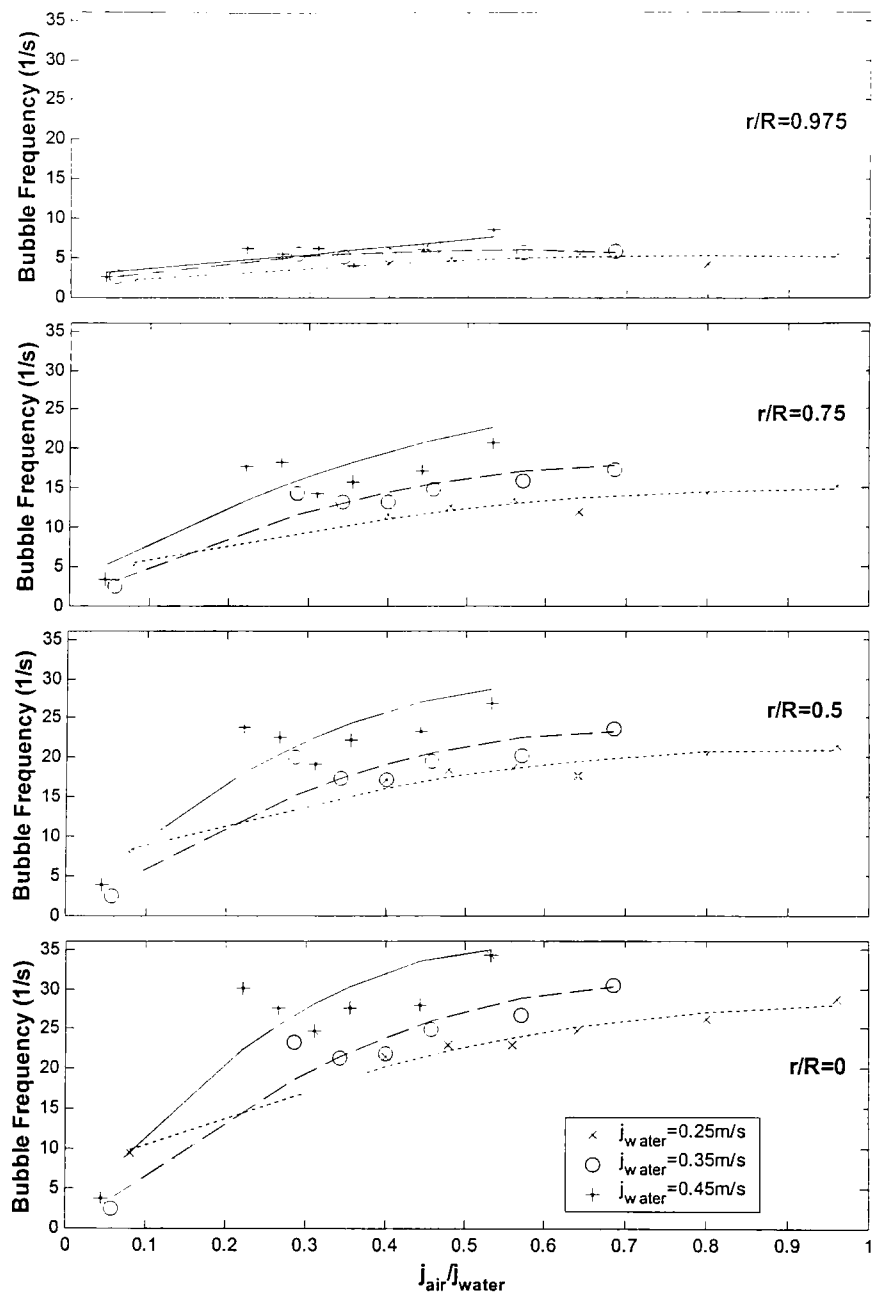
Figure 4.26   Bubble frequency vs. j_{air}/j_{water}
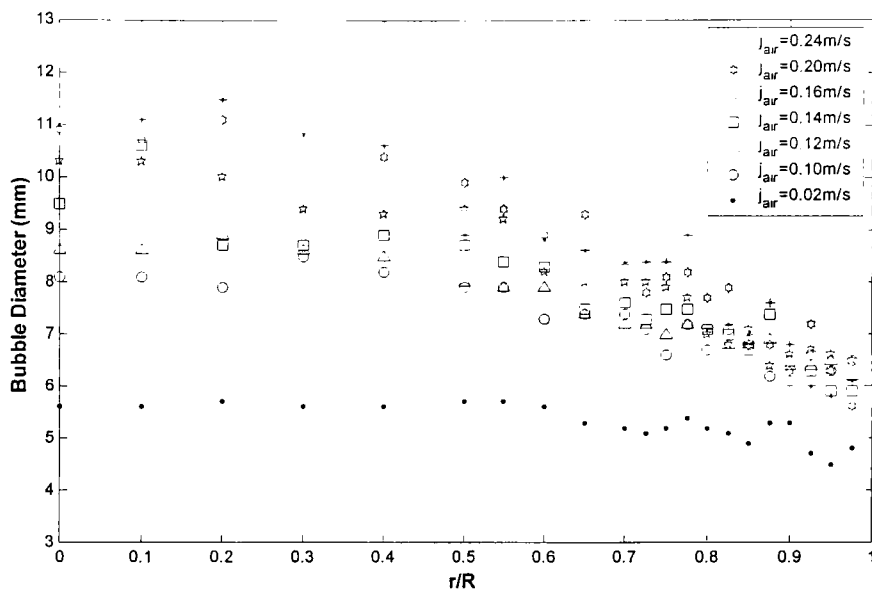
Figure 4.27   Radial bubble diameter distribution for j_{water}=0.25m/s
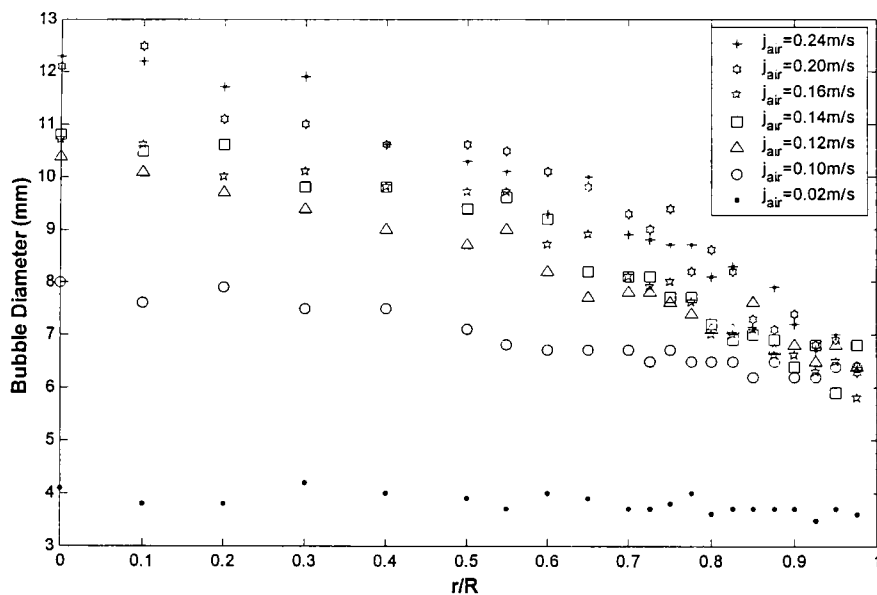
Figure 4.28   Radial bubble diameter distribution for j_{water}=0.35m/s
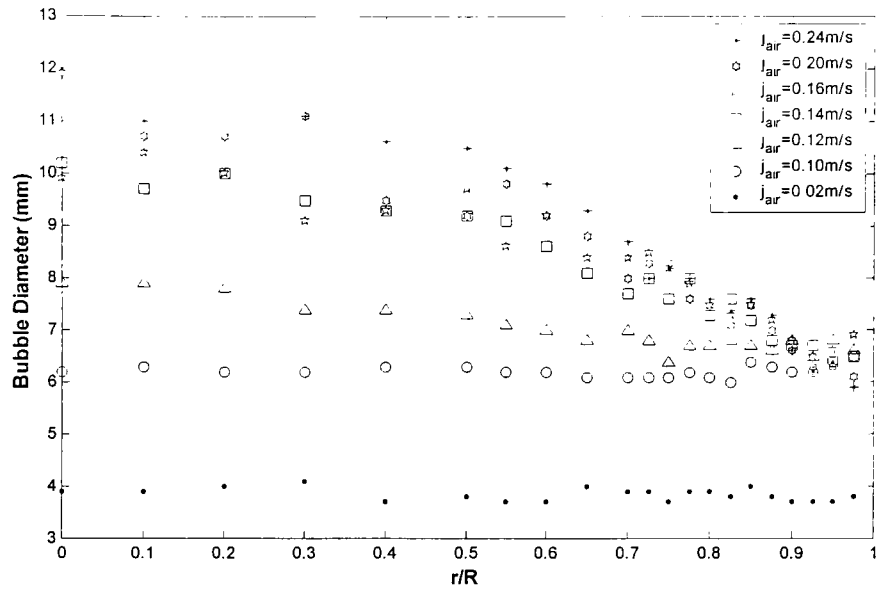
Figure 4.29   Radial bubble diameter distribution for j_{water}=0.45m/s
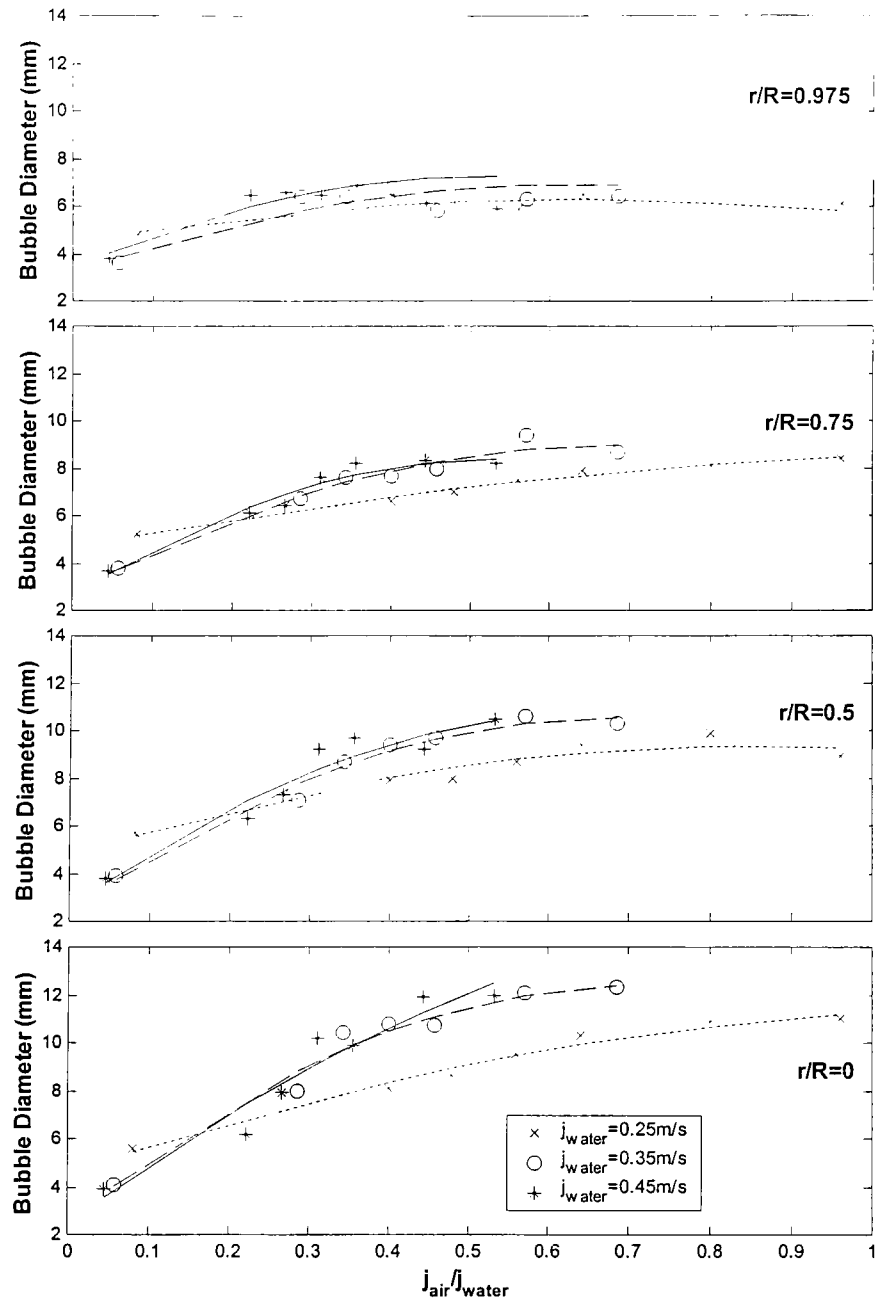
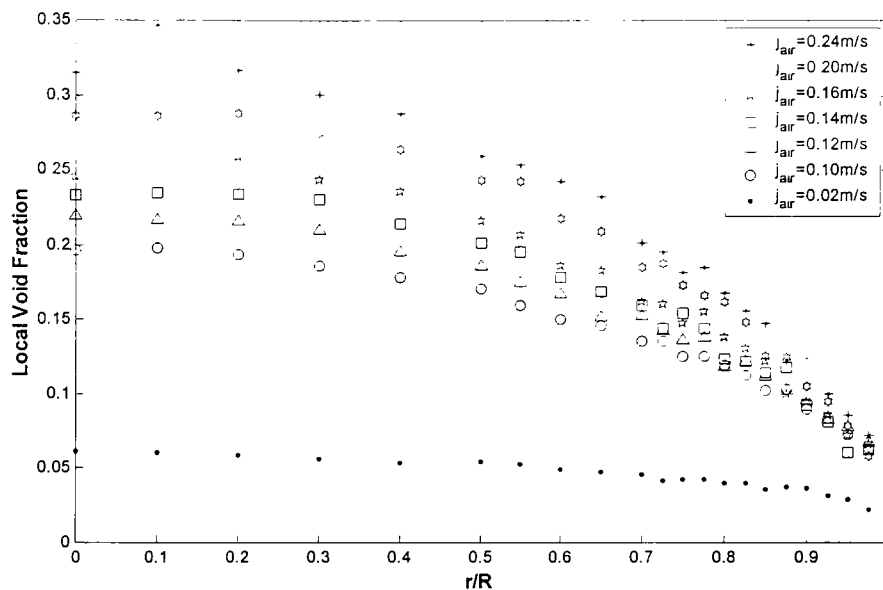**Figure 4.30   Bubble diameter vs. j_{air}/j_{water}**

Figure 4.31   Radial local void fraction distribution for j_{water}=0.25m/s
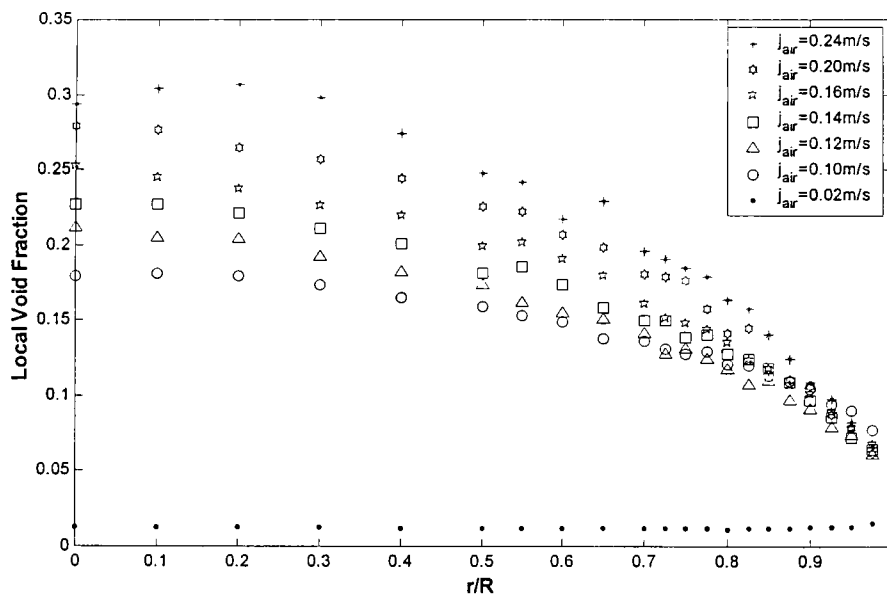

Figure 4.32   Radial local void fraction distribution for j_{water}=0.35m/s
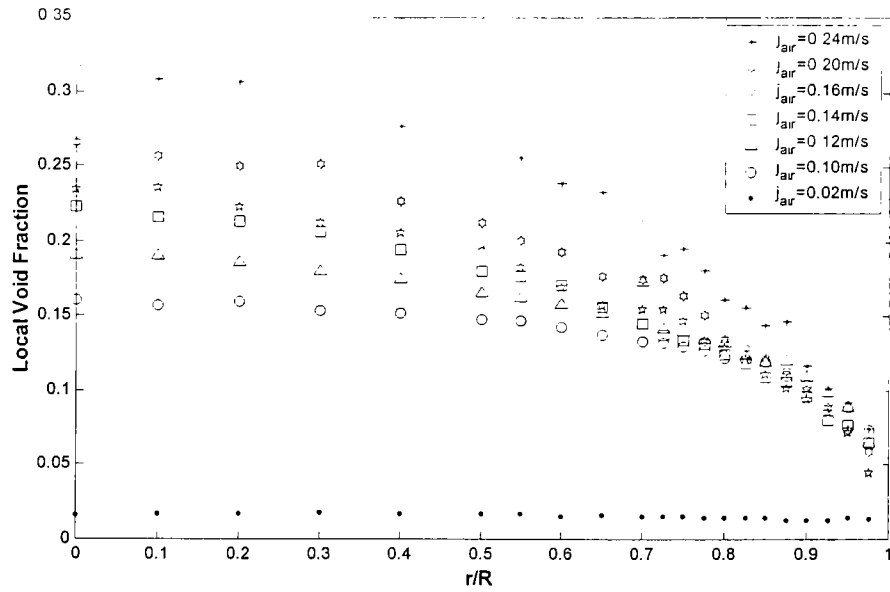
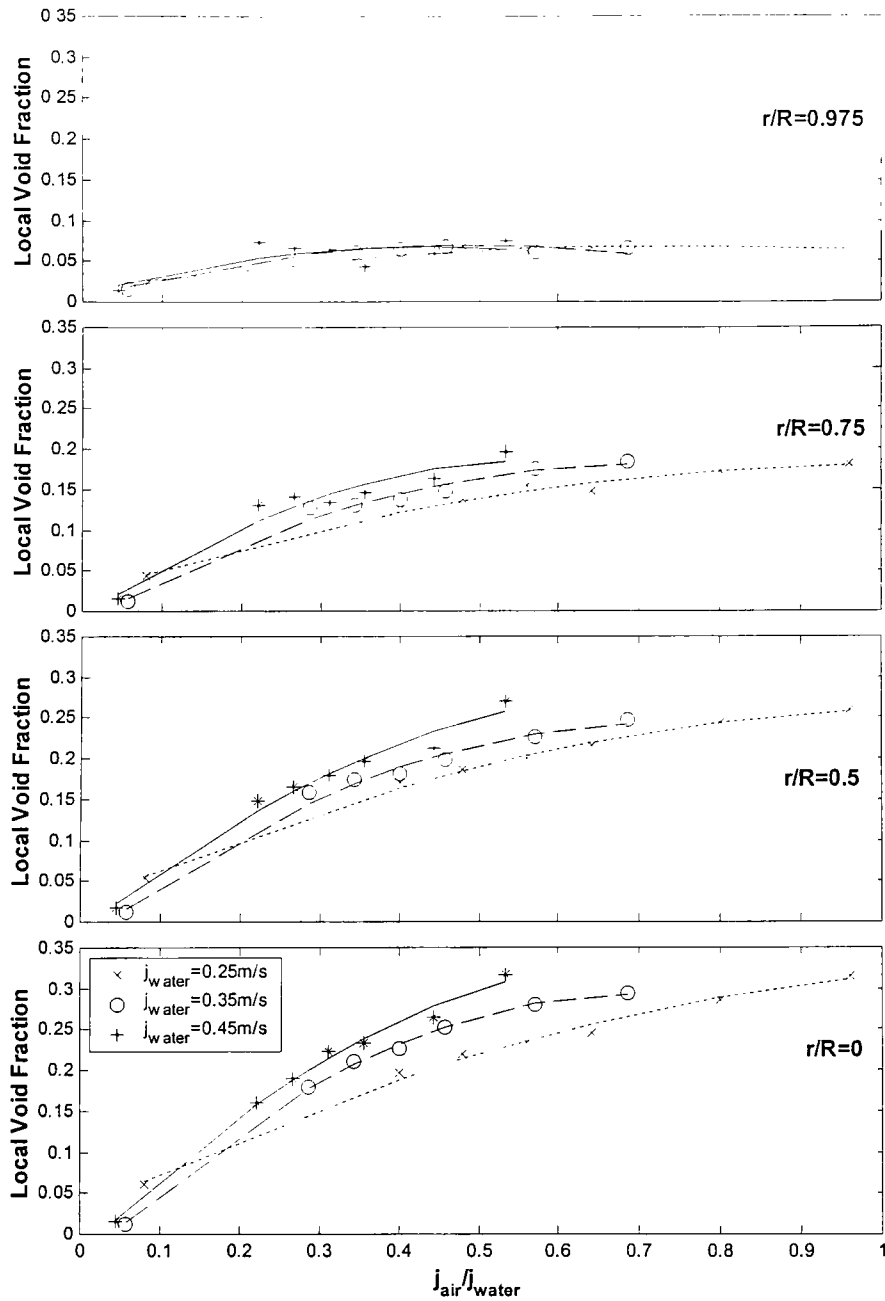**Figure 4.33   Radial local void fraction distribution for** j_{water}=0.45m/s

Figure 4.34   Local void fraction vs. j_{air}/j_{water}

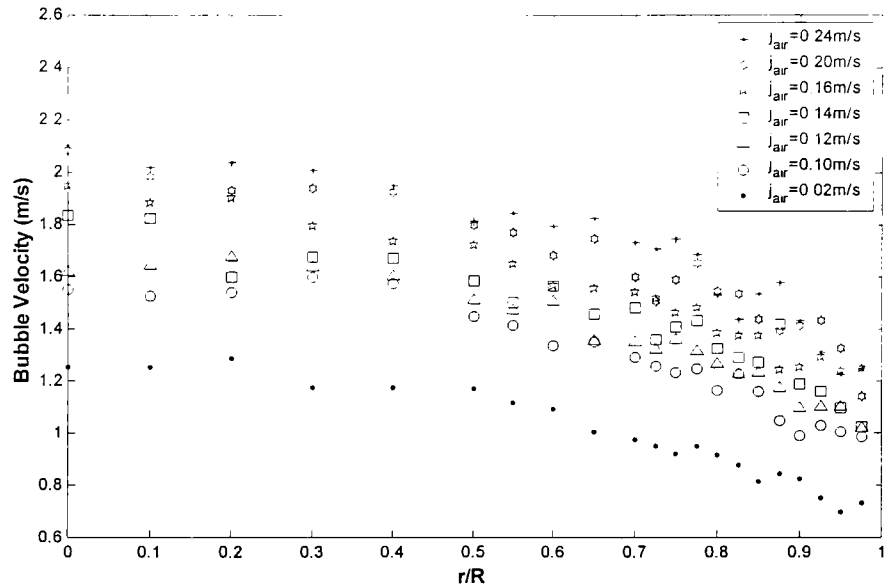**Figure 4.35   Radial bubble velocity distribution for j_{water}=0.25m/s**
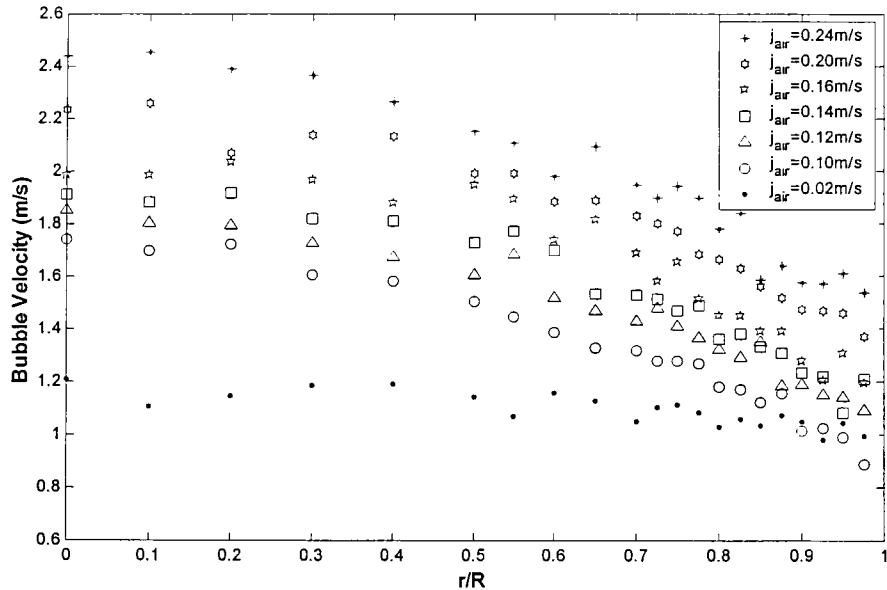

Figure 4.36   Radial bubble velocity distribution for j_{water}=0.35m/s

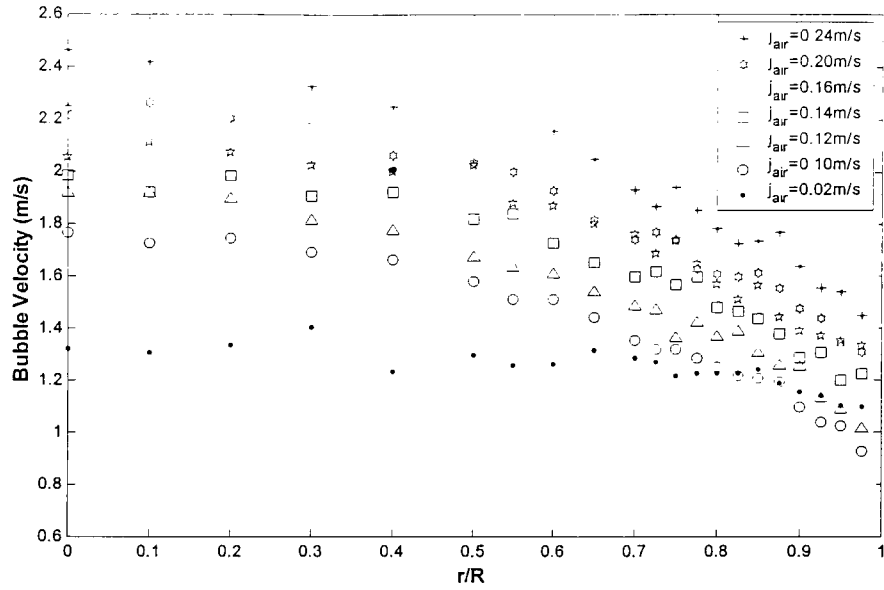**Figure 4.37   Radial bubble velocity distribution for j_{water}=0.45m/s**
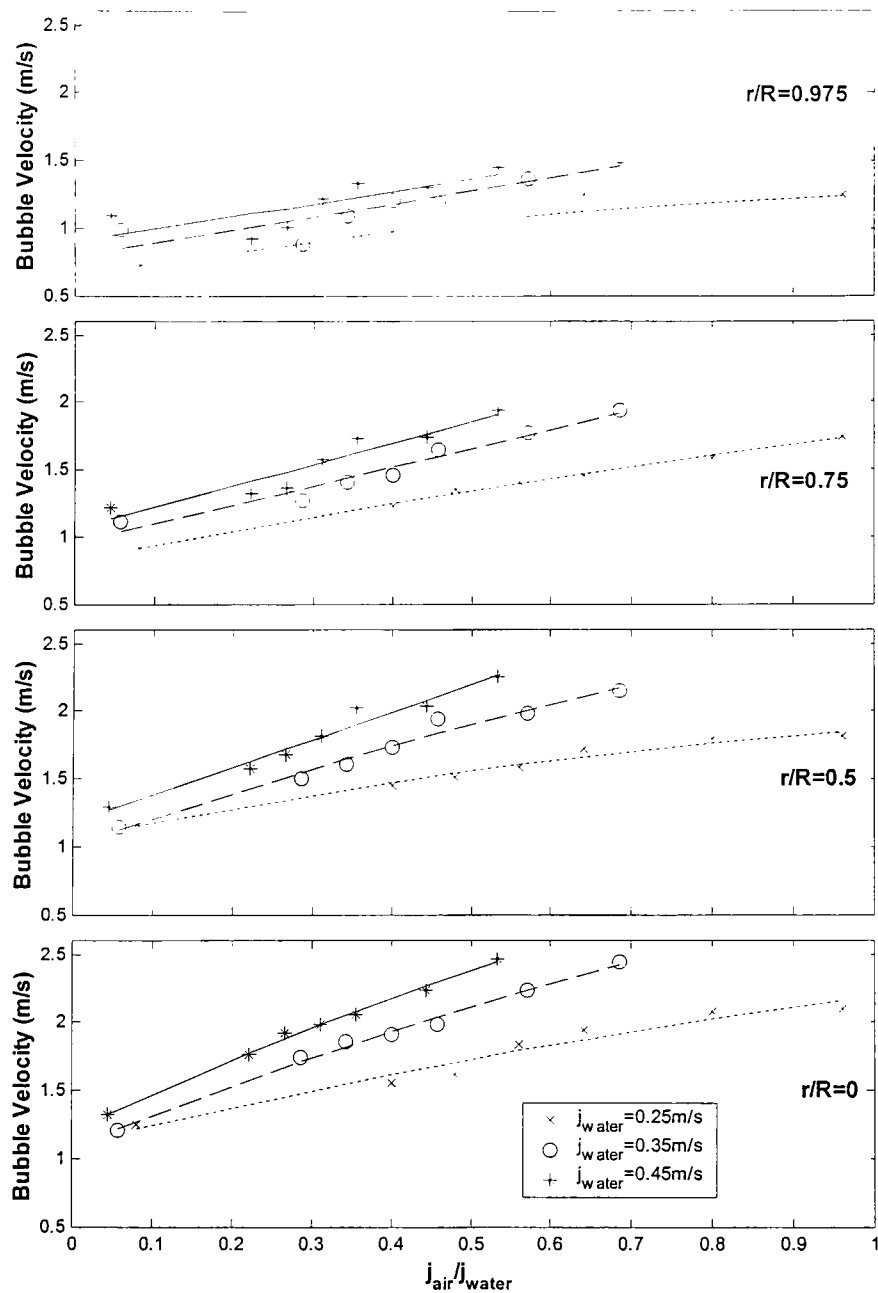
Figure 4.38   Bubble velocity vs. j_{air}/j_{water}
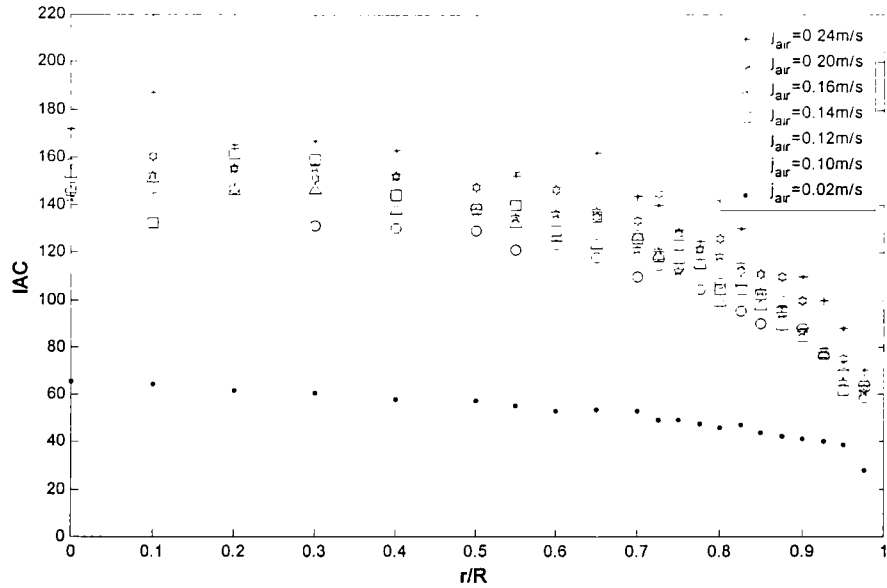
Figure 4.39   Radial *IAC* distribution for *j_water*=0.25m/s
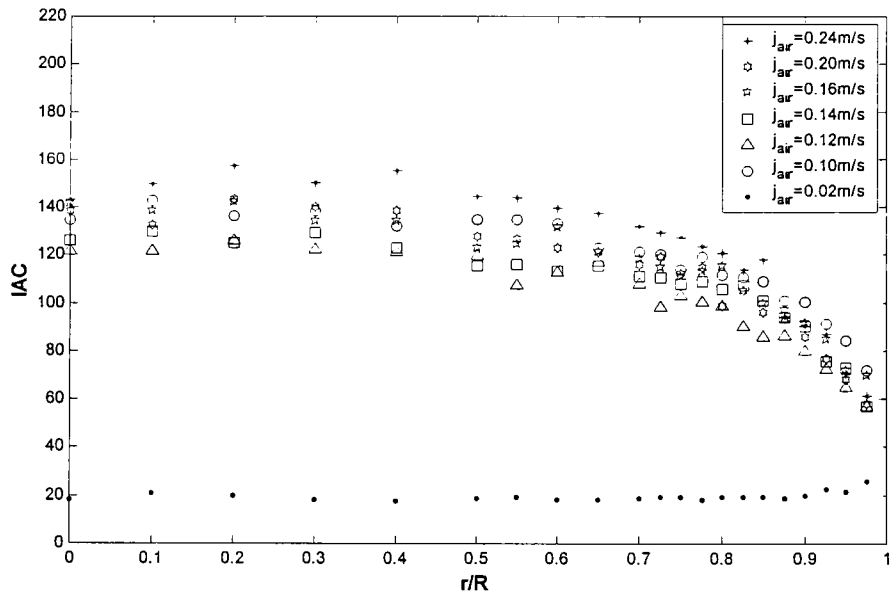
Figure 4.40   Radial *IAC* distribution for *j_water*=0.35m/s
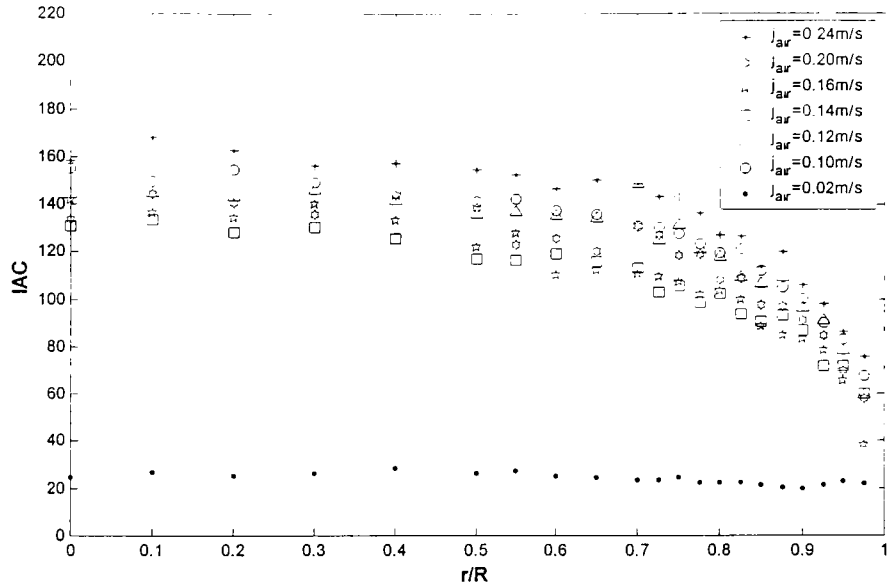
Figure 4.41   Radial *IAC* distribution for *j_{water}*=0.45m/s
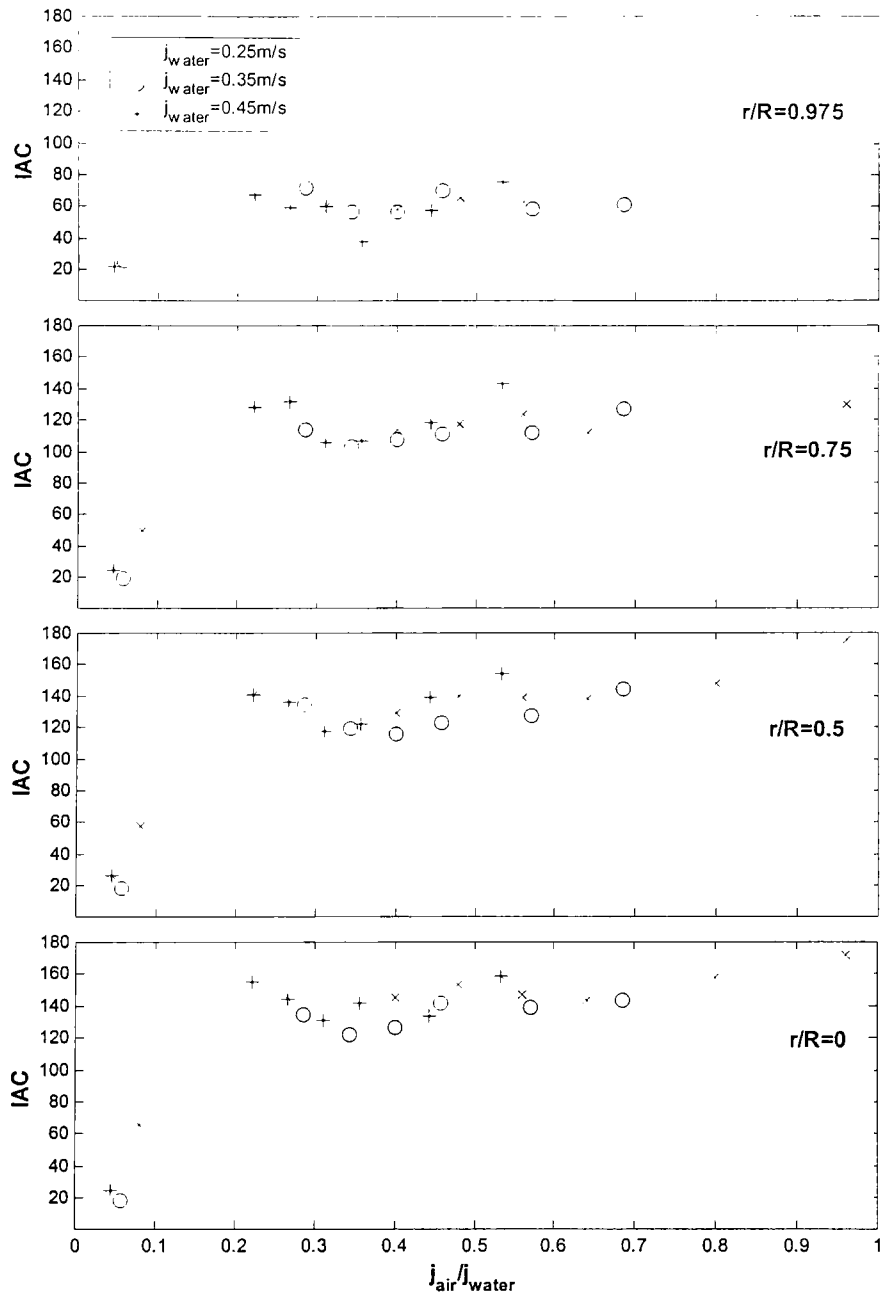
Figure 4.42   *IAC* vs. j_{air}/j_{water}
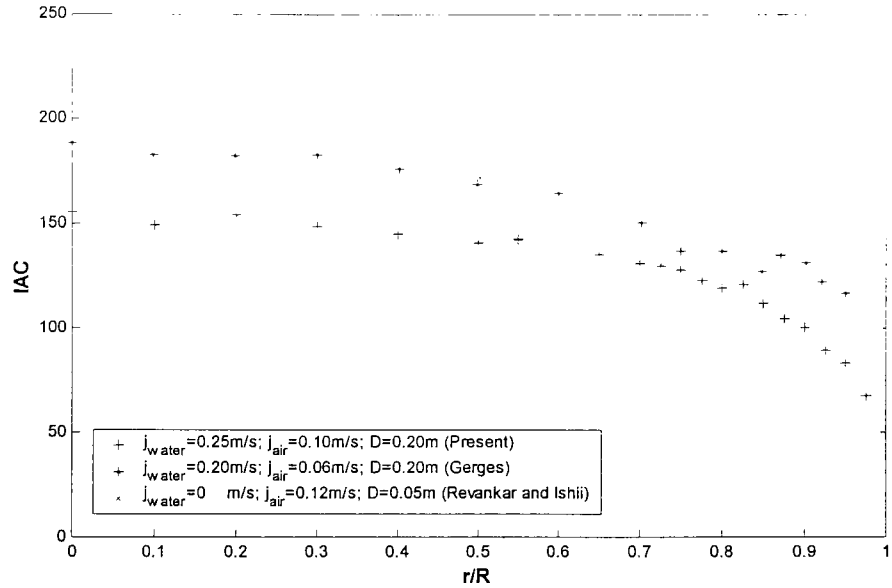
Figure 4.43   Comparison of *IAC* profiles in small and large diameter pipes at approximate flow conditions
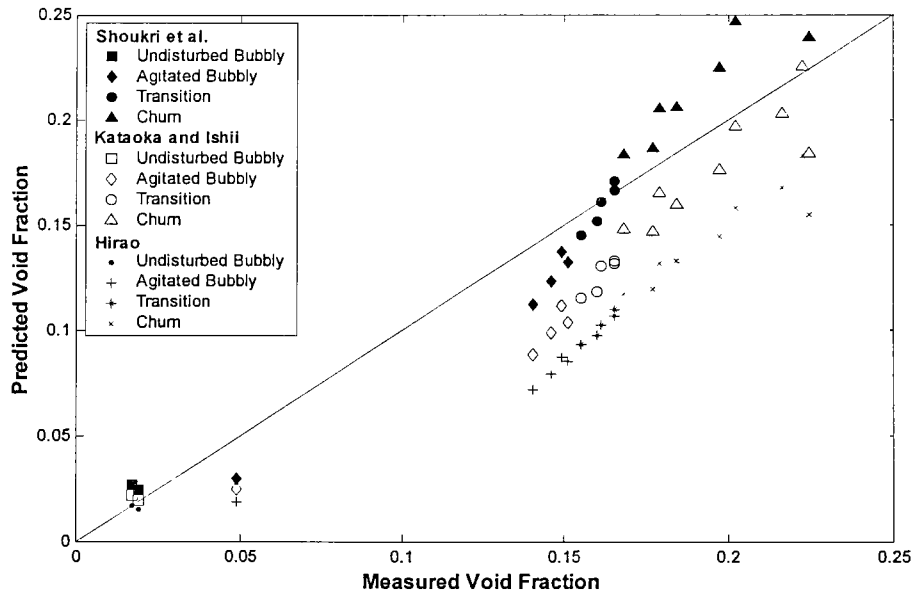
Figure 4.44   Void fraction predicted by drift-flux model correlations
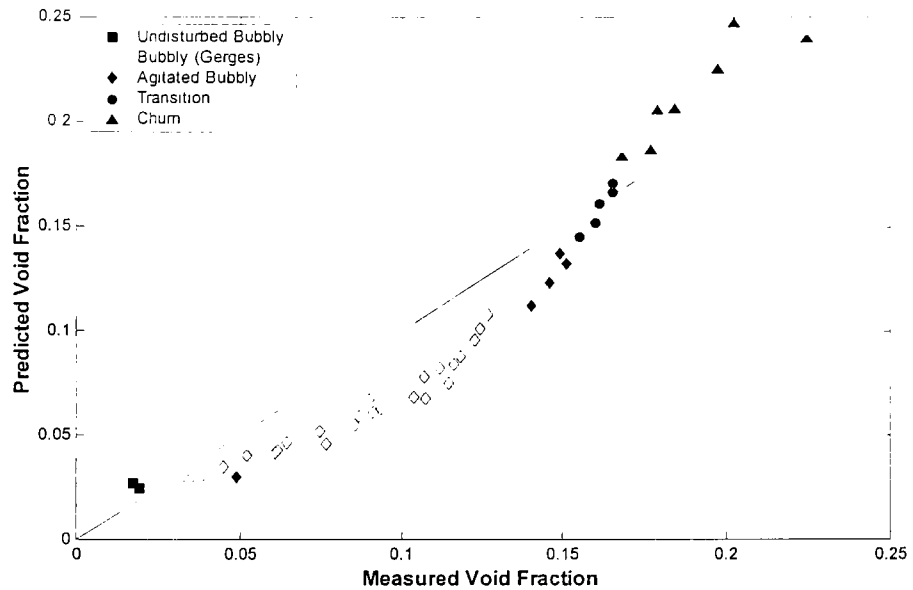
Figure 4.45   Void fraction measured from Gerges' and present experiments predicted by Shoukri et al.'s drift-flux model
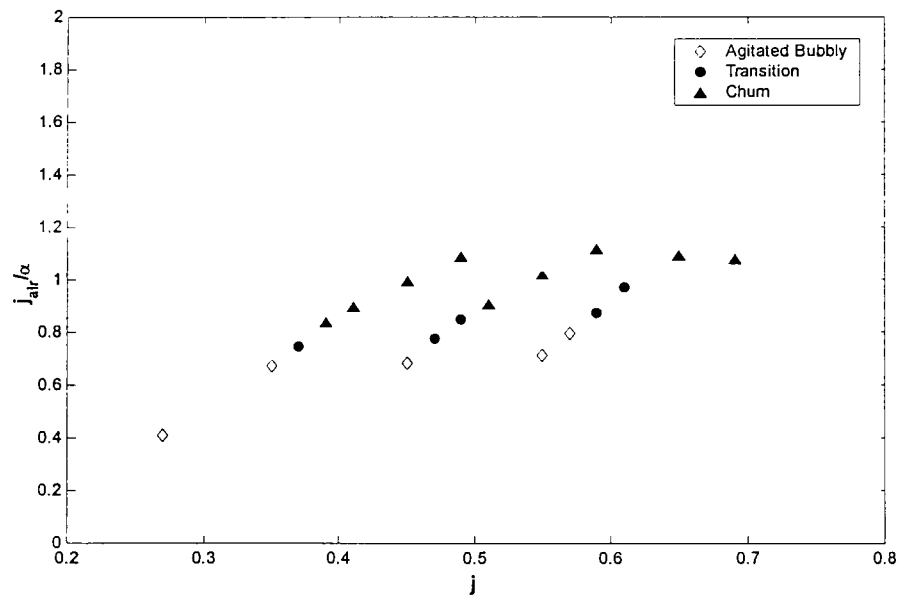
Figure 4.46 j_{air}/α vs. j for different flow regimes

Chapter 5

Conclusions

A better understanding of the two-phase flow structure in large diameter pipes is desired to improve two-phase fluid models for industrial applications. The flow structure and flow regime maps developed from studies in small diameter pipes do not accurately reflect the two-phase flow in larger diameter pipes. This research is aimed at increasing the database and obtaining a better understanding of two-phase flow in large diameter pipes.

Experiments were performed in a 20cm diameter two-phase flow loop. The local bubble characteristics such as local void fraction, bubble diameter, frequency and velocity were measured using a dual optical probe. The measurements were made across the pipe diameter for 21 different flow conditions, from bubbly to churn flow ($0.02\text{m/s} \leq j_{air} \leq 0.24\text{m/s}$, $0.25\text{m/s} \leq j_{water} \leq 0.45\text{m/s}$). The main conclusions can be summarized as:

1. The flow transitions from bubbly to churn without an intermediate slug flow regime as the air flow rate is increased at a fixed water flow rate. Taylor bubbles are not observed during the bubbly to churn flow transition. The bubbly to slug flow transition boundaries developed by Taitel et al. [9] and Mishima and Ishii

[24] for small diameter pipes occur at higher j_{air} than the transition of bubbly to churn in the present facility. The transition void fraction for bubbly to slug is about 0.25 while the transition void fraction for the present bubbly to churn is in the range $0.155 < <\alpha> < 0.165$.

2. The bubbly flow in a large diameter pipe can be classified as undisturbed bubbly and agitated bubbly flow due to the different characteristics of these two regimes. The undisturbed bubbly flow is defined when the bubbles flow upward with few interaction with adjacent bubbles, with average void fraction less than 0.04. In agitated bubbly flow, the bubbles have more random movement with significant bubble interactions. A downward motion of bubbles is also present due to the re-circulatory flow downstream of the larger bubbles.

3. The radial profiles of the bubble frequency, local void fraction of undisturbed bubbly flow are similar to those observed in small diameter pipes except the bubble diameter has a relatively flat profile. However, the profiles in agitated bubbly flow have a core-peak shape similar to churn flow in smaller diameter pipes.

4. The bubble frequency, diameter, local void fraction and velocity increase as j_{air}/j_{water} increases at any radial positions. There is no sudden change in any of the parameters as the flow transitions from bubbly to churn flow.

5. The *IAC* of undisturbed bubbly is significantly less than those of the other flow patterns. The *IAC* decreases slightly in agitated bubbly flow as the air flow rate increases, and then increase as the flow transition to churn flow.

6. The current data are in good agreement with the drift-flux model of Shoukri et al.[10] and Kataoka and Ishii [50] for the agitated bubbly and churn flow regimes.

The drift-flux model of Hirao et al. [52] underpredicts the data by up to 56 percent.

List of References

[1] S. Levy, 1999, *Two-phase flow in complex systems*, John Wiley & Sons, New York

[2] D. G. Shipley, 1984, Two-phase flow in large diameter pipes, *Chemical Engineering Sciences*, Vol. 39, No. 1, 163-165

[3] D. C. Lowe and K. S. Rezkallah, 1999, Flow regime identification in microgravity two-phase flows using void fraction signals, *Int. J. Multiphase Flow*, Vol. 25, 433-457

[4] T. L. Gould, 1974, Vertical two-phase steam-water flow in geothermal wells, *J. Petroleum Tech.*, Vol. 26, 833

[5] G. B. Wallis, 1969, *One-dimensional two-phase flow*, McGraw-Hill, New York

[6] N. Zuber and J. A. Findlay, 1965, Average volumetric concentration in two-phase flow systems, *J. Heat Transfer*, Nov., 453-468

[7] T. J. Liu and S. G. Bankoff, 1993a, Structure of air water bubbly flow in a vertical pipe-I liquid mean velocity and turbulence measurements, *Int. J. Heat Mass Transfer*, Vol. 36, No. 4, 1049-1060

[8] T. J. Liu and S. G. Bankoff, 1993b, Structure of air water bubbly flow in a vertical pipe-II void fraction, bubble velocity and bubble size distribution, *Int. J. Heat Mass Transfer,* Vol. 36, No. 4, 1061-1072

[9] Y. Taitel, D. Bornea and A. E. Dukler, 1980, Modeling flow pattern transitions for steady upward gas-liquid flow in vertical tubes, *AIChe Journal*, Vol. 26, No. 3, 345-354

[10] M. Shoukri, I. Hassan and I. Gerges, Two-phase bubbly flow structure in large-diameter vertical pipes, *accepted for publication in Canadian J. of Chemical Engineering*

[11] B. Stankovic, 1997, An experimental study on the local void fraction measurements in large-diameter vertical pipes using optical fiber probes, *M. Eng. Thesis, McMaster University*

[12] I. E. Gerges, 1999, Two-phase bubbly flow structure in large diameter pipes, *M. Eng. Thesis*, McMaster University

[13] T. Hibiki and M. Ishii, 2000, Experimental study on hot-leg U-bend two-phase natural circulation in a loop with a large diameter pipe, *Nuclear Engineering and Design*, Vol. 195, 69-84

[14] A. Ohnuki and H. Akimoto, 2000, Experimental study on transition of flow pattern and phase distribution in upward air-water two-phase flow along a large vertical pipe, *Int. J. Multiphase Flow*, Vol. 26, 367-386

[15] S. M. Nada, A. Abdul-Razzak, B. Stankovic and M. Shoukri, 1996, Flow regimes and drift-flux correlations for gas-liquid flow in large diameter vertical pipes, *International Congress of Fluid Dynamics and Propulsion*, Cairo, Egypt, Dec. 27-30

[16] H. Cheng, J. H. Hills and B. J. Azzorpardi, 1998, A study of the bubble-to-slug transition in vertical gas-liquid flow in columns of different diameter, *Int. J. Multiphase Flow*, Vol. 24, No.3, 431-452

[17] C. Yung, F. Chang and J. Skears, 1977, SOPHT-A computer model for CANDU-PHWR heat transport networks and their control, *Nuclear Technology,* Vol. 35, Oct.

[18] R. M. Mandl and P. A.Weiss, 1982, PKL tests on energy transfer mechanisms during small-break LOCAs, *Nuclear Safety*, Vol. 23, No. 2

[19] G. F. Hewitt and N. S. Hall-Taylor, 1970, *Annular Two-phase Flow*, Pergamon Press

[20] K. W. McQuillan and P. B. Whalley, 1985, Flow patterns in vertical two-phase flow, *Int. J. Multiphase Flow*, Vol. 11, No. 2, 161-175

[21] A. E. Dukler, J. A. Fabre, J. B. McQuillen and R. Vernon, 1988, Gas-liquid flow at microgravity conditions: flow patterns and their transition, *Int. J. Multiphase Flow*, Vol. 14, No. 4, 389-400

[22] G. F. Hewitt and D. N. Roberts, 1969, Studies of two-phase flow patterns by simultaneous X-ray and flash photography, *Rept. AERE-M2159, UKAEA*, Harwell

[23] P. Griffith and G. B. Wallis, 1961, Two-phase slug flow, *J. Heat Transfer*, Vol. 83, 307

[24] K. Mishima and M. Ishii, 1984, Flow regime transition criteria for upward two-phase flow in vertical tubes, *Int. J. Heat Mass Transfer*, Vol. 27, No. 5, 723-737

[25] R. S. Brodkey, 1967, *The phenomena of Fluid Motion*, Addison-Wesley Press

[26] O. C. Jones, N. Zuber, 1975, The interrelation between void fraction fluctuations and flow patterns in two phase flow, *Int .J. Multiphase flow*, Vol. 2, 273-306

[27] N. A. Radovicich and R. Moissis, 1962, The transition from two-phase bubble flow to slug flow, *MIT Report*, No. 7-7633-22

[28] A. Matuszkiewicz, J. C. Flamand and J.A. Boure, 1987, The bubble-slug flow pattern transition and instabilities of void fraction waves, *Int. J. Multiphase Flow*, Vol. 13, No. 2, 199-217

[29] G. F. Hewitt, 1990, Non-equilibrium two-phase flow, *Proc. Heat Transfer'90*, KN-25, Israel, 385-394

[30] R. K. Das and S. Pattanayak, 1994, Bubble to slug flow transition in vertical upward two-phase flow through narrow tubes, *Chemical Engineering Science*, Vol. 49, No. 13, 2163-2172

[31] P. Griffith and G. A. Snyder, 1964, The bubbly-slug transition on a high velocity two-phase flow, *MIT Report*, No. 5003-29

[32] N. Kurul and M. Z. Podowski, 1991, *ANS Proc. 1991, National Heat Transfer Conference*, Minneapolis

[33] M. Ishii, 1977, One-dimensional drift-flux model and constitutive equations for relative motion between phases in various two-phase flow regimes, *Argonne National Laboratory Report*, ANL-77-47

[34] A. Serizawa, I. Kataoka and I. Michiyoshi, 1975, Turbulence structure of air-water bubbly flow-II. local properties, *Int. J. Multiphase Flow*, Vol. 2, 235-246

[35] Z. Bilicki and J. Kestin, 1987, Transition criteria for two-phase flow patterns in vertical upward flow, *Int. J. Multiphase Flow*, Vol. 13, No. 3, 283-294

[36] R. Moissis and P. Griffith, 1962, Entrance effects in two-phase slug flow, *J. Heat Transfer*, Vol. 84, 29-39

[37] N. Brauner and D. Barnea, 1986, Slug/Churn Transition in upward gas-liquid flow, *Chemical Engineering Science*, Vol. 41, No. 1, 159-163

[38] G. F. Hewitt and S. Jayanti, 1993, To churn or not to churn, *Int. J. Multiphase Flow*, Vol. 19, 527-529

[39] X. T. Chen and J. T. Brill, 1997, Slug to churn transition in upward vertical two-phase flow, *Chemical Engineering Science*, Vol. 52, No. 23, 4269-4272

[40] Y. Taitel and A. E. Dukler, 1976, A model for predicting flow regime transitions in horizontal and near horizontal gas-liquid flow, *AIChe Journal*, Vol. 22, No. 1, 47-54

[41] O. L. Pushkin and Yu. L. Sorokin, 1969, Breakdown of liquid film motion in vertical tubes, *Heat Transfer Sov. Res.*, Vol. 1, No. 5, 56-64

[42] D. Barnea, 1987, Transition from annular flow and from dispersed bubble flow-unified models for the whole range of pipe inclination, *Int. J. Multiphase Flow*, Vol. 12, 733-744

[43] J. O. Hinze, 1959, *Turbulence*, McGraw-Hill

[44] M. M. Sorour and M. S. El-Beshbeeshy, 1998, Void fraction and pressure fluctuations of bubbly flow in a vertical annular channel, *Experiments in Fluids*, Vol. 4,163-170

[45] K. Sekoguvhi, M. Nakazatomi, M. Takeishi, H Shimizu, K. Mori and G. Miyake, 1992, Pressure effect on velocity of liquid lumps in vertical upward gas-liquid two-phase flow, *JSME International Journal*, Series 2, Vol. 35, No. 3, 380-387

[46] H. A. Hasanein, A. M. C. Chan, M. Kawajji and Y. Yoshioka, 1996, Steam–water two-phase flow in large diameter vertical piping at high pressures and temperatures, *ASME/JSME 4th International conference on Nuclear Engineering (ICONE-4)*, New Orleans, Louisiana, March 10-14, Vol. 1-Part B, 675-685

[47] H. A. Hasanein, M. Kawaji, A. M. C. Chan and Y. Yoshioka, 1997, Flow regime identification of steam-water flow in a large vertical pipe at elevated pressures, *ASME Fluids Engineering Division Summer Meeting FEDSM'97*, June 22-26

[48] G. Kocamustafaogullari and M. Ishii, 1985, Foundation of interfacial area transport equation and its closure relations, *Int. J. Heat Mass Transfer*, Vol. 38, 481-493

[49] G. Wang, 2001, An experimental study of vertical upward air-water two-phase slug flow using hot-film anemometry, *Ph. D. Thesis, Memorial University of Newfoundland*

[50] I. Kataoka and M. Ishii, 1987, Drift flux model for large diameter pipe and new correlation for pool void fraction, *Int. J. Heat Mass Transfer*, Vol. 30, No. 9, 1927-1939

[51] D. Barnea, 1987, Transition from annular flow and from dispersed bubble flow-unified models for the whole range of pipe inclination, *Int. J. Multiphase Flow*, Vol. 12, 733-744

[52] Y. Hirao, K. Kawanishi, A. Tsuge and T. Kohriyama, 1986, Experimental study on drift flux correlation formulas for two-phase flow in large diameter tubes, *Proceedings of the 2nd International Topical Meeting on Nuclear Power Plant Thermal Hydraulic and Operations*, Tokyo, Japan

[53] M. Ishii, 1975, Thermo-fluid dynamic theory of two-fluid flow, *Eyerolles*, Paris/Scientific and Medical Publications of France, New York

[54] M. Ishii and K. Mishima, 1984, Two-fluid model and hydrodynamic constitutive relations, *Nuclear Engineering and Design*, Vol. 82, 107-126

[55] M. Ishii and K. Mishima, 1980, Study of two-fluid model and interfacial area, *Nureg/Cr-1873-Anl-80-111*

[56] T. Okawa, K. Yoneda and Y. Yoshioka, 1998, New interfacial drag force model including effect of bubble wake (I) Model development for steam-water bubbly flow in large–diameter pipes, *Journal of Nuclear Science and Technology*, Vol. 35, No. 12, 895-904

[57] N. Hatta, M. Omodaka and H. Fujimoto, 1998, Theoretical modeling of gas-liquid flow in a vertical and straight pipe, *Steel Research,* Vol. 69, No. 3, 92-101

[58] N. Hatta, H. Fujimoto, M. Isobe and J-S. Kang, 1998, Theoretical analysis of flow characteristics of multiphase mixtures in a vertical pipe, *Int. J. Multiphase Flow*, Vol. 24, No. 4, 539-561

[59] I. Kataoka and A. Serizawa, 1990, Interfacial Area Concentration in bubbly Flow, *Nuclear Engineering and Design*, Vol. 120, 163-180

[60] G. Kocamustafaogullari, W.D. Huang and J. Razi, 1994, Measurement and modeling of average void fraction, bubble size and interfacial area, *Nuclear Engineering and Design,* Vol. 148, 437-453

[61] A. Serizawa and I. Kataoka, Phase distribution in two-phase flow, 1987, *Proc. ICHMT Int. Sem. Transient Two-Phase Flow*, Dubrovnik, Yugoslavia, May 24-30

[62] M. R. Ozgu, J. C. Chen and N. Eberhardt, 1973, A capacitance method for measurement of film thickness in two-phase flow. *Rev.Sci.Instrum*, Vol. 44, No. 12

[63] T. Uga, 1972, Determination of bubble-size distribution in a Boiling Water Reactor, *Nuclear Engineering and Design*, Vol. 22, 252-261

[64] A. Serizawa, I. Kataoka and I. Michiyoshi, 1975, Turbulence structure of air-water bubbly flow-I. measuring techniques, *Int. J. Multiphase Flow*, Vol. 2, 221-233

[65] J. M. Delhaye, 1981, *Instrumentation*, Hemisphere Publishing Corporation, 455-483

[66] R. A. Herringe and M. R. Davis, 1976, Structure development of gas-liquid mixture flows, *J. Fluid Mech.*, Vol. 73, 97-123

[67] E. Barrau, N. Riviere, Ch. Poupot and A. Cartellier, 1999, Single and double optical probes in air-water two-phase flows: real time signal processing and sensor performance, *Int. J. Multiphase Flow*, Vol. 25, 229-256

[68] F. A. Hamad, B. K. Pierscionek and H. H. Bruun, 2000, A dual optical probe for volume fraction, drop velocity and drop size measurements in liquid-liquid two-phase flow. *Measurement Science Technology*, Vol. 11, 1307-1318

[69] S. K. Wang, S. J. Lee, O. C. Jones and R. T. Latey, 1987, Turbulent structure and phase distribution measurements in bubbly two-phase flows, *Int. J. Multiphase Flow*, Vol. 3, 327-343

[70] Jr. H. Duns and N. C. J. Ros, 1963, Vertical flow of gas and liquid mixtures from boreholes, *Proc. 6th World Petroleum Congress Frankfurt*

[71] G. J. Kirouac, T. A. Trabold, P. F. Vassallo, W. E. Moore and R. Kumar, 1999, Instrumentation development in two-phase flow, *Experimental Thermal and Fluid Science*, Vol. 20, 79-93

[72] R. J. Moffat, 1998, Describing the uncertainties in experimental results, *Experimental Thermal and Fluid Science*, Vol. 1, 3-17

[73] G. Kocamustafaogullari and A. Wang, 1991, An experimental study on local interfacial parameters in a horizontal bubbly two-phase flow, *Int. J. Multiphase Flow*, Vol. 17, 553-572

[74] N. T. Thang and M. R. Davis, 1979, The structure of bubbly flow through Venturis, *Int. J. Multiphase Flow*, Vol. 5, 17-37

[75] A. Ohnuki, H. Akimoto and Y. Sudo, 1995, Flow pattern and its transition in gas-liquid two-phase flow along a large vertical pipe, *Proceedings of the 2nd International Conference on Multiphase Flow*, Kyoto, Japan, FT1-17

[76] T. K. Larson, An Investigation of Integral Facility Scaling and Data Relation Methods (Integral System Test Program), 187, *NuREG/CR-4531*, EGG-2440, 43

[77] C. H. Song, H. C. No and M. K. Chung, 1994, Investigation of bubble flow developments and its transition based on the instability of void fraction waves, *Int. J. Multiphase flow*, Vol. 20, 381-403

[78] T. Hibiki, S. Hogsett and M. Ishii, 1998, Local measurement of interfacial area, interfacial velocity and liquid turbulence in two-phase flow, *Nuclear Engineering and Design*, Vol. 184, 287-304

[79] P. Venkateswararao, R. Semiat and A. E. Dukler, 1982, Flow pattern transition for gas-liquid flow in a vertical rod bundle, *Int. J. Multiphase Flow,* Vol. 8, No. 5, 509-524

[80] R. C. Fernandes, R. Semiat and A. E. Dukler, 1983, Hydrodynamic model for gas-liquid slug flow in vertical tubes, *AIChe Journal*, Vol. 29, No. 6

[81] D. J. Nicklin, J. O. Wilkes, and J. E. Davidson, 1962, Two-phase flow in vertical tubes, *Trans. Inst. Chem. Eng*, Vol. 40, 61-68

[82] N. Zuber, 1967, Flow excursions and oscillations in boiling, two-phase flow systems with heat addition, *Proceedings of EURATOM Symposium on Two-phase Flow Dynamics*, Vol. 1, 1070-1089

[83] S. T. Revankar and M. Ishii, 1992, Local interfacial area measurement in bubbly flow, *Int. J. Heat Mass Transfer*, Vol. 35, No. 4, 913-925

[84] T. Hibiki, T.Takamasa and M. Ishii, 2001, Interfacial area transport of bubbly flow in a small diameter pipe, *Journal of Nuclear Science and Technology*, Vol. 38, No. 8, 641-620